Habilitation à diriger des recherches. Debregeas Georges

Georges Debregeas

▶ **To cite this version:**

Georges Debregeas. Habilitation à diriger des recherches. Debregeas Georges. Biophysique [physics.bio-ph]. Université Pierre et Marie Curie - Paris VI, 2010. tel-00672940

HAL Id: tel-00672940

https://theses.hal.science/tel-00672940

Submitted on 22 Feb 2012

HAL is a multi-disciplinary open access archive for the deposit and dissemination of scientific research documents, whether they are published or not. The documents may come from teaching and research institutions in France or abroad, or from public or private research centers.

L'archive ouverte pluridisciplinaire **HAL**, est destinée au dépôt et à la diffusion de documents scientifiques de niveau recherche, publiés ou non, émanant des établissements d'enseignement et de recherche français ou étrangers, des laboratoires publics ou privés.

Université Pierre et Marie Curie
Paris

HABILITATION A DIRIGER DES RECHERCHES

GEORGES DEBREGEAS

JURY :

Mme Martine Ben Amar
Mme Isabelle Cantat (rapporteur)
Mme Christiane Caroli
M. Antoine Chateauminois (rapporteur)
M. Jean-Pierre Munch
M. Olivier Pouliquen (rapporteur)

Laboratoire de Physique Statistique - CNRS/ENS/UPMC UMR 8550
24, rue Lhomond 75231 Paris cedex 05

Résumé :

Ce travail vise à décrire la réponse mécanique de matériaux divisés tels que les mousses aqueuses et les matériaux granulaires. Ces systèmes ont un comportement de type élastique à faible déformation et plastique au-delà d'une déformation seuil. Le caractère localisé des événements de plasticité et la longue portée des interactions élastiques conduisent à des phénomènes comparables de localisation d'écoulement, d'intermittence et de vieillissement induit par le cisaillement. Nous avons cherché à les étudier au moyen d'approches expérimentales et numériques variées associant des mesures aux échelles locales et globales. Nous avons par ailleurs développé des mesures, résolues spatialement, des déformations et contraintes mécaniques aux interfaces de frottement. Nous avons notamment développé un capteur tribologique, utilisant des micro-capteurs de force de type MEMS, qui permet une mesure dynamique des contraintes à la base d'un film élastique en frottement. Ce senseur, qui constitue un analogue rudimentaire du système mécanorécepteur/peau, a été mis à profit dans le cadre d'une étude de la transduction de l'information tactile dans le toucher humain par une approche de type bio-mimétique.

Abstract :

This work aims at describing the mechanical response of divided materials such as aqueous foams and granular materials. These systems exhibit a solid-like behavior under moderate shear, and flow plastically beyond a threshold strain. The local nature of plastic events and the long range elastic interactions are responsible for the existence of characteristic mechanisms such as strain localization, intermittency or strain-induced aging. We have probed them using various experimental and numerical approaches that combine local and global measurements. We have also developed spatially resolved measurements of interfacial deformations at frictional joints. Among them, we have developed a tribological sensor, based on the use of MEMS micro-force sensors, which allows one to monitor the friction-induced stress at the bottom of a thin elastic film. This sensor, which provides a rudimentary analogue of the mechanoreceptor/skin system, was used to study the transduction of tactile information in human touch, through a bio-mimetic approach.

Sommaire

CURRICULUM VITAE

Georges Debrégeas

Chargé de Recherche de 1ère classe

Laboratoire de Physique Statistique

CNRS/ENS/UPMC UMR 8550

24, rue Lhomond 75231 Paris cedex 05

+ 33 1 44 32 35 90 / + 33 1 44 32 34 33 / georges.debregeas@lps.ens.fr

http://www.lps.ens.fr/recherche/systemes-biologiques-integres

Né le 11 janvier 1971 - nationalité française

Formation universitaire

Doctorat de Physique, Université Paris 6 - 1997

DEA de Physique des Solides, Paris 6 - 1994

Diplômé de l'Ecole Polytechnique - 1993

Expérience professionnelle

CR au CNRS depuis Janvier 1999

Laboratoire de Physique Statistique - ENS, Paris, 2005-2009

Laboratoire des Fluides Organisés, Collège de France, Paris, 2002-2005

Institut Charles Sadron, Strasbourg, 1999-2002

Grainger Postdoctoral Fellow, James Frank Institute, University of Chicago, 1997-1999

Thèse de physique au laboratoire PCC, Institut Curie, Paris, 1994-1997

Principaux thèmes scientifiques

- Physique de la perception tactile.
- Mécanique du frottement et du contact solides.
- Rhéologie des matériaux divisés (milieux granulaires, mousses, colloïdes, etc.)
- Dynamique des réseaux de forces dans les empilements granulaires
- Hydrodynamique des films minces.
- Mouillage et capillarité.

ACTIVITE DE RECHERCHE

INTRODUCTION

J'ai effectuée ma thèse au laboratoire de Physico-Chimie de l'Institut Curie, sous la direction de Françoise Brochard Wyart (94-97). A la suite de cette thèse, qui portait sur l'hydrodynamique des films minces, j'ai effectué un stage post-doctoral au **James Frank Institute**, à **l'Université de Chicago**, dans l'équipe de Heinrich Jaeger et Sidney Nagel (97-98). J'y ai étudié l'écoulement de milieux granulaires par imagerie par résonance magnétique (IRM), tomographie X et *particle image velocimetry* (PIV). Ce travail expérimental a permis d'établir l'existence d'un phénomène de localisation des écoulements (bande de cisaillement) et de mesurer les profils d'écoulement en géométrie de Couette 3D.

Recruté au CNRS, j'ai rejoint en Janvier 1999 l'équipe de Jean-Marc di Meglio à l'**Institut Charles Sadron** à Strasbourg. J'ai développé des expériences d'imagerie sur des mousses aqueuses confinées entre deux plaques parallèles sous cisaillement. L'analyse de la forme des bulles et de leur mouvement a permis de comprendre certains aspects de la rhéologie complexe de ces matériaux et en particulier le phénomène de localisation. Ce travail expérimental s'est doublé d'une simulation numérique permettant de reproduire la plupart des observations expérimentales. Un modèle mécano-statistique d'écoulement a été proposé permettant de relier la cinématique de l'écoulement à la dynamique de fluctuations des contraintes au sein du matériau. J'ai par ailleurs développé plusieurs expériences pour étudier la dynamique d'évolution des contraintes au sein de systèmes granulaires ou colloïdaux soumis à de faibles sollicitations mécaniques. Ces expériences utilisaient la diffusion multiple de la lumière (DWS) mais aussi la tomographie X (expériences menées lors d'un séjour de deux mois à l'Université de Canberra, Australie). Une large part de ces travaux a constitué la thèse d'Alexandre Kabla soutenue en 2003.

Fin 2002, j'ai rejoint le **Laboratoire des Fluides Organisés** (LFO), dirigé par Pierre-Gilles de Gennes, au Collège de France. J'ai mis au point, dans le cadre de la thèse de Sébastien Besson, une expérience originale de mesure des propriétés adhésives de deux bulles de savon en contact. Ces mesures à l'échelle de la bulle ont permis de comprendre le comportement rhéologique de mousses aqueuses macroscopiques sous cisaillement rapide. J'ai initié par ailleurs un programme de recherche sur la mécanique du contact et le frottement solide dont l'objectif était d'obtenir des mesures mécaniques résolues spatialement à l'interface de frottement. Alexis Prevost, qui avait été recruté en 2003 au LFO dans l'équipe de Liliane Léger, m'a rejoint sur ce projet.

Lors de la fermeture du LFO, nous avons poursuivi ce travail au sein de l'équipe qui s'est formée en 2005 au **Laboratoire de Physique Statistique de l'ENS** à Paris, autour de Didier Chatenay, Jérôme Robert, Alexis Prevost et moi-même. Nous avons développé une méthode d'imagerie des interfaces rugueuses permettant d'extraire optiquement les champs de déformation de l'interface. Cette technique permet, à partir de ces champs, de mesurer de manière non invasive les contraintes interfaciales en régime de frottement (thèse de Julien Scheibert).

L'une des motivations de cette étude était de comprendre les aspects physiques de la transduction de l'information tactile dans le toucher humain. La perception tactile par le doigt repose en effet sur une exploration dynamique des surfaces au cours de laquelle l'information de texture est transmise, via la peau, à des cellules mécanoréceptrices situées sous l'épiderme. Afin de comprendre ce processus, nous avons développé un capteur bio-mimétique du doigt humain fondé sur l'utilisation de micro-capteurs de force de type MEMS (*Micro-Electro Mechanical Systems*, développés dans le cadre d'une collaboration avec le CEA-LETI à Grenoble) permettant de simuler le fonctionnement de ces cellules mécanoréceptrices. Ces capteurs sont recouverts d'une « peau » constituée d'une membrane élastomère, puis frottés contre des substrats solides texturés. Ce travail a permis de comprendre les

propriétés de filtrage de l'organe tactile, et en particulier de montrer le rôle essentiel de la texturation de la peau (les empreintes digitales) pour la transduction de l'information tactile.

Je suis impliqué depuis deux ans dans un projet de création d'un nouveau laboratoire (FRE Jean Perrin, UPMC) sur le campus de Jussieu, supposé regrouper plusieurs équipes de physiciens de la région parisienne travaillant sur des thématiques à l'interface de la physique et de la biologie. L'avenir de ce projet est aujourd'hui suspendu à l'affectation de locaux et de moyens par l'UPMC.

Dans la suite du document, les principaux thèmes abordés au cours de ces 12 années (depuis la fin de ma thèse) sont décrits en quelques pages suivies d'une ou plusieurs publications significatives. Chaque thème débute par un encadré résumant les principaux résultats obtenus. Les références indiquées dans le texte (en exposant) renvoient à la liste des publications donnée en fin de chaque thème (les références bibliographiques pouvant être trouvées dans les articles insérés).

L'ensemble de mes publications est listée chronologiquement au chapitre suivant (« publications, conférences et séminaire »), chacune d'entre elle étant par ailleurs téléchargeable à l'adresse :

http://www.lps.ens.fr/recherche/systemes-biologiques-integres/index.php?page=georges

THEME 1 : PLASTICITE ET ECOULEMENT DANS LES MILIEUX DIVISES (EMPILEMENTS GRANULAIRES ET MOUSSES AQUEUSES)

Résumé : Nous avons caractérisé de manière détaillée la dynamique d'écoulement dans un empilement 3D granulaire sous cisaillement, en géométrie de Couette cylindrique. Cet écoulement est caractérisé par l'existence d'une bande de cisaillement à la paroi du cylindre tournant. Un processus de localisation d'écoulement similaire a été démontré dans le cas d'une mousse aqueuse 2D (confinée entre deux plaques) sous cisaillement. Ce résultat a été confirmé par simulation numérique en géométrie plan parallèle.

Ce second système (mousses aqueuses 2D) nous a permis en outre de mesurer simultanément la dynamique du champ des contraintes et de plasticité au sein du matériau par une analyse de l'évolution de la structure des films liquide séparant les bulles. Nous avons ainsi pu montrer que l'instabilité de localisation résulte d'un couplage entre le champ des contraintes internes et la réponse mécanique du matériau : les évènements plastiques produisent localement un élargissement de la distribution des contraintes piégées associé à un abaissement du seuil de plasticité effectif.

Les systèmes divisés – tels que les milieux granulaires, les mousses, les émulsions concentrées – forment une classe de matériaux importante du point de vue industriel. Ils sont présents dans des domaines aussi variés que l'agro-alimentaire, l'industrie pharmaceutique, les cosmétiques ou encore les peintures. Les milieux granulaires sont également impliqués dans l'essentiel des phénomènes géologiques de surface. Pour de tels systèmes, l'énergie thermique est plusieurs ordres de grandeur inférieure à l'énergie nécessaire pour induire des réarrangements de la structure. En l'absence de contrainte externe, ils se trouvent piégés dans une configuration métastable et présentent, sous faible contrainte, un comportement de type solide élastique. Au-delà d'une contrainte seuil, des réarrangements plastiques peuvent être induits conduisant à un écoulement effectif du matériau qui présente cependant des caractéristiques très différentes de celles observées dans les liquides moléculaires. La courbe force/déformation présente ainsi un maximum (ou overshoot) qui révèle l'existence d'hétérogénéités spatiale de l'écoulement. En régime d'écoulement permanent, le signal de force montre de larges fluctuations qui sont la signature du caractère intermittent des événements de plasticité. La description de ces écoulements se heurte à la nécessité de modéliser tout à la fois les processus locaux de plasticité, dont l'échelle caractéristique est celle de la micro-structure, et les interactions élastiques de longue portée qui contrôlent la transmission des contraintes dans le matériau. D'un point de vue expérimental, il est donc impératif d'obtenir une mesure résolue à l'échelle de la micro-structure pour des écoulements macroscopiques.

A) MILIEUX GRANULAIRES SOUS CISAILLEMENT.

C'est dans cette optique que j'ai abordé, dans le cadre de mon stage post-doctoral, l'étude d'un écoulement granulaire tri-dimensionnel en géométrie de Couette cylindrique. J'ai fait appel à 3 techniques complémentaires – l'IRM, la tomographie X, et la PIV (*particle image velocimetry*) - afin d'étudier le mouvement des grains sous cisaillement lent[1] (Figure 1). Ce travail a permis de caractériser quantitativement les profils d'écoulements moyens sous différentes pression de confinement, ainsi que les profils de densité granulaire. Il a permis de montrer que la largeur de la bande de cisaillement - la région subissant l'essentiel des événements plastiques - était contrôlée par la taille des grains, et relativement indépendante des autres paramètres. La localisation de l'écoulement est par ailleurs associée à une réduction de la fraction volumique granulaire dans la bande de cisaillement.

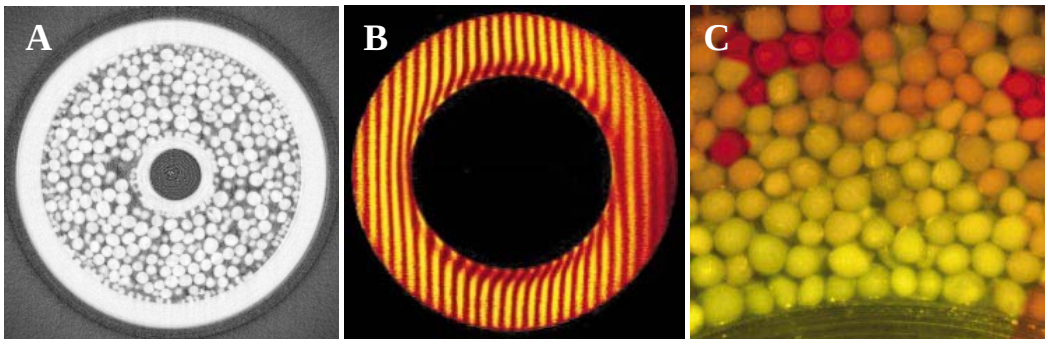

Figure 1: Expérience d'écoulement granulaire en cellule de Couette cylindrique. (A) image par tomographie X d'une tranche au sein de la cellule, permettant d'évaluer les profils radiaux de densité de grains. (B) Image par IRM du profil d'écoulement. La technique utilisée, dite de marquage de spin, permet d'identifier le mouvement moyen des grains se produisant dans une tranche de la cellule de Couette au cours d'un court intervalle de temps, au travers des déformations de lignes initialement parallèle. (C) image fixe extraite d'un enregistrement vidéo pris sous l'échantillon et servant à l'expérience de PIV.

Avec Christophe Josserand, j'ai proposé un modèle d'interprétation des profils d'écoulement observés fondé sur l'hypothèse d'une dynamique auto-similaire[2]. Ce modèle reposait sur l'observation que la longueur de corrélation des vitesses des grains semblait croître avec la distance à la paroi mobile. Ce modèle décrivait dès lors l'écoulement moyen comme résultant du mouvement intermittent de clusters de grains liés à la paroi mobile.

B) MOUSSES BIDIMENSIONNELLES CONFINEES ET MOUSSES NUMERIQUES.

De retour en France, j'ai souhaité étendre ce travail au cas des mousses aqueuses sous cisaillement. Pour permettre une observation directe de la dynamique à l'échelle des bulles, celle-ci est confinée entre deux vitres parallèles dont l'espacement permet d'accommoder une seule couche de bulles (Figure 2A). Cette mousse bidimensionnelle est cisaillée entre deux anneaux concentriques (géométrie de Couette cylindrique). Pour réduire l'effet de friction des bulles sur les parois de confinement, nous nous sommes limités à de très faibles taux de déformation. Cette expérience nous a permis de mettre en évidence un phénomène de localisation d'écoulement très similaire à celui observé dans les systèmes granulaires : après une déformation homogène transitoire, l'essentiel de la plasticité se concentre dans une bande de cisaillement large de quelques diamètres de bulle à proximité du disque interne. Nous avons pu établir la forme précise des profils d'écoulement pour des mousses humides et sèches. Nous avons également mis en évidence l'existence de corrélations spatiales du champ des vitesses instantanées, la longueur de corrélation étant proportionnelle à la distance au disque interne[3].

La grande similarité entre les comportements observés dans les milieux granulaires et les mousses sous cisaillement lent a constitué un résultat important car il laissait envisager un cadre de description commun pour ces deux systèmes. Mais le système modèle de mousse bidimensionnelle confinée offrait en outre la possibilité d'obtenir des informations au delà de ces seules mesures cinématiques : dans la limite d'écoulements quasistatiques, l'analyse de la forme des bulles permet en effet d'extraire directement le champ des contraintes au sein de la mousse à chaque instant. Par ailleurs, dans le cas de mousses sèches, les événements plastiques sont facilement identifiables puisqu'ils sont associés à une transformation topologique de la structure (processus T1, voir Figure 3A). Ce système est enfin propice à une modélisation numérique exacte. En effet, la configuration de la mousse à chaque instant correspond à la configuration minimale d'énergie de surface. Nous avons ainsi mis au point une expérience numérique de cisaillement de mousses 2D à partir d'un programme de minimisation de surface (Surface Evolver) que nous avons adapté à une situation d'écoulement sous cisaillement plan parallèle (Figure 2B). La mousse numérique possède des conditions limites périodiques dans l'une des directions, et est rigidement fixée sur ses deux autres frontières. Le cisaillement est obtenu en faisant

glisser ces deux murs rigides l'un par rapport à l'autre, par incrément infinitésimal. Nous avons observé là-encore l'apparition d'une bande de cisaillement le long d'une des parois après un régime transitoire de déformation uniforme de l'ordre de 1. Les caractéristiques mécaniques et d'écoulement (profil d'écoulement plastique, fluctuation des vitesses, état statistique des contraintes internes) ont montré un accord quantitatif avec les observations expérimentales réalisées en cellule de Couette[4].

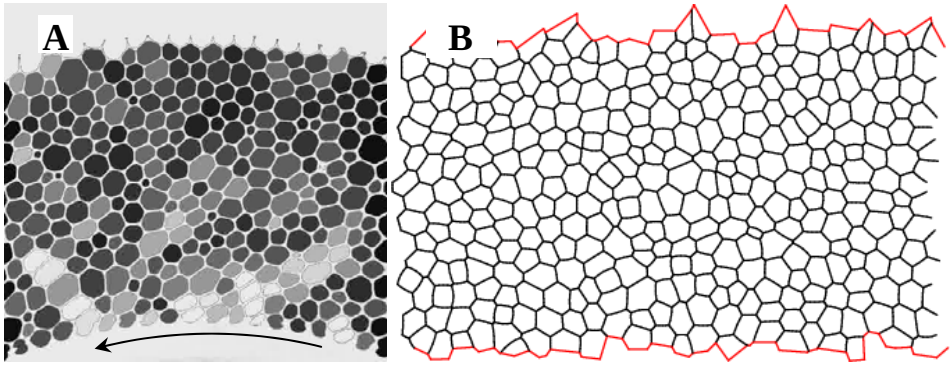

Figure 2 : (A) Détail d'une mousse bidimensionnelle confinée sous cisaillement de Couette. Le disque intérieur (en bas) tourne à vitesse constante, tandis que l'anneau extérieur (en haut) est fixe. Le code couleur traduit l'état de contrainte de cisaillement de chacune des bulles de l'échantillon, extraite de la structure du réseau de film, à l'instant de la prise d'image. (B) mousse numérique obtenue par minimisation de la surface totale des films, sous contrainte de volume constant dans chaque bulle. Le cisaillement de cette mousse est obtenu en déplaçant l'un des murs rigide (en rouge) de manière incrémentale. A chaque pas de temps, la structure d'équilibre de la mousse est recalculée.

Ce résultat numérique a permis de montrer que l'instabilité d'écoulement conduisant à la localisation pouvait apparaître même dans une géométrie qui garantissait l'homogénéité de la contrainte appliquée (ce qui n'est pas le cas de la géométrie de Couette cylindrique pour laquelle celle-ci décroit radialement avec la distance à la paroi du cylindre). Cette instabilité ne pouvait dès lors être expliquée que par l'existence d'un couplage entre l'écoulement plastique et une caractéristique structurelle du matériau qu'il nous fallait identifier. Dans cette optique, nous nous sommes intéressés aux distributions statistiques des contraintes piégées mesurées à l'échelle des bulles individuelles, dans différentes régions de l'échantillon. Nous avons pu montrer, dans l'expérience et la simulation numérique, que l'apparition de la bande de cisaillement s'accompagnait d'un élargissement de cette distribution dans la zone où se concentraient les événements plastiques. Cette observation était cohérente avec l'idée que l'hétérogénéité des contraintes piégées contrôle localement le seuil plastique effectif du matériau. Plus cette hétérogénéité est importante, plus le matériau est fragile c'est-à-dire susceptible de céder plastiquement en réponse à un accroissement de la contrainte globale appliquée.

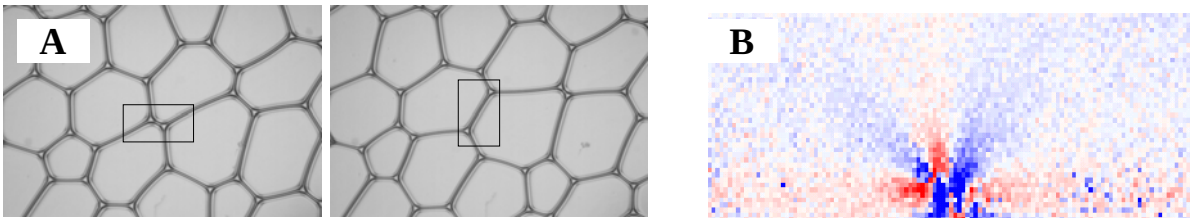

Figure 3 : (A) Image d'un événement plastique au sein d'une mousse bidimensionnelle. Cet événement se traduit par un changement topologique de la structure. (B) Variation du champ des contraintes de cisaillement associée à un tel processus TI et obtenue grâce à la simulation numérique. Les couleurs bleu et rouge indiquent respectivement un abaissement et un accroissement de la contrainte de cisaillement locale.

Il restait dès lors à comprendre comment les processus plastiques successifs contrôlaient à l'inverse l'évolution des distributions de contraintes piégées dans le matériau. Pour cela, nous avons tout d'abord déterminé, grâce à la simulation numérique, la déformation de la mousse associée à un réarrangement unique (Figure 3). Nous avons montré que la symétrie quadrupolaire de cette

perturbation mécanique élémentaire était à l'origine d'une corrélation spatiale à temps court des évènements plastiques suivant la direction d'écoulement. Ces événements très corrélés peuvent s'identifier à une fracture qui laisse une trace structurelle sous la forme d'un plus fort désordre de contrainte associé à un élargissement des distributions. Nous avons ensuite modélisé la dynamique d'évolution à temps long du champ des contraintes en régime d'écoulement permanent en évaluant l'effet cumulés de ces multiples événements plastiques distribués à travers l'échantillon. Ce modèle mécano-statistique a permis de reproduire correctement la dynamique du champ des contraintes mesuré dans les expériences et dans les simulations à partir de la seule donnée des profils d'écoulement[5,6].

Références :

1. Signatures of granular microstructure in dense shear flows. D. Mueth, G. Debregeas, G. Karczmar, P. Eng, S. Nagel & H. Jaeger, *Nature* 406, 385-388 (2000)
2. A self-similar model for shear flows in dense granular materials. G. Debrégeas and C. Josserand, *Europhys. Lett.*, 52 (2), pp. 137-143 (2000)
3. Deformation and Flow of a Two-Dimensional Foam under Continuous Shear. G. Debrégeas, H. Tabuteau, and J.-M di Meglio, *Phys. Rev. Lett.* 87(17) 178305 (2001)
4. Local Stress Relaxation and Shear Banding in a Dry Foam under Shear. A. Kabla and G. Debrégeas, *Phys. Rev. Lett.* 90(25) 258303 (2003)
5. Quasi-static rheology of foams. Part 1. Oscillating strain, A. Kabla and G. Debrégeas, *Journal of Fluid Mechanics*, 587 (2007), pp 23-44
6. Quasi-static rheology of foams. Part 2. Continuous shear flow, A. Kabla, J. Scheibert and G. Debrégeas, *Journal of Fluid Mechanics* 587 (2007), pp 45-72

damage[5]), and is strongly model-dependent[4]. Tougaard's approach[3] (quantitative analysis of signal-to-background correlation) requires minimal interference of neighbouring lines across a wide spectral range, and is therefore less effective with small signals. CSC is basically non-destructive, allowing fast and convenient data collection. It enables differentiation of spectrally identical atoms at different locations. It is applicable to thicker structures than ARXPS, as the signal is not subject to increased attenuation associated with off-normal measurements. Substrate roughness, severely affecting ARXPS depth analysis by smearing the angular scale, would only have a minor effect on CSC depth profiling. The linear dependence on depth, found in the present systems, is an attractive feature of CSC. Note, however, that other systems may involve more elaborate conduction processes, possibly causing deviations from linearity. Such deviations may allow the exploration of additional characteristics of the systems, such as charge distribution and conduction mechanisms.

As a high-resolution depth-profiling method, CSC is applicable to a large variety of non-conducting layers less than about 10 nm thick. Moreover, the present results suggest applications of CSC as a contactless electrical probe, capable of direct detection of local potentials in thin overlayers. In the light of recent progress in enhancing XPS lateral resolution, CSC may be an effective tool for studying three-dimensional nanostructures and molecular architectures. □

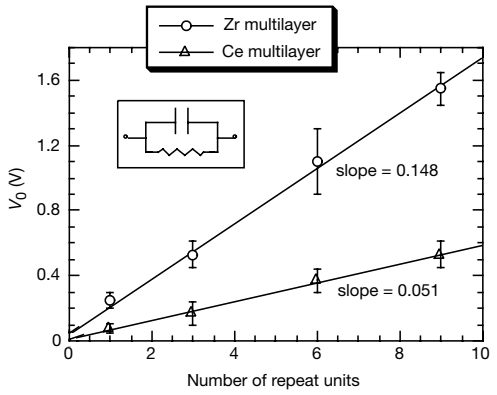

Figure 3 Plot of V_0 versus overlayer thickness. V_0 is the total potential difference across the overlayer, and the overlayer thickness is given as the number of molecular layers. V_0 is derived from the low-binding-energy side of the peaks of the respective ions. Inset, the electrical analogue of the overlayer, with a simple parallel-plate capacitor and a shunt resistor.

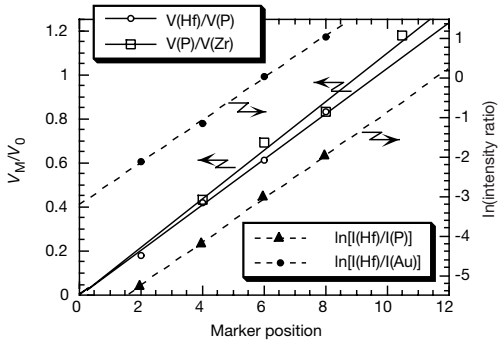

Figure 4 Depth profiling with accurately positioned markers. Solid lines show the normalized local potential of the 'moving' marker, V_M/V_0, versus marker position, for P and Hf markers in the multilayers shown in Fig. 1b and c, respectively (linear scale). Dashed lines show depth analysis via line intensities for the multilayers shown in Fig. 1c (log scale). The films with Hf(IV) in position 2 (Fig. 1c, left) displayed weak Hf signals that required second-derivative data processing for reliable determination of the energy shifts.

1. Briggs, D. & Seah, M. P. (eds) *Practical Surface Analysis* Vol. 1, 2nd edn (Wiley, New York, 1990).
2. Hofmann, S. in *Practical Surface Analysis* Vol. 1, 2nd edn (eds Briggs,D. & Seah, M. P.) 143–199 (Wiley, New York, 1990).
3. Tougaard, S. Quantitative analysis of the inelastic background in surface electron spectroscopy. *Surf. Interface Anal.* **11,** 453–472 (1988).
4. Tyler, B. J., Castner, D. G. & Ratner, B. D. Regularization—A stable and accurate method for generating depth profiles from angle-dependent XPS data. *Surf. Interface Anal.* **14,** 443–450 (1989).
5. Frydman, E., Cohen, H., Maoz, R. & Sagiv, J. Monolayer damage in XPS measurements as evaluated by independent methods. *Langmuir* **13,** 5089–5106 (1997).
6. Seah, M. P. in *Practical Surface Analysis* Vol. 1, 2nd edn (eds Briggs, D. & Seah, M. P.) 541–554 (Wiley, New York, 1990).
7. Tielsch, B. J., Fulghum, J. E. & Surman, D. J. Differential charging in XPS. 2. Sample mounting and x-ray flux effects on heterogeneous samples. *Surf. Interface Anal.* **24,** 459–468 (1996).
8. Barr, T. L. Studies in differential charging. *J. Vac. Sci. Technol. A* **7,** 1677–1683 (1989).
9. Lewis, R. T. & Kelley, M. A. Binding energy reference in XPS of insulators. *J. Electron Spectrosc. Relat. Phenom.* **20,** 105–115 (1980).
10. Miller, J. D., Harris, W. C. & Zajac, G. W. Composite interface analysis using voltage contrast XPS. *Surf. Interface Anal.* **20,** 977–983 (1993).
11. Beamson, G. *et al.* Characterization of PTFE on silicon wafer tribological transfer films by XPS, imaging XPS and AFM. *Surf. Interface Anal.* **24,** 204–210 (1996).
12. Barr, T. L. in *Practical Surface Analysis* Vol. 1, 2nd edn (eds Briggs, D. & Seah, M. P.) 370 (Wiley, New York, 1990).
13. Shabtai, K., Rubinstein, I., Cohen, S. & Cohen, H. High-resolution lateral differentiation using a macroscopic probe: XPS of organic monolayers on composite Au-SiO_2 surfaces. *J. Am. Chem. Soc.* **122,** 4959–4962 (2000).
14. Hatzor, A. *et al.* Coordination-controlled self-assembled multilayers on gold. *J. Am. Chem. Soc.* **120,** 13469–13477 (1998).
15. Moav, T. *et al.* Coordination-based symmetric and asymmetric bilayers on gold surfaces. *Chem. Eur. J.* **4,** 502–507 (1998).
16. Yang, H. C. *et al.* Growth and characterization of metal(II) alkanebisphosphonate multilayer thin-films on gold surface. *J. Am. Chem. Soc.* **115,** 11855–11862 (1993).
17. Hatzor, A. *et al.* A metal-ion coordinated hybrid multilayer. *Langmuir* **16,** 4420–4423 (2000).
18. Umemura, Y., Yamagishi, A. & Tanaka, K.-I. X-ray photoelectron spectroscopic study of alternately layered zirconium and hafnium phosphate thin films on silicon substrates. *Bull. Chem. Soc. Jpn* **70,** 2399–2403 (1997).

Received 14 March; accepted 26 May 2000.

Acknowledgements

This work was supported by the Israel Science Foundation, and the Tashtiot Infrastructure Program of the Israel Ministry of Science.

Correspondence and requests for materials should be addressed to I.R. (e-mail: israel.rubinstein@weizmann.ac.il). or H.C. (e-mail: cphagai@wis.weizmann.ac.il).

Signatures of granular microstructure in dense shear flows

Daniel M. Mueth*, Georges F. Debregeas*, Greg S. Karczmar†, Peter J. Eng‡, Sidney R. Nagel* & Heinrich M. Jaeger*

* *The James Franck Institute and Department of Physics,* †*Radiology Department,* ‡*Center for Advanced Radiation Sources (CARS), University of Chicago, 5640 South Ellis Avenue, Chicago, Illinois 60637, USA*

Granular materials and ordinary fluids react differently to shear stresses. Rather than deforming uniformly, materials such as dry sand or cohesionless powders develop shear bands[1–5]—narrow zones of large relative particle motion, with essentially rigid adjacent regions. Because shear bands mark areas of flow, material failure and energy dissipation, they are important in many industrial, civil engineering and geophysical processes[6]. They are also relevant to lubricating fluids confined to ultrathin molecular layers[7]. However, detailed three-dimensional information on motion within a shear band, including the degree of particle rotation and interparticle slip, is lacking. Similarly, very little is known about how the microstructure of individual grains affects movement in densely packed material[5]. Here we combine

© 2000 Macmillan Magazines Ltd

magnetic resonance imaging, X-ray tomography and high-speed-video particle tracking to obtain the local steady-state particle velocity, rotation and packing density for shear flow in a three-dimensional Couette geometry. We find that key characteristics of the granular microstructure determine the shape of the velocity profile.

In order to probe the role of microstructure inside the narrow granular shear zone, independent determinations are required of the velocity and density profiles with spatial resolution well below the size of individual particles. Non-invasive measurements of this type so far have been limited to two-dimensional (2D) geometries where optical tracking of all particle positions is straightforward[2,4,8–11]. In a three-dimensional (3D) Couette cell, as sketched in Fig. 1a, a steady-state shear flow can be set up by confining granular material between two concentric, vertical cylinders and turning the inner cylinder at constant velocity v_{wall} while keeping the outer wall at rest. Unlike 2D Couette cells[9,10,12], where particles are confined to a single layer with constant volume, there is a free upper surface allowing the packing density to adjust via feedback between shear-induced dilation and gravity.

The difficulty of imaging the interior has restricted studies of 3D granular Couette systems; such studies have probed only the surface (including its velocity fluctuations)[13], or tracked coloured tracers in very narrow (a few particles wide) cells[14], or measured global quantities, such as the total applied torque. Here we use magnetic resonance imaging (MRI) to obtain flow velocities from the interior of a 3D system[15,16]. We have used oil-rich seeds as a source of free protons that can be traced using MRI[15]. Two kinds of seeds were used to explore the role of microstructure: mustard seeds (spherical with mean diameter $d = 1.8$ mm) and poppy seeds (kidney-shaped with mean diameter $d = 0.8$ mm). The wall friction was controlled by gluing a layer of seeds on both cylinders. Using a spin-tagging technique, horizontal slices were imaged, as sketched in Fig. 1a. In the resulting MRI image (Fig. 1b), the shear band shows up as the narrow region of deformed stripes near the inner, moving, cylinder. Imaging slices at different heights, h, we measured these deformations, from which the azimuthal velocity profiles were calculated throughout the cell. Similarly, 3D X-ray tomography (Fig. 1d) allowed us to calculate packing-fraction profiles at various heights. At the transparent cell bottom, additional velocity and packing-fraction information was gathered by direct, high-speed-video particle tracking (Fig. 1c).

Before each set of measurements, the cell was run until steady state was reached (as determined by the fact that the packing density profiles became stationary). High-resolution images revealed the long-time average local displacements during a time interval, $\delta t = 100$ ms. Figure 1b represents such displacements averaged over a 17-min acquisition time. The azimuthal velocity at a given distance r from the inner wall was obtained by exploiting the cylindrical symmetry of the Couette geometry: we calculated the MRI intensities along a circle of radius r, $I_{turning}(\theta)$ and $I_{stopped}(\theta)$, for the cell turning and at rest, respectively. The position of the central peak in the cross-correlation between $I_{turning}(\theta)$ and $I_{stopped}(\theta)$ corresponds to the average azimuthal distance travelled by the material during δt. This technique yielded the angle- and time-averaged radial profile of the steady-state azimuthal mass flow velocity, $v(r)$, resolving $v(r)$ to within 0.1 mm s^{-1} and r to within 0.1mm. We note that this high-resolution mass flow velocity is the average velocity of all material at radius r and thus not only contains information about particle translation, but also about particle spin. This differs from the

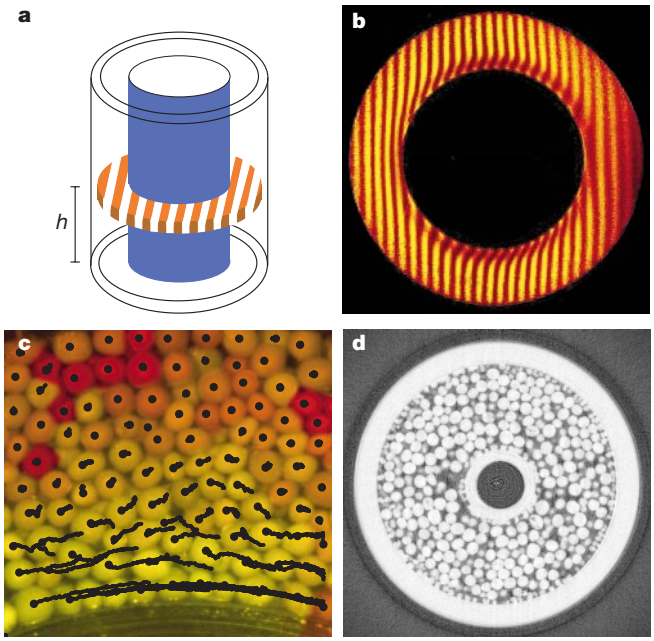

Figure 1 Non-invasive MRI, X-ray tomography and high-speed-video probes of granular Couette flow. **a**, Sketch of the Couette-type shear cell consisting of two concentric cylinders with diameters 51 mm and 82 mm, and filled to a level of 60 mm. The inner cylinder was rotated at velocities 0.6 mm s^{-1} < v_{wall} < 120 mm s^{-1}. The flow velocity was measured using an MRI spin-tagging technique[14,15]. Before imaging, proton spins were encoded (spin-tagged) so as to display parallel stripes when imaged. Images were taken of 5-mm-thick horizontal slices at various heights, h. **b**, When the inner cylinder was rotated, distortion of the stripe pattern revealed the displacement of the material that occurred during the 100-ms interval between spin-tagging and imaging. 2,048 spin-tag-image steps were used to assemble each complete image. **c**, High-speed-video frame, taken at 1/1,000 s, of mustard seeds observed through the cell's transparent bottom. To indicate the movement history of individual particles, their centre positions over the preceding 200 frames are traced by black lines. The particle colouring reflects the magnitude of each particle's average velocity during this 0.2-s interval: fast particles (yellow) near the inner wall appear to move smoothly, while slower particles (orange and red) display more irregular and intermittent motion. In the long-time average, measured by the MRI technique, the flow appears smooth everywhere. **d**, Two-dimensional, horizontal slice through the cell at half the filling height, taken from the X-ray tomography data set. Particles, in this case mustard seeds, appear bright (as do the walls of the cell). These measurements were performed at the Advanced Photon Source at Argonne National Laboratory in a Couette cell of slightly smaller size but under otherwise identical shearing conditions.

© 2000 Macmillan Magazines Ltd

average velocity of particle centres that typically is obtained by video particle-tracking techniques.

We found $v(r)$ highly reproducible from run to run, even though on shorter timescales there are rapid velocity fluctuations from point to point within the material that, at the top and bottom boundaries, can be observed with high-speed video (Fig. 1c). Within the resolution of our measurements, $v(r)$ for both types of seeds did not vary with height, including the regions near the top and bottom surfaces. (We note that this indicates that non-azimuthal, secondary flow was small and did not affect $v(r)$, in accordance with tracer-bead studies[13].) Apart from an overall scale factor, we also did not detect any shear-rate dependence to the velocity profile over the entire range $5\,\mathrm{mm\,s^{-1}} < v_{\mathrm{wall}} < 120\,\mathrm{mm\,s^{-1}}$ explored with MRI. (With video imaging we verified rate independence down to velocities as small as $0.6\,\mathrm{mm\,s^{-1}}$).

For (nearly) monodisperse smooth, spherical particles, the decay of $v(r)$ away from the shearing wall is dominated by abrupt drops at integer multiples of r/d as shown in Fig. 2a for mustard seeds. In the normalized velocity gradient $\gamma(r) \equiv (d/v)\,\partial v/\partial r$ (Fig. 2b) these drops appear as deep narrow valleys. They are correlated with pronounced oscillations in the packing density, $\rho(r)$, which signal the presence of well defined, single-grain-wide layers near the moving wall (Fig. 2c).

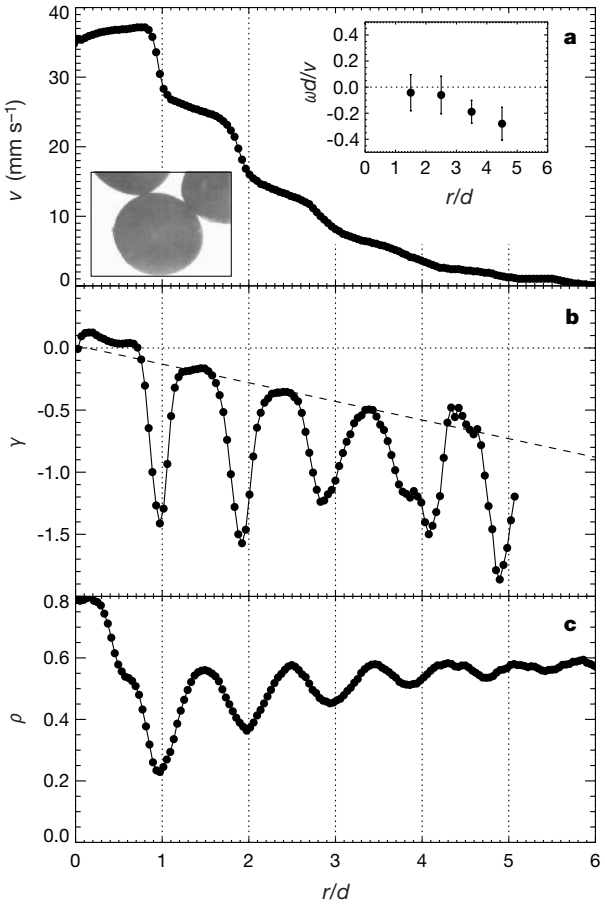

Figure 2 Radial profiles of azimuthal velocity, spin and packing density for spherical mustard seeds. **a**, Steady-state, angle-averaged azimuthal velocity $v(r)$ across the shear band at $h = 30$ mm, halfway below the filling level. The layer of seeds glued to the inner cylinder wall extends to the dotted vertical line at $r/d = 1$. The lower inset shows a photograph of the seeds. The upper inset shows the normalized particle spin rate, $\omega d/v$, as a function of distance from the moving wall (where ω is the angular velocity of a particle about its centre). **b**, Normalized velocity gradient $\gamma \equiv (d/v)\partial v/\partial r$ for the data in the main panel of **a**. **c,** Angle-averaged, steady-state radial packing density profile $\rho(r)$ computed from X-ray tomography data as in Fig. 1d, measuring the volume fraction occupied by seed material. For $0 < r/d < 1$, the seeds glued to the wall contribute to ρ.

(We note that the average density approaches the random close packing value at larger r in a manner that is consistent with an exponential form[10].) The shear-induced layering is reminiscent of that seen[17] in the collisional regime of dilute flows, but occurs here in the high-density limit of rate-independent, frictional flow. Because the velocity drops are highly localized, we associate them with slipping at the interface between adjacent layers. Either directly from $v(r)$ or by comparing the integrated areas of each valley in $\gamma(r)$ we find that across each slip zone the velocity decreases by approximately the same factor, $b = 0.36 \pm 0.13$.

In addition to slip between layers, MRI resolves a non-zero velocity gradient $\gamma(r)$ within each layer. This could be caused by either particle rotation or disorder in the layering along the radial direction. (Along the azimuthal and axial directions, particles within layers certainly show packing disorder—as can be seen from the maxima in $\rho(r)$ in Figs 2c and 3c, whose values lie significantly below those for a crystalline configuration). For perfectly arranged layers, $\gamma(r)$ at the layer centres would be determined solely by particle rotation (spin) within each layer. The presence of particles which do not lie perfectly within the layers (revealed by the non-zero values of $\rho(r)$ between layers in Fig. 2c and seen directly from the tracks in Fig. 1c) reduces the gradient in the slip region and increases it at the layer centres. In the limit of complete disorder, we would expect the staircase shape of $v(r)$ to vanish completely. Using information about the density, $\rho_c(r)$, and velocity, $v_c(r)$, of the particle centres, as determined by the high-speed-video and X-ray experiments, we find that approximately 90% of $\gamma(r)$ at the layer centres is due to the radial disorder. In order

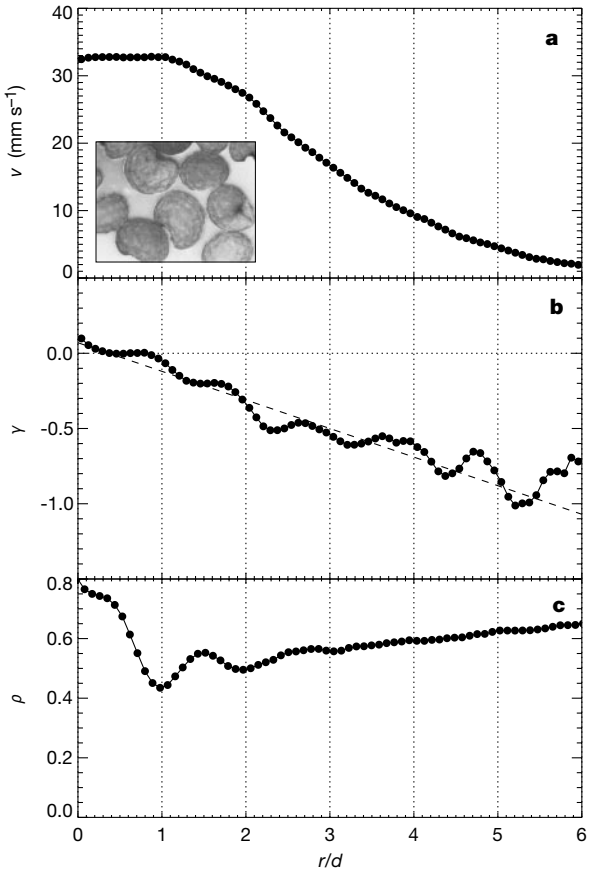

Figure 3 Radial profiles of azimuthal velocity, spin and packing density for aspherical poppy seeds. **a**, Steady-state, angle-averaged azimuthal velocity $v(r)$ across the shear band at $h = 30$ mm. The inset shows a photograph of the seeds. **b**, Normalized velocity gradient for the data in **a**. **c**, Corresponding angle-averaged, radial packing density profile $\rho(r)$ from X-ray data. For $0 < r/d < 1$, the seeds glued to the wall contribute to ρ.

© 2000 Macmillan Magazines Ltd

for the MRI and high-speed-video experiments to give the same $\gamma(r)$, particle spin must be considered, revealing the spin profile seen in the inset of Fig. 2a. We note that the spin is small, increasing slowly with distance from the shearing wall to a value at $r/d = 4.5$ of less than one full particle rotation per $13d$ translation.

The message of Fig. 2 is that the overall shape of $v(r)$ across the shear band can be understood as arising from two main contributions to the velocity gradient $\gamma(r)$: a slip contribution in the presence of layering, and a second contribution associated with radial disorder. These two pieces are distinguished by the characteristic r-dependence they produce in $v(r)$ on length scales larger than a single grain. A constant slipping fraction, $\int_{\text{interface}}\gamma_{\text{slip}}(r)\mathrm{d}r = -b$, across each interface leads (by itself) to a velocity profile with an exponential decay, $v(r) = v_o\exp(-br/d)$. The constant inter-layer slip appears on a background due to radial disorder, $\gamma_{\text{disorder}}(r) = -2c(r-r_o)/d$, that starts at r_o within the glued-on layer and increases linearly in strength with slope $2c$ as indicated by the dotted line in Fig. 2b). Such linear r-dependence in $\gamma(r)$ results in a gaussian profile, $v(r) = v_o\exp(-c(r/d - r_o/d)^2)$. The sum of the two contributions to $\gamma(r)$, after integration, leads to a product of an exponential and gaussian term for the overall, averaged velocity profile: $v(r) = v_o\exp[-br/d - c(r/d - r_o/d)^2]$. Fits of this function to mustard-seed data yield $b = 0.36 \pm 0.13$, $c = 0.06 \pm 0.03$ and $r_o/d = 0.6 \pm 0.8$ independent of height and shear rate.

The decomposition of $\gamma(r)$ allows the quantitative tracking of the slip inside the shear band for different particle types. We find a greatly reduced slip rate b when smooth spherical particles are replaced by roughened ones. More dramatic differences result from changes in the particle shape. For kidney-shaped poppy seeds we observe a comparatively smooth overall velocity profile (Fig. 3a). Much smaller modulations in $\gamma(r)$ (Fig. 3b) together with little layering in $\rho(r)$ (Fig. 3c) indicate that interlayer slip is greatly reduced. The linear trend $\gamma(r) = -2c(r/d - r_o/d)$ is still present, however, and leads to the gaussian shape for $v(r)$ seen in Fig. 4 over several orders of magnitude. These data also demonstrate explicitly that the shear rate fixed by v_{wall}, while setting the overall scale, leaves the shape of the profile unchanged. This allows for a collapse of all poppy-seed data for different shear rates and heights in the cell onto a single gaussian described by $c = 0.11 \pm 0.02$ and $r_o/d = -0.1 \pm 0.5$. Layering can also be suppressed and radial disorder be promoted in sphere packings if wide particle size distributions are used. We find that these, too, produce essentially gaussian velocity profiles.

From these results, the gaussian component of the velocity profile emerges as a robust, generic feature; slip, if it occurs, is seen to augment $v(r)$ by an additional, exponential factor. In contrast to the translationally invariant slip, the explicit dependence of the gaussian on the distance from the shearing wall indicates correlations. There are several possible mechanisms for radial correlations[5,9,10,18–20], including the formation of stress chains[5,9,10] or particle clusters[18,20], both of which require high packing densities and the absence of slip or some degree of interlocking. However, a detailed mechanism that would explain the observed gaussian dependence does not exist at present. A successful theory must not only account for the linear increase in the magnitude of the velocity gradient with r, but also show how the gaussian shape is independent of the presence of layering. We speculate that both of these might be provided by a coupling of $\gamma(r)$ to the average packing fraction and its gradients (for 2D Couette systems, a coupling to the average density alone has been suggested[9,10]). A gaussian, then, arises naturally for a coupling of type $\gamma(r) \propto \rho(r_o) - \rho(r)$, considering first-order terms in r. Because all stress-loading is driven by the seed layer glued to the inner wall, its location, r_o, serves as a spatial reference point. This argument carries over to the absence of a gaussian contribution to $v(r)$ in less-dense types of flow, where interlocking may be less effective, such as rapid flows down inclines with free upper surface for which power-law forms have been reported[4,15,21], or vertical gravity-driven flows through 2D 'pipes', which appear to follow essentially exponential profiles[2,22].

Our results show that, in this regime of high packing density and slow shearing rate, there is a direct connection between the microstructure and the shape of the velocity profile. For equal-sized spherical particles, where considerable layering is found, a strong exponential contribution is observed. For aspherical seeds, which show no pronounced layering, the profile is almost completely described by a gaussian centred on the shearing wall. But despite the complicated nature of the grain–grain interactions, the steady-state velocity profile exhibits robust behaviour: its shape—characterized by the two length scales, $\lambda = d/b$ and $\sigma = d/c^{1/2}$—is found to be independent of both height and shear-rate. □

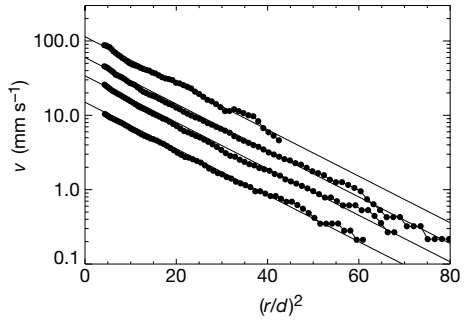

Figure 4 Rate-independence of the velocity profiles. Shown is a log plot of poppy-seed velocity profiles $v(r)$ as a function of $(r/d)^2$ for four different shearing wall speeds ($v_{\text{wall}} = 120$, 52, 33 and 14 mm s^{-1}, top to bottom). Straight lines on this plot correspond to a gaussian with origin at $r = 0$. The slope, c, of these lines corresponds to half the average slope of the velocity gradient in Fig. 3b and characterizes the width $\sigma = d/c^{1/2}$ of the shear band.

Received 13 December 1999; accepted 7 June 2000.

1. Bridgwater, J. On the width of failure zones. *Géotechnique* **30,** 533–536 (1980).
2. Nedderman, R. M. & Laohakul, C. The thickness of the shear zone of flowing granular materials. *Powder Technol.* **25,** 91–100 (1980).
3. Mühlhaus, H.-B. & Vardoulakis, I. The thickness of shear bands in granular materials. *Géotechnique* **37,** 271–283 (1987).
4. Drake, T. G. Structural features in granular flows. *J. Geophys. Res.* **95,** 8681–8696 (1990).
5. Oda, M. & Kazama, H. Microstructure of shear bands and its relation to the mechanism of dilatancy and failure of dense granular material. *Géotechnique* **48,** 465–481 (1998).
6. Scott, D. R. Seismicity and stress rotation in a granular model of the brittle crust. *Nature* **381,** 592–595 (1996).
7. Grannick, S. Soft matter in a tight spot. *Phys. Today* **52,** 26–31 (1999).
8. Tüzün, U. & Nedderman, R. M. An investigation of the flow boundary during steady-state discharge from a funnel-flow bunker. *Powder Technol.* **31,** 27–43 (1982).
9. Howell, D., Behringer, R. P. & Veje, C. Stress fluctuations in a 2D granular Couette experiment: a continuous transition. *Phys. Rev. Lett.* **82,** 5241–5244 (1999).
10. Veje, C. T., Howell, D. W. & Behringer, R. P. Kinematics of a two-dimensional granular Couette experiment at the transition to shearing. *Phys. Rev. E* **59,** 739–745 (1999).
11. Rajchenbach, J. Granular flows. *Adv. Phys.* **49,** 229–256 (2000).
12. Karion, A. & Hunt, M. L. Wall stresses in granular Couette flows of mono-sized particles and binary mixtures. *Powder Technol.* **109,** 145–163 (2000).
13. Losert, W., Bocquet, L., Lubensky, T. C. & Gollub, J. Partical dynamics in sheared granular matter. Preprint cond-mat/0004401 at ⟨http://xxx.lanl.gov⟩ (24 April 2000).
14. Khosropour, R., Zirinsky, J., Pak, H. K. & Behringer, R. P. Convection and size segregation in a Couette flow of granular material. *Phys. Rev. E* **56,** 4467–4473 (1997).
15. Fukushima, E. Nuclear magnetic resonance as a tool to study flow. *Annu. Rev. Fluid Mech.* **31,** 95–123 (1999).
16. Ehrichs, E. E. *et al.* Granular convection observed by magnetic resonance imaging. *Science* **267,** 1632–1634 (1995).
17. Hopkins, M. A., Jenkins, J. T. & Louge, M. Y. On the structure of three-dimensional shear flows. *Mech. Mater.* **16,** 179–188 (1993).
18. Debregeas, G. & Josserand, C. A self-similar model for shear flows in dense granular material. Preprint cond-mat/9901336 (cited 24 Feb. 2000) at ⟨http://xxx.lanl.gov⟩ (1999).
19. Tkachenko, A. & Putkaradze, V. Mesoscopic physics of granular flows. Preprint cond-mat/9912187 (cited 10 Dec. 1999) at ⟨http://xxx.lanl.gov⟩ (1999).
20. Josserand, C. A 2D asymmetric exclusion model for granular flows. *Europhys. Lett.* **48,** 36–42 (1999).
21. Hanes, D. M. & Inman, D. L. Observations of rapidly flowing granular-fluid materials. *J. Fluid Mech.* **150,** 357–380 (1985).
22. Pouliquen, O. & Gutfraind, R. Stress fluctuations and shear zones in quasi-static granular chute flows. *Phys. Rev. E* **53,** 557–561 (1996).

Acknowledgements

We thank E. Fukushima, J. Jenkins, C. Josserand, D. Levine, M. Medved, V. Putkaradze,

© 2000 Macmillan Magazines Ltd

M. Rivers and A. Tkachenko for discussions, and D. Stockwell for the donation of mustard seeds for the experiment. G.F.D. acknowledges a postdoctoral Grainger Fellowship. This work was supported by an NSF research grant and by the MRSEC program of the NSF.

Correspondence and requests for materials should be addressed to H.M.J. (e-mail: h-jaeger@uchicago.edu).

Oscillatory cluster patterns in a homogeneous chemical system with global feedback

Vladimir K. Vanag, Lingfa Yang, Milos Dolnik, Anatol M. Zhabotinsky & Irving R. Epstein

Department of Chemistry and Volen Center for Complex Systems, MS 015, Brandeis University, Waltham, Massachusetts 02454-9110, USA

Oscillatory clusters are sets of domains in which nearly all elements in a given domain oscillate with the same amplitude and phase[1–4]. They play an important role in understanding coupled neuron systems[5–8]. In the simplest case, a system consists of two clusters that oscillate in antiphase and can each occupy multiple fixed spatial domains. Examples of cluster behaviour in extended chemical systems are rare, but have been shown to resemble standing waves[9–13], except that they lack a characteristic wavelength. Here we report the observation of so-called 'localized clusters'—periodic antiphase oscillations in one part of the medium, while the remainder appears uniform—in the Belousov–Zhabotinsky reaction–diffusion system with photochemical global feedback. We also observe standing clusters with fixed spatial domains that oscillate periodically in time and occupy the entire medium, and irregular clusters with no periodicity in either space or time, with standing clusters transforming into irregular clusters and then into localized clusters as the strength of the global negative feedback is gradually increased. By incorporating the effects of global feedback into a model of the reaction, we are able to simulate successfully the experimental data.

The Belousov–Zhabotinsky (BZ) reaction is the best studied chemical oscillator; its dynamics resemble those of many important biological and physical nonlinear oscillators[14–19]. The reaction consists of the oxidation of malonic acid by bromate, catalysed by metal ions or metallo-complexes in acidic aqueous solution.

Here we study pattern formation in the photosensitive $Ru(bpy)_3$-catalysed BZ reaction[20–22] in a thin layer of silica gel[23,24] with photochemical global negative feedback imposed through illumination (see Fig. 1). The average concentration of $Ru(bpy)_3^{3+}$, Z_{av}, taken over the working area of the gel, is employed to control the intensity I of actinic light (from lamp L2), according to $I = I_{max}\sin^2(g(Z_{av} - Z_t))$, where g is the feedback coefficient and Z_t is a target concentration. The target Z_t is varied by changing the reference voltage (RV) and is set close to the steady state value, Z_{ss}, in such a way that the difference $Z_{av} - Z_t$ is always positive. The angle between polarizers P1 and P2 (that is, $g(Z_{av} - Z_t)$) is not allowed to exceed $\pi/2$. The gain of amplifier A5 is used to control the feedback coefficient g. The actinic light produces bromide ion[21], which inhibits the oxidation of $Ru(bpy)_3^{2+}$.

We investigate how pattern formation depends on g. We choose the initial reagent concentrations in such a way that without any feedback the system generates bulk oscillations. Various travelling wave patterns are found when g is less than $g^\star$, a value that depends on the initial concentrations of reagents. In most cases, $1 \times 10^4\,M^{-1} < g^\star < 2 \times 10^4\,M^{-1}$. When the feedback coefficient is slightly above $g^\star$, either travelling wave patterns or cluster patterns are observed, depending on the initial conditions. The width of this bistability range depends on the initial reagent concentrations.

When g exceeds $2 \times 10^4\,M^{-1}$, standing clusters arise. Figure 2 depicts several patterns of such clusters. Figure 2a shows one period of oscillation of a pattern that arose from initial conditions created by brief illumination of the gel through a striped mask. At $t = 4$ s, Z_{av} reaches a maximum. After this instant, the white domains start to fade and the system gradually evolves to the uniform reduced (dark) state. During the second half-period, the regions that were dark during the first half-period become bright, and at $t = 29$ s the pattern displays another maximum in Z_{av}. As adjacent domains oscillate in antiphase, the period, T_{av}, of oscillations of Z_{av} is half the period of the local oscillations. Figures 2b and 2c show patterns that developed from a spiral wave and from uniform initial conditions, respectively. Other patterns of standing clusters can be obtained by varying the initial conditions. Standing clusters do not possess intrinsic spatial periodicity, because the global feedback is sensitive only to the spatially integrated characteristics of the patterns.

At larger g, two other types of patterns arise. If the initial reagent concentrations lie far from the boundary of the oscillatory region of the parameter space, we observe a transition from standing clusters

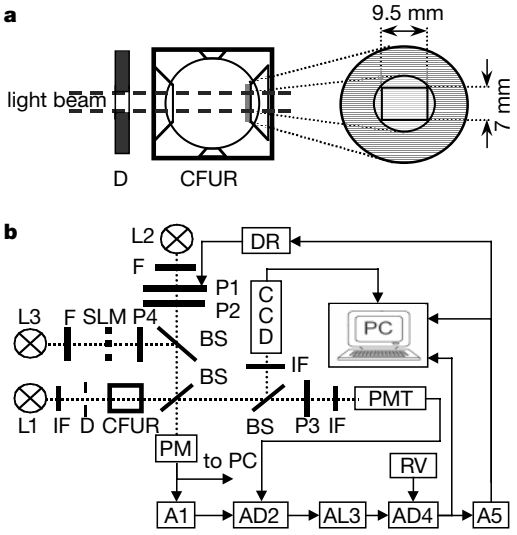

Figure 1 Experimental set-up. **a**, The continuously fed unstirred reactor (CFUR) consists of a 24-ml continuously stirred tank reactor thermostated at 25 °C and a thin layer of silica gel polymerized on the reactor optical window (grey circle). The 0.413-mm-thick gel has diameter 22 mm, and contains 1.5 mM of immobilized Tris(2,2′-bipyridyl)ruthenium(II)($Ru(bpy)_3^{2+}$. Diaphragm D selects an illuminated working area of gel (light grey circle). The rectangular frame shows the field of view of the CCD camera. A peristaltic pump injects stock solutions of KBr, malonic acid, $NaBrO_3$ and H_2SO_4 into a premixing chamber (not shown) and then into the CFUR. **b**, Low-intensity analysing light from the stabilized 45-W light source (L1) passes through the working area of the gel, and is collected by a lens and directed to the photomultiplier tube (PMT). AD2 and AD4 are differential amplifiers, AL3 is a logarithmic amplifier, A5 is a d.c. amplifier. The driver (DR) rotates polarizer P1, and controls the intensity of actinic light from the 450-W Xe arc lamp (L2). P1–P4 are polarizers, IFs are interference filters with $\lambda_{max} = 450$ nm, Fs are bandpass filters (400–500 nm), BSs are beam splitters; lenses and collimators are not shown. The 150-W Xe arc lamp (L3) serves to set patterns of initial conditions. An image of the spatial light modulator (SLM) is focused in the plane of the silica gel. Actinic light intensity (I) is measured by the power meter (PM). Polarizers P2-P3 and P4-P3 are crossed to separate optical channels. The remaining parasitic signal from scattered actinic light is compensated electronically by amplifiers A1 and AD2, and stays below 1% of the photomultiplier working signal when I varies from 0 to $I_{max} = 4.3\,mW\,cm^{-2}$. Uniformity of illumination of the working area is better than 2%.

© 2000 Macmillan Magazines Ltd

Deformation and Flow of a Two-Dimensional Foam under Continuous Shear

G. Debrégeas,* H. Tabuteau, and J.-M di Meglio†

Institut Charles Sadron, CNRS UPR 022, 6 rue Boussingault, 67083 Strasbourg Cedex, France

(Received 21 March 2001; published 9 October 2001)

We investigate the flow properties of a 2D foam (a confined monolayer of jammed bubbles) submitted to a continuous shear in a Couette geometry. A strong localization of the flow at the moving inner wall is evidenced. Moreover, velocity fluctuations measurements reveal self-similar dynamical structures consisting of clusters of bubbles moving coherently. A stochastic model is proposed where bubbles rearrangements are activated by local stress fluctuations produced by the shearing wheel. This model gives a complete description of our observations and is also consistent with available data on granular shear bands.

DOI: 10.1103/PhysRevLett.87.178305 PACS numbers: 82.70.Rr, 83.80.Iz

Disordered systems, such as foams, concentrated emulsions, slurries, or granular materials, exhibit rheological properties that cannot be understood within the scope of standard solid or liquid mechanics [1–3]. For such systems, thermal energies are orders of magnitude lower than the typical energy required to relax the structural arrangements of their components; under small forces, the material remains trapped in a metastable configuration and exhibits a solidlike behavior. However, when submitted to a large enough stress, it can be driven through a series of new metastable configurations, giving rise to a macroscopic flow. But the resulting flow field may still differ a lot from what would be expected for a molecular liquid.

Dry sand slowly flowing down an hour glass provides a simple example of such abnormal flow behaviors: the flow splits into a pluglike central region and a strongly sheared thin layer at the wall — a few particles wide — where most of the dissipative process occurs [4]. This spontaneous localization of the strain in narrow regions (the so-called shear bands) can be observed in many other situations such as shear, surface or convective flows for instance [5–8]. Shear banding actually controls most of the practical situations encountered in soil mechanics and industrial handling of grains, and is also relevant to pyroclastic flows in geology (for a review on granular matter, see [9]). This question has recently received a lot of attention from physicists, both theoretically and experimentally [10,11], but a clear picture has not emerged yet.

By contrast, the possibility of shear banding in foams has been mostly ignored in the literature, and numerical or theoretical studies usually assume shear flows in foams to be uniform [2,12]. The assumption that shear banding is unique to granular matter can be misleading because it suggests that some peculiar aspects of granular flows, such as solid friction, particle rotation, or dilatancy, are essential.

In this Letter, we report the formation of shear bands in aqueous foams. We believe that foams may shed light on the dynamics of granular systems by evidencing the minimal set of ingredients needed to get shear banding. To that extent, foams constitute a much simpler model than granular systems since the basic bubble/bubble interactions which control the mechanical properties of the material are well known: elastic (stored) energy is related to an increase of the total interfacial area when the bubbles are distorted, whereas dissipated energy is associated with neighbors swapping events (T_1 processes) inducing flows in the liquid films and vertices (for a review on foams, see [13]).

In order to probe the microdynamics of the foam, one needs to track the trajectory of each bubble. Since 3D foams are inherently diffusive to light, we used a 2D model foam — a confined monolayer of bubbles — submitted to a continuous slow shear in a wide-gap Couette geometry. The setup was composed of an inner shearing wheel and an outer ring (of respective radius $R_0 = 71$ mm and $R_1 = 122$ mm) confined between two transparent plates separated by a 2 mm gap. To produce the foam, the cell was first held vertically and partially filled with a known volume of soap/water solution. Bubbles were formed by blowing nitrogen gas through two small injection holes at different flow rates until the resulting foam reached the top of the cell. Once set horizontally, the foam rapidly attained a uniform wetness characterized by its liquid fraction $0.01 < \phi < 0.3$ (Fig. 1). This foaming procedure was chosen because it produces bidisperse disordered foams and therefore eliminates crystallization. The mean diameters within each of the two populations of bubbles were of the order of 2 and 2.7 mm, with a mean deviation of 0.2 mm. These bubbles were large enough compared to the gap height so that they would not overlap. To define a bubble scale, we measured the mean distance d between first neighbors in the foam. We kept $2.1 < d < 2.5$ mm so that the gap between the wheel and the ring could accommodate from 20 to 25 rows of bubbles. The distance d was evaluated several times during the experiment and found to be almost constant. Coarsening would eventually lead to a growth of the biggest bubbles at the expense of the smallest ones but over a longer time. We also checked the absence of shear induced size segregation that might have occurred during the experiment.

Shearing was induced by rotating the inner wheel at constant velocity V_{wheel} using a stepper motor. To avoid

 © 2001 The American Physical Society

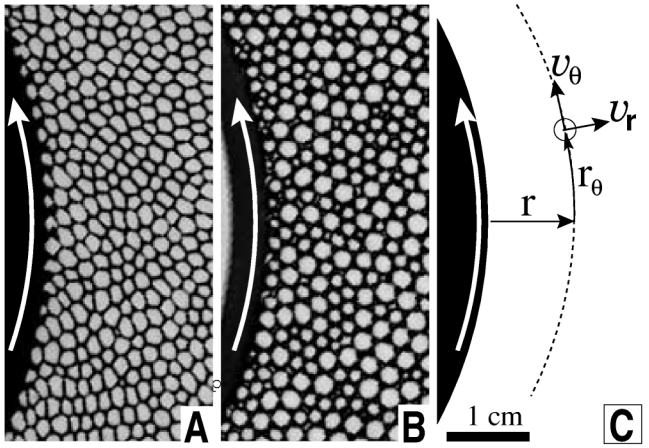

FIG. 1. Close-up frames of dry and wet 2D foams under continuous shear. The shearing wheel appears in black. Arrows indicate the inner wheel direction of rotation. (**A**) A dry bidisperse foam ($\phi = 0.05$), showing deformed polygonal cells. (**B**) A wet bidisperse foam ($\phi = 0.20$). The bubbles are circular and undeformed. (**C**) System of coordinates used to analyze the flow field.

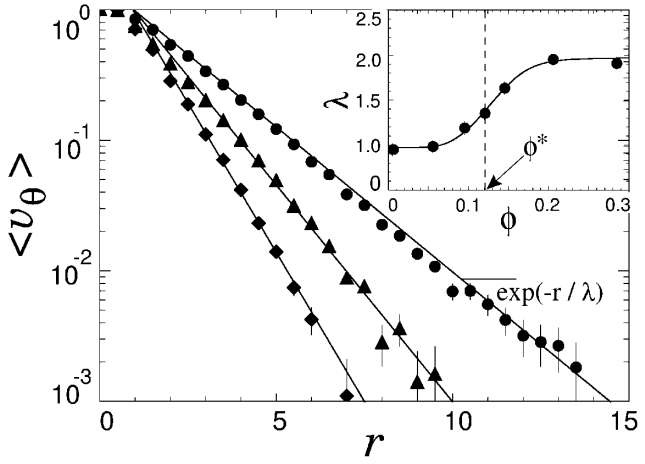

FIG. 2. Average tangential velocity profiles for different liquid fraction (◆: $\phi = 0.05$; ▲: $\phi = 0.12$; •: $\phi = 0.20$), showing exponential decays with a width $\lambda(\phi)$. The small plateau for $0 < r < 1$ corresponds to the first row of bubbles being attached to the shearing wheel. Inset: Dependence of λ on liquid fractions ϕ (the line is just a guide for the eyes). Two plateaus can be distinguished on either side of $\phi^* \simeq 0.12$, which separate polygonal and circular bubbles regimes.

slippage at the wheel and the ring, their sides were tooth shaped so that the first and last rows of bubbles would remain irreversibly attached to the walls. To eliminate transient effects, we ran the experiment a full round before taking data. The motion of 1000 to 1500 bubbles was then recorded using a CCD digital camera positioned over the setup. In a typical experiment, 3000 images were taken corresponding to a total displacement of $600d$ of the wheel edge. The apparent centers of mass of the bubbles were subsequently tracked by image analysis (IDL software). To reduce the effect of the viscous friction between the bubbles and the confining plates, we restricted our study to quasistatic flows. We focused on average velocity measurements as a probe of shear rate dependence: we found that in the range $0 < V_{\text{wheel}} < 0.7$ mm $\cdot$ s^{-1}, the velocity profiles were similar apart from an overall scale factor. All experiments were performed in the quasistatic regime at $V_{\text{wheel}} = 0.25$ mm $\cdot$ s^{-1}. In the following, all velocities and distances are normalized by V_{wheel} and d, respectively. We note $\omega_0 = V_{\text{wheel}}/d$ the characteristic frequency of the shear.

Figure 2(A) shows the decay of the average tangential velocity $\langle v_\theta(r) \rangle$ with the distance r to the shearing wheel for different liquid fractions ϕ [see Fig. 1(C) for variables definition]. Averaging was performed over the tangential coordinate r_θ and time t, yielding smooth and reproducible profiles, although the instantaneous flow is strongly intermittent. The reduced velocity is found to approach 1 at $r \to 0$ confirming the absence of slip at the edge of the wheel. At larger r, the profiles exhibit an exponential decay

$$\langle v_\theta(r) \rangle \sim \exp(-r/\lambda), \tag{1}$$

with a width λ depending on ϕ. The curve λ versus ϕ, presented in Fig. 2 (inset), shows two plateaus at low and high volume fraction. The transition between these two regimes occurs around $\phi^* = 0.12$, which qualitatively marks the limit between dry foams with polygonal bubbles for $\phi < \phi^*$ and wet foams with circular bubbles for $\phi > \phi^*$. In both cases, the rapid decay of the mean velocity over a few bubble diameters establishes the existence of shear banding in foams. The exponential shape of the velocity profile, observed in all experiments, appears as a robust feature which was also observed in comparable experiments performed on 2D granular materials [4,5,14].

Beyond these time averaged profiles, our setup allows measurements of the short time scale fluctuations of the bubbles velocities. A mere observation of the video sequences reveals brief oscillations of clusters of bubbles of various radial extension, rotating together as rigid bodies as shown in Fig. 3. These dynamical structures are ephemeral and disappear after the wheel edge has moved by roughly one bubble diameter (this was checked by measuring time correlations of the velocity which decay to 0 in a time of order $1/\omega_0$). To quantitatively probe these coherent moves, we studied the spatial correlations of the instantaneous velocity field. We focused on the radial component v_r which has a zero time average and therefore gives a better signal to noise ratio (qualitatively, similar results were found when using $v_\theta - \langle v_\theta \rangle$ instead of v_r). Figure 4(A) shows the correlation function $g_r(\Delta r_\theta) = \langle v_r(r, r_\theta) \cdot v_r(r, r_\theta + \Delta r_\theta) \rangle / \langle v_r^2(r) \rangle$ for different values of r from 1 to 10, at a volume fraction $\phi = 0.20$. Regardless of r, g_r decreases with Δr_θ from 1 to a negative value then slowly relaxes to 0. The length $\xi(r)$

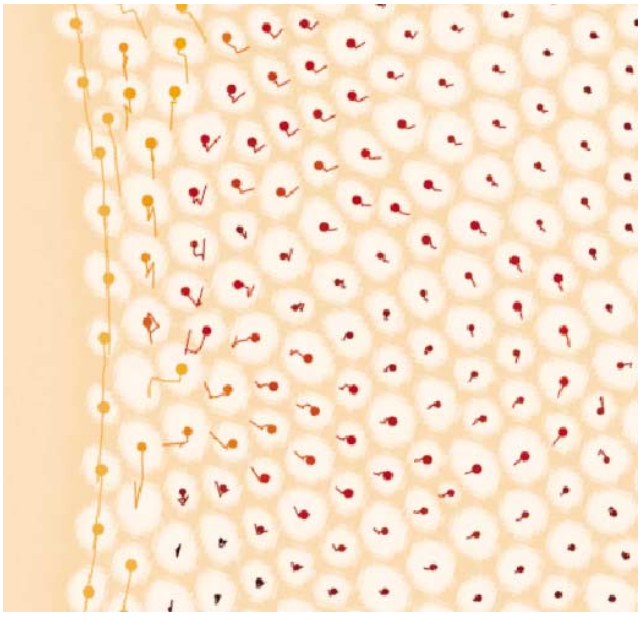

FIG. 3 (color). Video frame of the foam with the position of the bubbles centers and their trajectories over the last 20 sec. This time period corresponds to a total displacement of one bubble diameter for the first row (or equivalently for the inner disc edge). The dots size and lines color reflect the total distance traveled by the bubbles revealing a large rotating cluster.

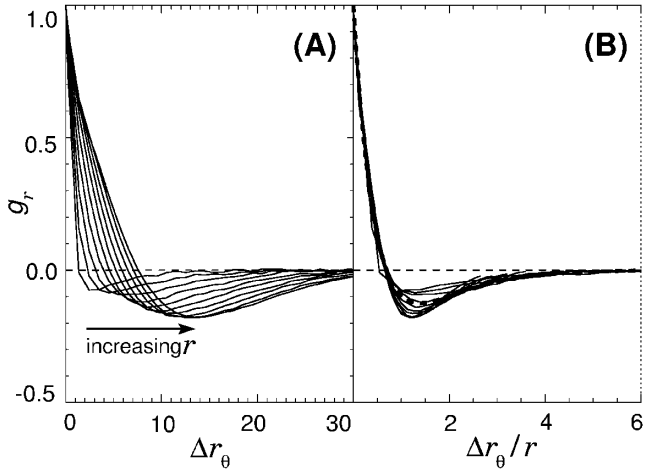

FIG. 4. (A): Spatial correlations of the radial velocity for different radial distances r from 1 to 10 ($\phi = 0.15$). (B): All correlations can be collapsed on a single curve when plotted versus the tangential distance rescaled by r. To fit this master curve, we assume that the radial velocity $v_r(r, r_\theta)$ at different r comes from the rotation of clusters of mean lateral extension $\xi(r)$ proportional to r [$\xi(r) = \alpha r$]. The radial velocity field within a cluster of size μ is idealized by a two step function ($v_r = \epsilon v_0$ for $-\mu < r_\theta < 0$ and $v_r = -\epsilon v_0$ for $0 < r_\theta < \mu$ with $\epsilon = \pm 1$). We postulate a statistical distribution of μ around $\xi(r)$ by assuming that the fraction of clusters of size larger than μ is $\exp(-\frac{\mu}{\xi(r)})$. The resulting correlation function (dotted line) then reads $g_r(\Delta r_\theta) = (1 - \frac{\Delta r_\theta}{\alpha r}) \exp(-\frac{\Delta r_\theta}{\alpha r})$.

for which g_r reaches 0 defines a typical correlation length of the velocity field at distance r. In Fig. 4(B), r_θ has been rescaled by r. All curves then collapse on a single one, which demonstrates a linear increase of $\xi(r)$ with the radial distance r: $\xi(r) = \alpha r$. Motivated by the observation of oscillating clusters, we modeled the flow field as a superimposition of rotating blocks of bubbles of various sizes (see figure caption for details) which allowed us to obtain a good fit of the master curve [Fig. 4(B)]. Similar results were obtained at all volume fractions, and the coefficient α was found to decrease with ϕ.

It should be noted that the velocity field which yields the measured correlation functions mainly corresponds to reversible moves and thus probes the elastic deformation of the foam rather than the plastic flow. The quantity $\sqrt{\langle v_r^2 \rangle}/\langle v_\theta \rangle$ provides a good estimate of the ratio of reversible to irreversible moves. This quantity is larger than 1 beyond the first attached row of bubbles, and gets larger than 10 beyond the fifth row. The correlation measurements thus reveal that the instantaneous *stress* field is spatially correlated.

This peculiar characteristic of the foam deformation field can actually be understood under the scope of linear elasticity, by modeling the foam as an isotropic elastic medium. In the following, we neglect the radial geometry of the experiment (the wheel radius being much larger than the shear band width) and thus assume parallel shear. During the initial loading, a uniform mean shear stress $\overline{\sigma}$ builds up in the material. In the steady state, this uniform stress persists in average but is locally modulated by a fluctuating stress field $\Delta\sigma(t)$ of mean value 0 associated with the continuous rubbing of the wheel teeth. At each location $(r = 0, r_\theta = i)$ on the wheel edge, the foam is indeed submitted to a localized perturbative stress $\Delta\sigma_i(t)$ of variance $s_0 = \langle \Delta\sigma_0^2 \rangle$ varying at a frequency ω_0 which elastically propagates into the material. These multiple noise sources add up to produce a stress fluctuation at a position (r, r_θ) of amplitude (see, for instance, [15]):

$$\Delta\sigma_r(r_\theta, t) \simeq \sum_i \frac{\Delta\sigma_i(t)}{\sqrt{r^2 + (r_\theta - i)^2}} . \qquad (2)$$

Assuming the noise sources to be uncorrelated [$\langle \Delta\sigma_i(t) \times \Delta\sigma_j(t) \rangle = 0$ for $i \neq j$], the resulting stress coherence length, at distance r, takes the form $\xi(r) = \alpha r$, in agreement with our experimental findings. We interpret the different observed values for α as a signature of the anisotropy of the foam due to its initial loading. This is consistent with the observation of large values of α for the driest foams where the largest uniform deformation is first produced. From Eq. (2), we are also able to compute the variance of the fluctuating stress $\Delta\sigma_r(t)$ as

$$\langle \Delta\sigma_r^2 \rangle = s(r) \sim \frac{s_0}{\alpha r} . \qquad (3)$$

We now relate the fluctuating stress field $\Delta\sigma_r(t)$ to the average flow profile by taking into account the foam plasticity. Our approach mostly follows a model proposed by Pouliquen and Gutfraind [4] based on Eyring's activated

process theory [16] to describe chute flows of granular materials. In the present description, the variance of the local stress fluctuation $s(r)$ plays the role of a temperature allowing plastic flow to occur. The moving boundary acts as a "hot wall," exciting internal deformation modes in the form of self-similar rotating clusters. When the fluctuating stress overcomes a certain yield value σ_y, the structure plastically yields. The yielding rate in the material by unit of time and space thus writes $\omega = \omega_0 P(\sigma > \sigma_y)$, where $P(\sigma)$ is the density probability of stress. The stress at a distance r is a sum of $\sim r$ random variables [see Eq. (2)] so that $P[\sigma(r)]$ is a Gaussian distribution centered on $\overline{\sigma}$ of variance $s(r)$. Using Eq. (3), the yielding rate at a distance r reads

$$\omega(r) = \omega_0 P[\sigma(r) > \sigma_y] = \omega_0 \left(1 - \mathrm{erf}\sqrt{\frac{r}{\lambda}}\right), \quad (4)$$

with

$$\lambda = \frac{1}{\alpha} \frac{2s_0}{(\sigma_y - \overline{\sigma})^2}. \quad (5)$$

Each failure increments the average velocity gradient by 1 in reduced unit, so that the constitutive equation for the flow writes $\frac{\partial \langle v_\theta(r) \rangle}{\partial r} \sim -\omega(r)/\omega_0$ with the boundary conditions $\langle v_\theta(0) \rangle = 1$ and $\langle v_\theta(\infty) \rangle = 0$. A very good approximate function to the integral of $\omega(r)$ is given by a pure exponential so that $\langle v_\theta(r) \rangle \simeq \exp(-r/\lambda)$ in good agreement with our experimental findings.

In conclusion, we have observed shear banding in dry and wet 2D foams under continuous slow shear and we have probed the associated elastic deformations of the foam, characterized by brief, collective oscillations of self-similar blocks of bubbles. We have developed a stochastic model which relates the plastic flow to the stress fluctuations. The main characteristics of the flow (rapid decay of the average velocity over a few bubbles, large velocity fluctuations) are very similar to what is commonly observed in granular systems, suggesting that the proposed mechanism could remain valid for granular systems. As already mentioned, the predicted exponential velocity decay has been observed in various 2D granular shear bands [4,5,7]. Moreover, the velocity profile in 3D has been shown to obey a Gaussian decay in the limit of disordered and nonspherical grains [6]. This functional form for the velocity profile immediately follows from the modification of Eq. (3) in 3D which then writes $s(r) \sim \frac{s_0}{\alpha^2 r^2}$ yielding a Gaussian decay for $\langle v_\theta \rangle$.

We are grateful to D. Mueth for helping us with the image analysis. We wish to thank A. Kabla, S. Roux, and C. Josserand for stimulating discussions.

*Corresponding author.
Electronic address: debregea@ics.u-strasbg.fr.
†Also at Université Louis Pasteur and Institut Universitaire de France.

[1] P. Sollich, F. Lequeux, P. Hebraud, and M. E. Cates, Phys. Rev. Lett. **78**, 2020 (1997).
[2] S. A. Langer and A. J. Liu, Europhys. Lett. **49**, 68 (2000).
[3] A. Liu and S. Nagel, Nature (London) **396**, 21 (1998).
[4] O. Pouliquien and R. Gutfraind, Phys. Rev. E **53**, 552 (1996).
[5] D. Howell, R. P. Behringer, and C. Veje, Phys. Rev. Lett. **82**, 5241 (1999).
[6] D. Mueth, G. Debrégeas, G. Karczmar, P. J. Eng, S. Nagel, and H. Jaeger, Nature (London) **406**, 385 (2000).
[7] T. S. Komatsu, S. Inagaki, N. Nakagawa, and S. Nasuno, Phys. Rev. Lett. **86**, 1757 (2001).
[8] J. B. Knight, E. E. Ehrichs, V. Y. Kuperman, J. K. Flint, H. M. Jaeger, and S. R. Nagel, Phys. Rev. E **54**, 5726 (1996).
[9] P.-G. de Gennes, Rev. Mod. Phys. **71**, S374 (1999).
[10] J. Torok, S. Krishnamarthy, J. Kertesz, and S. Roux, Phys. Rev. Lett. **84**, 3851 (2000).
[11] G. Debrégeas and C. Josserand, Europhys. Lett. **52**, 137 (2000).
[12] D. J. Durian, Phys. Rev. Lett. **75**, 4780 (1995).
[13] D. Weaire and S. Hutzler, *The Physics of Foams* (Clarendon Press, Oxford, 1999).
[14] W. Losert, L. Bocquet, T. C. Lubensky, and J. P. Gollub, Phys. Rev. Lett. **85**, 1428 (2000).
[15] K. L. Johnson, *Contact Mechanics* (Cambridge University Press, Cambridge, United Kingdom, 1985).
[16] K. Glasstone, J. Laider, and H. Eyring, *The Theory of Rate Processes* (McGraw-Hill, New York, 1941).

Local Stress Relaxation and Shear Banding in a Dry Foam under Shear

Alexandre Kabla and Georges Debrégeas*
LFO–Collège de France, CNRS UMR 7125, Paris, France
(Received 27 November 2002; published 27 June 2003)

We have developed a realistic simulation of 2D dry foams under quasistatic shear. After a short transient, a shear-banding instability is observed. These results are compared with measurements obtained on real 2D (confined) foams. The numerical model allows us to exhibit the mechanical response of the material to a single plastication event. From the analysis of this elastic propagator, we propose a scenario for the onset and stability of the flow localization process in foams, which should remain valid for most athermal amorphous systems under creep flow.

DOI: 10.1103/PhysRevLett.90.258303 PACS numbers: 82.70.Rr, 05.40.–a, 83.50.–v, 83.60.–a

Amorphous glassy materials are ubiquitous in industry and nature: they include silica-based glass-formers and polymer melts below T_g, dense colloidal suspensions and emulsions, foams, and dense granular systems. Unlike crystalline solids, plasticity in such systems originates from discrete *local* relaxation events [1,2], involving a small number of particles (atoms, grains, bubbles, etc.). Spatial and time correlations in the occurrence of these plastic events are generally important, leading to avalanchelike dynamics [3–5] and spatially inhomogeneous flows [6–8]. Glassy rheology thus remains one of the most active and challenging domains of statistical physics.

Among the large number of theoretical and numerical models recently proposed, foam has emerged as a strongly inspiring model system [9–11]. First, because thermal energy is strictly irrelevant on bubble scale, creep flow experiments can be run (by imposing an infinitely low deformation rate) in which time dependent effects are absent. Second, the bubble mechanics is simple and yields a wide linear elastic regime. Finally, plasticity in foams is associated with well-identified processes. In spite of this apparent simplicity, many features of foams flow remain to date unexplained [12]. Thus, shear-banding flows have been recently exhibited in a 2D Couette experiment [13]. In this study, a monolayer of bubbles squeezed between two glass plates was slowly sheared between two concentric discs. Much of the rearrangements were found to occur in a thin region (a few bubbles in width) along the edge of the inner disc. In the present Letter, we directly address this question by developing a numerical model adapted to the quasistatic shearing of 2D dry foams. The observed flow features are compared with experimental data obtained with the same setup as in [13]. This model allows us to investigate the microscale mechanics of the foam leading to strain localization.

We use Voronoi tessallation to build polydisperse structures of $W \times L = 16 \times 48$ cells separated by straight segments. These are later referred to as bubbles and films, respectively, by analogy with real foams, the intercept between films being called a vertex. These structures have periodic boundary conditions along the x direction, and films laying at the upper and lower edges are fixed to allow subsequent plane parallel shearing [Fig. 1(a)]. To obtain a mechanically equilibrated structure, the total film length is minimized at fixed topology and with a constant volume constraint on each bubble, as expected for static dry foams [14]. Our algorithm is based on Surface Evolver [15], a software widely used in foams structural studies [16]. The main difficulty of this minimization procedure comes from the existence of very soft modes associated with large-scale shear deformations [17]. A special care is thus put in equilibrating these modes. The overall procedure is then validated by imposing various strain fields to the initial foam, and checking that the resulting equilibrated structure remains unchanged.

Once the foam has been mechanically equilibrated, plasticity is introduced by allowing $T1$ rearrangements—the elementary topological changes in 2D foams [see Fig. 1(b)]. In a real dry foam, vertices have a finite size which depends on the liquid fraction. When a film becomes smaller than this length, the two vertices attract and a $T1$ event is triggered. We mimic this criterion by exchanging bubbles neighbors when one of the film length

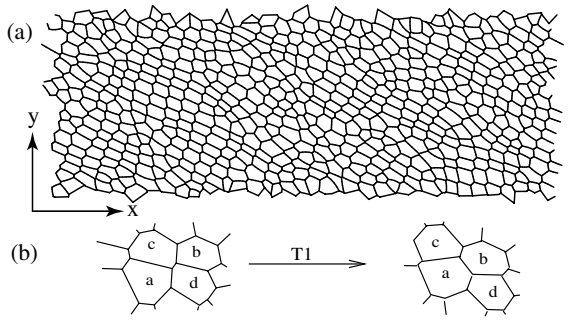

FIG. 1. (a) Snapshot of a simulated foam with 16×48 bubbles. The polydispersity is 6%. The foam has periodic boundary conditions along the x direction. Films laying at upper and lower edges are fixed; shearing is obtained by moving the lower edge along the x direction. (b) Example of a topological change ($T1$ process) occurring inside the foam upon shearing.

 © 2003 The American Physical Society

falls below a fixed value l_v, corresponding to a liquid fraction $\phi = 1\%$. The $T1$ events are triggered one at a time and followed by a complete mechanical equilibration. This two-step procedure is iterated until all films are stable with regards to the $T1$ criterion. It should be noted that this procedure might not precisely reflect the physical process taking place during an avalanche of $T1$ events. Indeed, in a real foam plasticity and mechanical equilibration take place simultaneously. Our procedure implicitly assumes the latter to be much faster than the $T1$ event. Finally, the foam is quasistatically sheared by iteratively moving the lower edge over a short distance then equilibrating the structure and allowing plastic events.

Figure 2 conveys the main result of the present study: it displays the y_{T1} positions of the rearrangements as a function of the imposed wall displacement D. After a short transient (for $D \sim W$ i.e., an imposed strain ~ 1), the rearrangements permanently gather within a thin shear band in the vicinity of the lower wall. This strain instability is observed for all the simulations, with a flow localization taking place on either wall depending on the initial foam structure. In the following we mainly focus on measurements performed in the steady-state localized regime.

From the sequence of equilibrated structures, we measure the trajectories of the bubbles centers to extract the flow field at each time step. Furthermore, we can compute the internal shear stress on any subvolume w using the following relation (where the summation is performed over all segments $\vec{l}$ inside w) [12]:

$$\sigma_{xy}(w) = \frac{1}{w} \sum_{l \in w} \frac{l_x l_y}{l}. \quad (1)$$

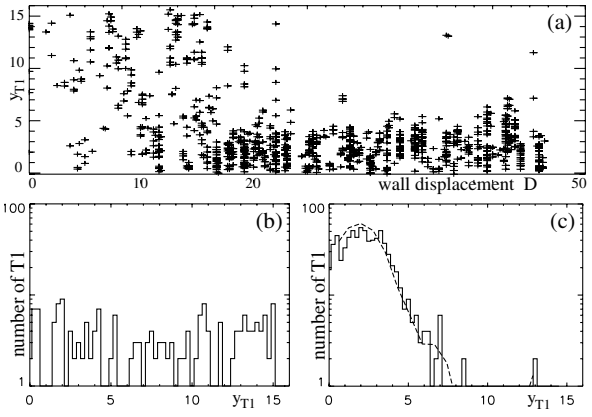

FIG. 2. Localization process in a simulated foam. (a) The y position of the $T1$ events as a function of the wall displacement D expressed in bubble diameter. (b) Distribution of the y positions of the $T1$ events for $D < 15$ (transient regime) and (c) $D > 20$ (localized regime). In the latter, the dotted line shows the gradient $\frac{\partial \overline{v}}{\partial y}(y)$ of the associated plastic flow profile $\overline{v}(y)$.

We have compared time averaged measurements from the simulation with experimental data we obtained using the same liquid fraction ($\phi = 1\%$). Figure 3 shows the tangential velocity profiles and the normal velocity fluctuations for the experiment and the simulation. For both quantities, we observe similar decays with the distance from the wall. Other flow features, such as the stress fluctuations profiles (presented below), show a similarly good agreement. This adequacy proves the validity of the present simulation. Conversely, it demonstrates that the shear banding observed in [13] is not due to the Couette geometry, in which the mean stress decreases with the distance from the inner disc.

Beyond these time averaged measurements, the simulation allows one to study the evolution of the foam on short time scales. The dynamics can be separated into two elementary processes, associated with different simulation time steps: (i) charge periods over which the position of the wall is incremented without plastication. The resulting deformation is linear and the shear stress tensor uniformly increases. This allows us to extract a shear elastic modulus μ. This modulus is found to weakly depend on the total applied strain and is considered as a constant in the following. (ii) plastic yielding, during which the stress is relaxed through discrete $T1$ events. To analyze in detail the latter, we focus on the displacement and shear stress fluctuation fields produced by a single rearrangement. The spatial resolution is enhanced to below one bubble diameter by averaging these results over 100 individual $T1$ events located at the same y_{T1} coordinate.

Figures 4(a) and 4(b) display the average displacement profiles associated with $T1$ events located at two different distances y_{T1} from the lower wall. Both profiles exhibit a strong discontinuity at the rearranging line, whereas the rest of the material is uniformly deformed with a strain amplitude $\delta\epsilon_{T1}$. Regardless of the position y_{T1}, $\delta\epsilon_{T1} = 1.07\, d^2/(WL)$ (with a 30% statistical dispersion over

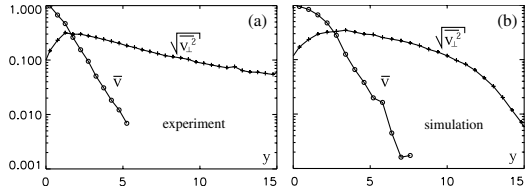

FIG. 3. Comparison of time averaged measurements obtained from (a) experiments on 2D foams in a Couette cell and (b) simulated foams. $\overline{v}$ is the tangential velocity rescaled by the wall velocity v_0. $\sqrt{\overline{v}_\perp^2}$ is the normal mean square displacement, associated with a time lapse $\tau = 0.25\, d/v_0$, where d is the average bubble diameter. The rapid drop of $\sqrt{\overline{v}_\perp^2}$ in (b) far from the moving wall is due to the relatively small width of the simulated foam ($W = 16$), and hence the presence of the other confining wall.

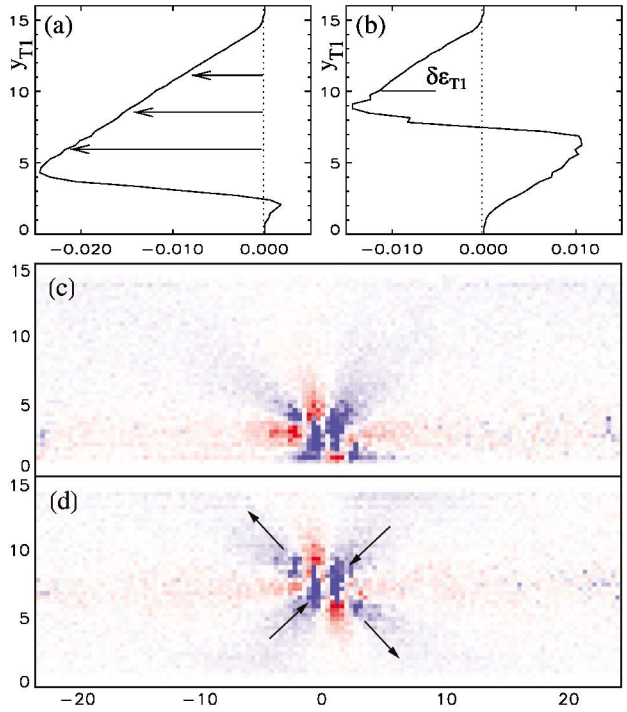

FIG. 4 (color). Displacement and variational shear stress field associated with a single $T1$ event. Each of these results has been obtained by averaging over ~100 different $T1$ events located at the same distance y_{T1} from the shearing wall. (a) and (b): line averaged displacement profiles (expressed in bubble diameter d), for a $T1$ event located at $y_{T1} = 3$ and 8, respectively. $\delta\epsilon_{T1}$ represents the mean strain released by the $T1$ event. (c) and (d): Corresponding shear stress variation fields. Red color indicates an increase of the stress (relative to the imposed shear stress), blue color indicates a stress relaxation. The arrows show approximately the motion of the rearranging bubbles during the $T1$ event.

different $T1$ events), where d is the mean bubble diameter and WL is the foam area.

This elementary strain $\delta\epsilon_{T_1}$ can be interpreted from two different viewpoints. On one hand, it represents a *plastic* strain amplitude: each $T1$ event increments the plastic flow gradient at $y = y_{T1}$ by $-\delta\epsilon_{T1}$ in average. This yields the following kinematic relation between the plastic flow profile $\overline{v}(y)$ and the spatial distribution of $T1$ events:

$$\frac{\partial \overline{v}}{\partial y}(y) = -W\ \omega(y)\ \delta\epsilon_{T_1}, \tag{2}$$

where $\omega(y)dy$ is the frequency of $T1$ events occurring between y and $y + dy$. This relation can be directly exhibited by overplotting the plastic velocity gradient on the $T1$ spatial distributions [see Fig. 2(c)]. On the other hand, $\delta\epsilon_{T_1}$ is a uniform elastic strain relaxation. The associated stress can be independently evaluated using Eq. (3) yielding a line-averaged uniform stress release $\delta\sigma_{T1} = \mu\delta\epsilon_{T1}$. By taking into account both the elastic charge and $T1$ relaxation, we derive an equation of evolution of the line-averaged shear stress $\overline{\sigma}(y)$, valid for any line y between 0 and W:

$$\mu\dot{\gamma} - \mu\delta\epsilon_{T1}\int_0^W \omega(y')dy' = \frac{\partial\overline{\sigma}(y)}{\partial t} = 0. \tag{3}$$

The first term of the left-hand side of the equation corresponds to the advective charge induced by the imposed shear at strain rate $\dot{\gamma}$. The second term comes from the cumulative relaxation of stress associated with the $T1$ processes. The integral form of this equation is a direct consequence of the long range mechanical relaxation associated with each $T1$ process. As a result, this line-averaged mechanical analysis cannot allow one to predict a flow profile, and is in fact strictly equivalent to Eq. (2) from which it can be deduced by simple integration. In other words, any velocity profile which obeys the kinematic boundary conditions is mechanically admissible.

The understanding of the shear-banding instability finally comes down to the following question: All lines bearing in average the same stress, why are $T1$ events unevenly distributed among them? To capture this process, we need to go beyond the line-averaged analysis and examine the spatial structure of stress release associated with individual T1 events. This is shown in Figs. 4(c) and 4(d) for two different y_{T1} locations. As it appears clearly, the stress release is very inhomogeneous and anisotropic, owing to the systematic displacement pattern of the rearranging bubbles imposed by the shearing [8,18]. In particular, lines in the vicinity of the rearranging site experience large stress modifications. Although the global effect is a release of the main shear stress, some region-s(which appear in red) get overcharged. By contrast, remote lines are homogeneously relaxed.

From this measurement, one may expect that T1 events do not only relax the global stress but also cumulatively modify the statistical properties of the frozen stress field. To investigate this effect, we measure the shear stress distributions $P[\sigma(x, y)]$ at different distances y from the shearing wall. We extract from these distributions the local variances $\Delta\sigma^2(y) = \langle[\sigma(x, y) - \overline{\sigma}]^2\rangle$. We then compare these profiles obtained from foam structures before shearing and after full localization. As shown in Fig. 5, the shearing induces an inhomogeneous modification of these profiles: a large increase of $\Delta\sigma^2$ occurs in the shear-band region where many T1 events have occurred, in both the experiment and the simulation. By contrast, the stress distributions in lines away from the shear-band display no modification, or even a small decrease of their variance. The latter is due to T1's occurring during the transient period of charge which do not have a systematic orientation. We therefore postpone the discussion of this effect.

This result shows that the strain history of the foam is permanently imprinted in its frozen stress field, and that such modification can be directly probed through

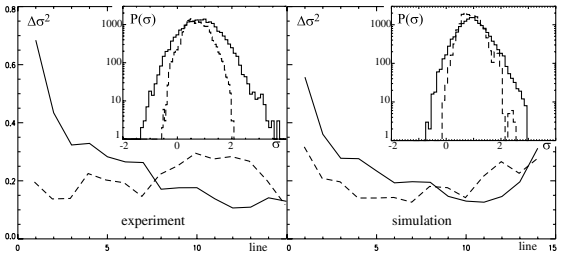

FIG. 5. Profile of shear stress variance $\langle[\sigma(x, y) - \overline{\sigma}]^2\rangle$ in real (left) and simulated (right) foams. Solid lines correspond to foams in the fully localized regime. Dashed lines correspond to freshly prepared samples (no shearing). All data have been rescaled with the long time limit shear stress. Inset: shear stress probability distributions at lines $y = 1$ (solid) and $y = 10$ (dashed), respectively, in the localized regime.

measurements of $\Delta\sigma^2$. This parameter has a further important physical meaning: large values of $\Delta\sigma^2$ indicate that a large fraction of bubbles are highly deformed and therefore more likely to rearrange upon increasing the global stress. This parameter thus provides a local measurement of the foam "fragility."

Based on these observations, a simple scenario for strain localization in quasistatic shearing can be proposed. Starting with a homogeneous structure, shear banding develops through a self-amplification process: $T1$ events locally weaken the foam structure by increasing its frozen stress disorder. This in turn enhances the probability for subsequent rearrangements to take place in neighboring lines. This mechanism spontaneously leads to the formation of a single shear band in the material. Within this scheme, we can also qualitatively understand why shear bands preferentially develop along the boundaries, even in plane parallel shearing geometry where the average shear stress is uniform. Indeed, the presence of a rigid boundary with a no-slip condition imposes an extra mechanical constraint to the foam in the vicinity of the walls. This tends to locally enlarge the local stress distributions.

The experimental and numerical systems studied here provide an ideal model to study plasticity in disordered media. It allowed us to access detailed mechanical features, from the stress signature associated with a single plastic event, to the statistical modifications of the frozen stress field associated with a fully developed shear flow. We have used these results to propose a simple scenario for shear localization based on a strain weakening process. Most results obtained with this model system should remain valid to any material provided the existence of (i) frozen disorder (no thermal relaxation), (ii) elastic behavior at low deformation, (iii) local discrete plastication processes. It could therefore serve as a useful test to more elaborated models of plasticity that involve local stress relaxations [1,8,19] but do not necessarily address foam rheology.

We wish to thank J. Scheibert, C. Caroli, O. Pouliquen, and J.-M. di Meglio for stimulating discussions. We are grateful to C. Fond for introducing us to finite elements calculation.

*Electronic address: georges.debregeas@college-de-france.fr

[1] V.V. Bulatov and A. S. Argon, Modell. Simul. Mater. Sci. Eng. **2**, 167 (1994).
[2] M. L. Falk and J. S. Langer, Phys. Rev. E **57**, 7192 (1998).
[3] Kan Chen, Per Bak, and S. P. Obukhov, Phys. Rev. A **43**, 625–630 (1991).
[4] Y. Jiang, P. J. Swart, A. Saxena, M. Asipauskas, and J. A. Glazier, Phys. Rev. E **59**, 5819 (1999).
[5] S. Tewari, D. Schiemann, D. J. Durian, C. M. Knobler, S. A. Langer, and A. J. Liu, Phys. Rev. E **60**, 4385 (1999).
[6] P. Hébraud, F. Lequeux, J. P. Munch, and D. J. Pine, Phys. Rev. Lett. **78**, 4657 (1997).
[7] D. Mueth, G. Debrégeas, G. Karczmar, P. J. Eng, S. Nagel, and H. Jaeger, Nature (London) **406**, 385 (2001).
[8] J. S. Langer, Phys. Rev. E **64**, 11 504 (2001).
[9] P. Sollich, F. Lequeux, P. Hébraud, and M. E. Cates, Phys. Rev. Lett. **78**, 2020 (1997).
[10] D. J. Durian, Phys. Rev. E **55**, 1739 (1997).
[11] I. K. Ono, C. S. O'Hern, D. J. Durian, S. A. Langer, A. J. Liu, and S. R. Nagel, Phys. Rev. Lett. **89**, 095703 (2002).
[12] D. Weaire and S. Hutzler, *The Physics of Foams* (Clarendon Press, Oxford, 1999).
[13] G. Debrégeas, H. Tabuteau, and J. M. di Meglio, Phys. Rev. Lett. **87**, 178305 (2001).
[14] D. Weaire and J. P. Kermode, Philos. Mag. B **50**, 379 (1983).
[15] K. Brakke, Exp. Math. **1**, 141–165 (1992).
[16] D. A. Reinelt and A. M. Kraynik, J. Rheol. **44**, 453 (2000).
[17] T. Herdtle and H. Aref, J. Fluid Mech. **241**, 233 (1992).
[18] We were actually able to reproduce this propagator using a finite element algorithm (CASTEM2000), by imposing a quadrupolar displacement in a 2D incompressible elastic medium, with identical boundary conditions. This indicates that beyond the rearranging bubbles, the foam responds as an elastic body to the plastication event.
[19] C. Derec, A. Ajdari, and F. Lequeux, Eur. Phys. J. **4**, 355–361 (2001).

THEME 2 : MICRO-PLASTICITE DANS LES MILIEUX GRANULAIRES

Résumé : nous avons étudié, par diffusion multiple de la lumière, la dynamique de réorganisation du réseau de contact au sein d'empilements granulaires soumis à de très faibles vibrations. Nous avons mis en évidence un processus de renforcement progressif de ce réseau qui se traduit par un temps de relaxation intrinsèque croissant avec le nombre de pulses de vibrations appliqués.

Nous avons par ailleurs mesuré, par tomographie X, l'énergie de précurseurs d'avalanche dans un empilement granulaire en tambour tournant à l'approche de l'angle d'avalanche macroscopique. Nous avons caractérisé la façon dont cette séquence d'événements dépend de « l'histoire » de l'échantillon, c'est-à-dire de la trajectoire angulaire du tambour.

Un empilement granulaire est un matériau intrinsèquement fragile. Sa tenue mécanique repose sur l'existence d'un réseau de forces de contact entre les grains qui, même pour un empilement régulier, présente un fort désordre. C'est pourquoi toute déformation même minime de l'empilement peut conduire à la rupture de l'un de ces contacts et à une réorganisation irréversible de ce réseau de forces. Pour autant, cette micro-plasticité n'implique pas nécessairement de modification de la structure de l'empilement, du fait du découplage d'échelle entre les grains et les contacts.

Il existe donc deux échelles de description pour un milieu granulaire. L'une concerne la structure de l'empilement dont la dynamique peut être sondée par exemple dans les études dites de compaction (où le matériau est soumis à de fortes vibrations) ou d'écoulement forcé. Dans cette partie, je décris des expériences qui visent au contraire à étudier la dynamique de la structure à l'échelle des contacts. Nous étudions l'évolution du réseau de forces induite par de très faibles vibrations ou par une très lente rotation d'ensemble de l'échantillon. Ces perturbations mécaniques ne modifient que très peu l'empilement granulaire mais engendrent un changement important dans la réponse micro-plastique du milieu du fait d'une modification de la structure du réseau de forces.

A) DYNAMIQUE D'UN RESEAU DE CONTACTS SOUS FAIBLES VIBRATIONS.

Le premier système étudié consiste en un empilement tri-dimensionnel de billes de verre de diamètre 50 microns immergées dans l'eau. La cellule contenant l'empilement est fixée sur un actuateur piezo-électrique permettant d'imposer de brefs pulses de vibrations verticales appelés « tapes », sous la forme de trains d'onde d'une durée 100ms à une fréquence de 1kHz. Pour mesurer les mouvements microscopiques induits par ces vibrations dans l'échantillon, nous utilisons une méthode de diffusion multiple de la lumière multi-speckle (MSDWS). Nous formons sur une caméra CCD l'image de la figure de diffraction d'un faisceau laser après traversée de l'échantillon. Une image est prise entre chaque tape, lorsque tout mouvement s'est interrompu. Une analyse des corrélations d'intensité à 2 temps de la séquence d'images permet de déterminer la fréquence des micro-glissements induits par les tapes dans l'échantillon[1].

Nous utilisons deux amplitudes de vibrations (tapes « faibles » et « fortes ») de quelques dizaines et quelques centaines de nanomètre d'amplitude, respectivement. Les tapes fortes permettent d'amener le système à une densité granulaire donnée par un processus de compaction standard. Nous appliquons ensuite une longue série de tapes faibles qui ne modifient pas (ou très peu) la fraction volumique moyenne. Cette deuxième étape permet de sonder la réponse micro-plastique du matériau à l'échelle des contacts. Nous avons observé que cette réponse ne dépend que du nombre de tapes faibles – noté t_w - fournies depuis la dernière tape forte. Pour chaque valeur de t_w, nous mesurons un temps $\tau(t_w)$ proportionnel à l'inverse du nombre de micro-glissements produits par chaque tape. Ce temps représente donc un temps caractéristique de réorganisation du réseau de contacts (exprimé en nombre de tapes) associé à cette sollicitation de faible intensité. Nous avons montré que le temps $\tau(t_w)$

augmente de façon quasi-linéaire avec t_w. Cette évolution, établie sur 5 ordres de grandeur, dépend peu de la fraction volumique initiale du tas (Figure 4). En outre, la dynamique peut être entièrement réinitialisée par l'application de quelques tapes de forte intensité.

Ce ralentissement dynamique est très similaire à celui observé dans le domaine des verres colloïdaux : dans ces matériaux, le temps de relaxation le plus long (temps α) croît en loi de puissance du temps depuis que le système a été laissé au repos et la dynamique peut être relancée par l'application d'un fort cisaillement[2]. Cette analogie est surprenante lorsque l'on considère les processus physiques en jeu dans ces deux types de systèmes : dans les liquides colloïdaux, le phénomène de vieillissement est lié à une relaxation des contraintes piégées par activation thermique[3]. Ici, ce sont les ondes acoustiques produites par les vibrations qui, en déclenchant la rupture de certains contacts, contrôlent la dynamique de renouvellement du champ des contraintes internes.

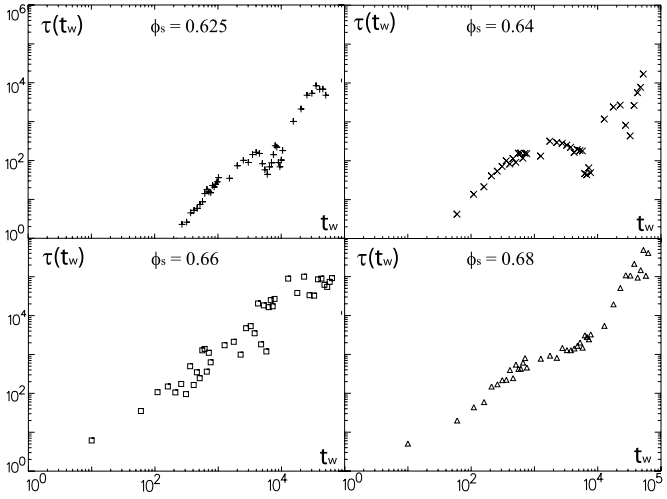

Figure 4 : Evolution du temps de relaxation $\tau(t_w)$ exprimé en nombre de tapes et caractérisant la dynamique du réseau de contacts, en fonction du nombre de tapes faibles t_w depuis le début de l'expérience. Les 4 graphes correspondent à différentes fractions volumiques ϕ_s de l'empilement granulaire.

Cette analogie nous a conduits à proposer un modèle simple permettant de comprendre les principaux résultats observés. Notre approche est largement inspirée du modèle de pièges développé par Bouchaud pour décrire le vieillissement des liquides vitreux. Nous décrivons le système dynamique comme un ensemble de contacts indépendants en nombre fixé ; nous considérons donc la structure de l'empilement à l'échelle des grains comme invariante. Chaque contact est caractérisé par une force dont les composantes obéissent à un critère d'équilibre de Coulomb. Lors d'une tape, chaque contact subit une fluctuation aléatoire de force pouvant occasionner une rupture. Cette description permet d'écrire une équation simple d'évolution de la distribution des forces au niveau des contacts, associée à une évolution de la fréquence totale de micro-glissements en accord qualitatif avec les observations expérimentales. Dans cette description, le phénomène de ralentissement dynamique est le résultat d'une déplétion progressive des contacts faibles, conduisant à une consolidation effective du tas.

B) PRECURSEURS D'AVALANCHE

Cette seconde expérience, réalisée lors d'un séjour à l'Université de Canberra en 2002, vise à établir un lien entre les deux échelles de description des milieux granulaires : l'empilement et le réseau de forces. L'idée sous-jacente est que les transitions solide/fluide dans les milieux granulaires (avalanche granulaire, apparition d'une bande de cisaillement sous contrainte uni-axiale, déblocage d'une trémie...) résulteraient d'une rupture collective d'un grand nombre de contacts. Nous cherchons

à identifier, dans la réponse plastique microscopique du tas, une signature de l'approche vers cette rupture macroscopique de l'empilement.

Figure 5 : (A) *Image radiographique du tambour tournant.* (B) *Image traduisant les variations relatives de longueur d'absorption X en tout point de l'échantillon induit par un incrément de 0 .5° de l'angle de rotation du tambour. De cette image, il est possible d'extraire l'énergie dissipée par les mouvements de grains au sein de l'échantillon lors de cet incrément.*

Nous avons construit pour cela une expérience de type tambour tournant constituée d'un empilement de grains confiné entre 2 disques de verres pouvant être mis en rotation de façon contrôlée[4]. Un faisceau X focalisé traverse l'échantillon et l'intensité transmise est mesurée sur une caméra CCD. Nous mesurons, en chaque point de l'échantillon, la variation d'intensité transmise associée à un incrément de rotation du tambour (Figure 5). Cette technique permet d'extraire les caractéristiques spatiales et l'énergie d'événements de micro-plasticité se produisant avant l'apparition d'une avalanche macroscopique.

Nous avons pu montrer que, à l'approche de l'angle d'avalanche, le nombre et l'énergie de ces précurseurs d'avalanche augmentaient rapidement. Nous avons montré que la séquence de ces événements dépendait de « l'histoire » de l'échantillon i.e. de la trajectoire angulaire suivie par le tambour. A l'inverse, l'angle d'avalanche macroscopique est indépendant de cette séquence, ce qui indique que les deux types de dynamiques – pré-avalanches et avalanches macroscopiques – sont de nature différente. Les pré-avalanches sont des instabilités mécaniques du réseau de forces et dépendent de l'état statistique des contraintes au sein de celui-ci. Les avalanches macroscopiques sont elles des instabilités dynamiques essentiellement contrôlées par les propriétés dissipatives du matériau.

Références :

1. Contact Dynamics in a Gently Vibrated Granular Pile. A. Kabla and G. Debrégeas, *Phys. Rev. Lett.* 92(3), 035501(2004)
2. Partial rejuvenation of a colloidal glass. F. Ozon, T. Narita, A. Knaebel, G. Debrégeas, P. Hébraud and J.-P. Munch, *Phys. Rev. E* 68, 032401 (2003)
3. Rheology of soft glassy materials. D. Bonn, P. Coussot, H. Huynh, F. Bertrand and G. Debrégeas, *Europhys. Lett.*, 59 (5), pp. 786-792 (2002)
4. X-ray observation of micro-failures in granular piles approaching an avalanche, A. Kabla, G. Debrégeas, J.-M. di Meglio and T. J. Senden, *Europhys. Lett.* 71 932-937 (2005)

Contact Dynamics in a Gently Vibrated Granular Pile

Alexandre Kabla and Georges Debrégeas*
LFO-Collège de France, CNRS UMR 7125, Paris, France
(Received 27 March 2003; published 22 January 2004)

We use multispeckle diffusive wave spectroscopy to probe the micron-scale dynamics of a water-saturated granular pile submitted to discrete gentle taps. The typical time scale between plastic events is found to increase dramatically with the number of applied taps. Furthermore, this microscopic dynamics weakly depends on the solid fraction of the sample. This process is largely analogous to the aging phenomenon observed in thermal glassy systems. We propose a heuristic model where this slowing-down mechanism is associated with a slow evolution of the distribution of the contact forces between particles. This model accounts for the main features of the observed dynamics.

DOI: 10.1103/PhysRevLett.92.035501 PACS numbers: 81.05.Rm, 05.45.–a, 45.70.Cc

Internal contact forces in dense granular systems are very inhomogeneous [1,2], even for crystalline assemblies [3]. The stress at a given contact can change macroscopically following a relative displacement of the two particles on the order of microns. Hence, large modifications in the contact forces field can result from minute deformations of the pile. This phenomenon is crucial in understanding the catastrophic yielding occurring in granular systems submitted to a slowly varying stress (avalanches [4], shear bands in triaxial tests [5]). It also explains why the sound transmission through a granular sample can be strongly affected by very small deformations [6]. To probe the evolution of the internal stress field, one needs to measure forces directly [7,8] which is difficult in 3D. In this Letter, we propose a different approach: we use multispeckle diffusive wave spectroscopy (MSDWS) to measure particle displacements on micron scales in a pile submitted to gentle discrete taps. These vibrations are too weak to induce large-scale rearrangements which would eventually lead to a compaction of the granular system [9–11]. We can therefore evaluate the microdynamics of the contacts without significantly perturbing the packing structure.

We use glass beads of diameter 45 ± 2 μm, contained in a glass cell (30 mm $\times$ 10 mm $\times$ 2 mm). To reduce electrostatic forces and avoid any capillary attraction due to moisture, the granular system is fully saturated with pure water. During the experiment, the mean packing fraction ϕ is obtained by measuring the position of the upper surface of the pile with a charge-coupled device (CCD) camera. Although a systematic error of 2% cannot be avoided, this allows us to detect relative changes in ϕ as small as 0.01%. To produce motion in the pile, we use a piezoelectric actuator on which the cell is rigidly mounted. Vertical vibrations of precisely controlled amplitude, shape, and durations can thus be applied to the granular column. In the present experiment we focus on a single type of mechanical excitation, later referred to as a "tap," which consists of a train of square wave vibrations of frequency 1 kHz and duration 100 ms. Different applied voltages are used, yielding various vertical amplitudes ranging from 50 to 300 nm.

In a standard experimental run, the pile is prepared by turning the cell upside down and then allowing the particles to sediment for half an hour. This procedure yields reproducible structures of low volume fraction. The pile is then submitted to high amplitude taps (of vertical amplitude 300 nm) until it reaches a prescribed packing fraction ϕ_s. This first step is a way to obtain granular samples of given packing fractions with essentially the same preparation history. We then start probing the dynamics of contacts by submitting the cell to very gentle taps of amplitude 50 nm (Fig. 1). During the compaction stage, the evolution of the packing fraction ϕ with the number of taps is consistent with previous experimental results on dry granular systems [9–11]. It should be noted however that the packing fraction we reach is well above the close

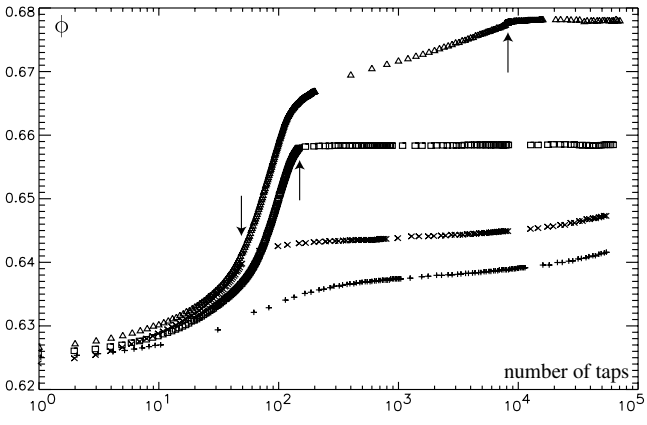

FIG. 1. Evolution of the packing fraction for four experimental runs. Each run consists of a first step in which high amplitude taps allow rapid compaction of the sample, followed by a sequence of gentle vibrations, during which the internal dynamics is probed. The arrows indicate the change in tapping intensity, which occurs after (+) 0, (×) 50, (□) 150, (△) 8000 high impulsion pulses. There is a systematic error of 2% on the measurements of the packing fraction.

 © 2004 The American Physical Society

packing limit expected for a fully disordered pile ($\simeq 0.64$). This indicates that crystallization does occur in our system under strong vibration. In contrast, the low intensity vibrations do not induce significant further evolution of the packing fraction except for initially very loose packs.

To probe the microscopic dynamics induced by these gentle taps, we use MSDWS [12,13]. This technique, which allows one to resolve submicron displacements, has been successfully applied to granular dynamics by several groups [14,15]. The sample is illuminated with a He-Ne laser beam at a depth of 2 cm below the upper surface of the pile (1 cm over the bottom). Photons are multiply scattered by the particles [16] and form a speckle pattern on the opposite cell wall which we record with a CCD camera. In the absence of vibration, the speckle image does not change in time as temperature is insignificant for such large objects. In contrast, the taps induce some irreversible particle displacements which modify the speckle image. To quantify the internal dynamics, we measure the intensity correlation of speckle images, taken between taps, as a function of the number of taps t that separate them. This function generally depends on the total number of small amplitude taps t_w that have been performed. We therefore calculate the two-times correlation function $g(t_w, t)$:

$$g(t_w, t) = \frac{\langle I(t_w + t)I(t_w)\rangle_{\mathrm{spkl}} - \langle I(t_w)\rangle^2_{\mathrm{spkl}}}{\langle I(t_w)^2\rangle_{\mathrm{spkl}} - \langle I(t_w)\rangle^2_{\mathrm{spkl}}}. \qquad (1)$$

In this expression, $\langle\,\rangle_{\mathrm{spkl}}$ denotes the average over different speckles. MSDWS thus allows one to rapidly access relaxation time by substituting time with space averaging and is therefore well suited to the study of nonstationary dynamical systems.

Figure 2 shows three correlation functions obtained with the same sandpile at different values of t_w. These functions are well fitted by stretched exponentials: $g(t_w, t) = \exp(-(t/\tau(t_w))^{\alpha(t_w)})$.

For different packing fractions, we follow the evolution of the dynamics by monitoring $\tau(t_w)$ and $\alpha(t_w)$ as a function of the total number of gentle pulses t_w. We find that the exponent α is roughly constant ($\simeq 0.8 \pm 0.2$) and independent of the packing fraction ϕ_s. In contrast, the time $\tau(t_w)$ increases by five decades over the range of t_w explored, as shown in Fig. 3. This result demonstrates that the response of a granular system to small perturbations is strongly dependent on the history of its preparation (the number of applied taps t_w) and rather insensitive to the packing fraction. Conversely, the dynamics can be entirely reset by submitting the system to a few taps of large intensity (such as those used for compacting the sample). A careful examination of the $\tau(t_w)$ curve also reveals large fluctuations in the internal dynamics, especially in looser packs in which the packing fraction slowly evolves. During certain periods of time, the dynamics is restarted as shown by a sudden decrease of $\tau(t_w)$. This may correspond to catastrophic failures of the pack structure, which compete against a global reinforcement of the granular contacts.

The dynamical arrest observed here is strongly reminiscent of the aging behavior recently exhibited in various glassy colloidal systems [18–20]. In these materials, the longest (α)-relaxation time is found to grow as a power law of the time since the system was left to rest after rapid shearing. Here, the large fluctuations of $\tau(t_w)$ do not allow one to definitely claim a power-law behavior, especially for low density samples, but the overall evolution of $\tau(t_w)$ is compatible with this standard result. This analogy is surprising considering the differences in the microscopic processes underlying the dynamics in both systems: in glassy liquids, stress relaxation occurs by thermally activated rearrangements of the structure. In granular materials, temperature is effectively zero and relaxation results from the local yielding of contacts triggered by externally applied vibrations.

We now turn to a tentative microscopic model to capture this slowing-down process. We first need to connect

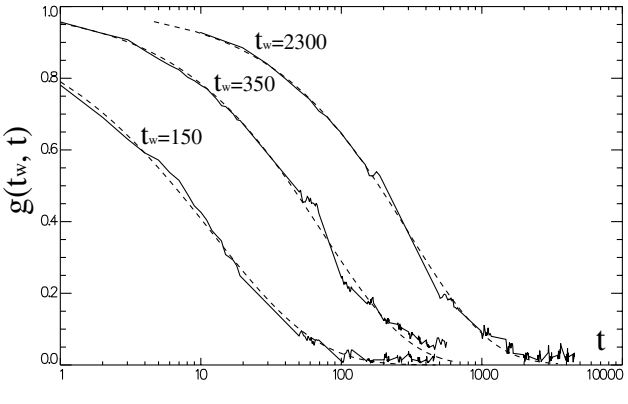

FIG. 2. Three different correlation functions obtained after three different times t_w. Solid lines correspond to experimental values and dashed lines to the stretched exponential fit.

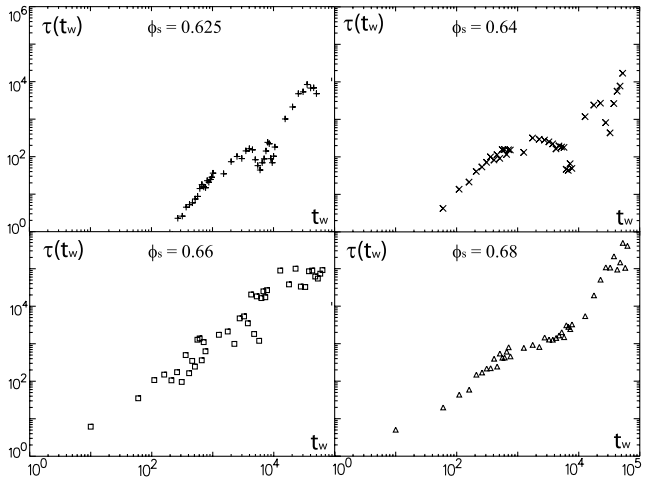

FIG. 3. Evolution of the dynamical time τ with the number of low magnitude taps t_w for different packing fractions ϕ_s.

DWS measurements to a grain-level description of the dynamics. We note that only the irreversible grain displacements produced by slippage events are responsible for the speckle image decorrelation. Since we do not observe significant compaction in the low vibration regime, the amplitude of these displacements ought to be much smaller than the diameter of the grains. Assuming that they are uniformly distributed in space and have a unique characteristic amplitude, $\tau(t_w)$ is simply proportional to the inverse of the yielding frequency [17,23].

The observed dynamical arrest is rather insensitive to the packing fraction of the sample. Any satisfactory description thus requires the introduction of another internal variable that will control the instantaneous response of the pack to gentle vibrations. Here we propose to focus on contact stress distribution. It has been observed that the form of this distribution is almost independent of the volume fraction of the pack and the preparation history [1–3]. However, standard measurements are not sensitive enough to detect small variations in these distributions that may follow from very gentle mechanical vibrations. We will argue here that the observed evolution of the dynamics follows from a slow modification of the stress distribution which effectively strengthens the granular pile.

To model such a dynamics, we picture the granular assembly as a set of independent contacts (whose total number is supposed to be a constant.) Each contact is characterized at time t by the normal and tangential component of the contact force which we denote σ_n and σ_t, respectively. Mechanical equilibrium imposes that $\sigma_t < \mu\sigma_n$. For simplicity, we will make the friction coefficient μ equal to 1 in the rest of the Letter. For a given packing structure, the state of the internal stress field is characterized by the two variables stress density distribution $P_\sigma(\sigma_n, \sigma_t)$. As the cell is vibrated, mechanical waves traveling through the sample induce random stress fluctuations at each contact. Such perturbations can locally trigger the rupture of a contact, whenever the shear force σ_t overcomes the normal force σ_n. We assume an exponential distribution $\chi(\delta\sigma)$ of the maximum force fluctuation induced by the tap on each contact:

$$\chi(\delta\sigma) = \frac{1}{\overline{\delta\sigma}} \exp\left(-\frac{\delta\sigma}{\overline{\delta\sigma}}\right). \tag{2}$$

In this expression, the mean force fluctuation $\overline{\delta\sigma}$ is an increasing function of the applied vibration amplitude. Thus the probability for a given contact to yield following a single tap writes

$$\omega_y(\sigma_n, \sigma_t) = \exp\left(-\frac{\sigma_n - \sigma_t}{\overline{\delta\sigma}}\right). \tag{3}$$

This expression is a consequence of the peculiar form [Eq. (2)] taken for the tap induced force fluctuations $\chi(\delta\sigma)$. However, the main results of the present model remain valid for any fast decaying distribution (faster than a power law).

After a yielding event, the force at the renewed contact is chosen from a given "rejuvenated" distribution which we consider intrinsic to the system. The distribution of normal forces in a granular pile under a moderate load is known to exhibit an exponential tail at high forces and a plateau below the mean force [1–3]. Numerical measurements have also shown that, for a given value of the normal force, the tangential forces are uniformly distributed between 0 and the sliding limit $\sigma_t = \mu\sigma_n$ (in a 2D case) [21]. We use these different observations to infer the form of the rejuvenated distribution $P_{\text{rej}}(\sigma_n, \sigma_t)$, which thus writes

$$P_{\text{rej}}(\sigma_n, \sigma_t) = \frac{1}{\sigma_0 \cdot \sigma_n} \exp\left(-\frac{\sigma_n}{\sigma_0}\right), \tag{4}$$

where σ_0 is the mean stress inside the pile. For simplicity, we have omitted the plateau saturation of the distribution at low forces. We can now derive the dynamical equation of evolution of the stress distribution P_σ:

$$\frac{\partial P_\sigma(\sigma_n, \sigma_t)}{\partial t} = -P_\sigma(\sigma_n, \sigma_t)\omega_y(\sigma_n, \sigma_t) + P_{\text{rej}}(\sigma_n, \sigma_t)F(P_\sigma), \tag{5}$$

where $F(P_\sigma)$ is the total frequency of sliding events which is self-consistently defined as

$$F(P_\sigma) = \iint_{\sigma'_t < \sigma'_n} P_\sigma(\sigma'_n, \sigma'_t)\omega_y(\sigma'_n, \sigma'_t)d\sigma'_n d\sigma'_t. \tag{6}$$

The present description exhibits many common features with Bouchaud's trap model [22] of glass transition. In the latter, the internal dynamics of a glassy liquid is pictured as a succession of thermal escapes from energy wells of various depths. In an analogous way, each contact here can be considered as frozen in a mechanical trap (the local solid friction cone), the depth of which depends on the relative amplitude of the normal and shear components of the contact force. Moreover, in the absence of temperature, mechanical vibrations play the role of the energy source by allowing individual contacts to hop out of their trap.

As in the trap model, we thus observe two limiting regimes depending on the relative values of the intensity of the applied stress $\overline{\delta\sigma}$ and the width σ_0 of the rejuvenated distribution. For large vibrations, i.e., $\overline{\delta\sigma} > \sigma_0$, the rejuvenated stress distribution is a stationary solution of Eq. (6), and the yielding frequency is constant in time. In contrast, for $\overline{\delta\sigma} < \sigma_0$, the stress distribution evolves endlessly. Figure 4 shows the time evolution of P_σ obtained by numerically solving Eq. (6) for $\overline{\delta\sigma} = \sigma_0/20$, starting with $P_\sigma = P_{\text{rej}}$. It shows that fragile contacts — contacts of low normal force or close to the sliding limit (inset) — are slowly depleted. As a result, the number of sliding events per time unit decays. More quantitatively,

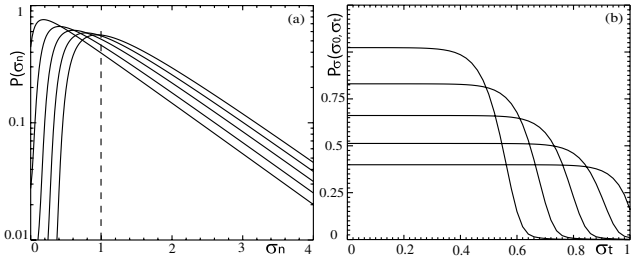

FIG. 4. Results of the numerical model for $\sigma_0 = 1$ and $\overline{\delta\sigma} = \sigma_0/20$: (a) distributions of normal forces for $t_w = 1$, 10, 100, 1000, and 10 000 (from left to right); (b) distributions of tangential forces for $\sigma_n = \sigma_0$ at the same times t_w (from bottom to top).

we find that the characteristic time between events grows linearly with the elapsed time, in reasonable agreement with our observations (Fig. 3.)

We have evidenced, through MSDWS measurements, the existence of a slowing down of the microscale dynamics over more than five decades in gently vibrated granular piles. This behavior is reminiscent of the aging process observed in glassy systems. This dynamics appears to be weakly connected to the overall grain-scale structure, which suggests a two-level description of granular systems. Under strong vibrations, a granular pile evolves through the restructuration of the piling geometry, leading to a slow irreversible compaction. In this regime, the forces network is rapidly renewed and shows no history-dependent behavior. Under gentle vibrations however, the geometry of the pile is essentially frozen but the forces network can still evolve by slowly depleting the most fragile contacts. This leads to an effective reinforcement of the pack structure as is evidenced in the present study by the decrease of vibration induced plastic events.

The precise nature of the yielding events remains however unclear. In particular, one might expect large spatial and temporal correlations between the events, which we cannot probe with DWS. Another important question concerns the relevance of such modifications to the onset of macroscopic flow. For instance, does the observed reinforcement of the force networks play a role in changing the threshold of avalanche triggering or shear-banding appearance?

We wish to thank Luca Cipelletti and Jean-Marc di Meglio for fruitful discussions and Deniz Gunes for helping us with the estimation of $l^\star$.

*Electronic address: georges.debregeas@college-de-france.fr

[1] D. M. Mueth, H. M. Jaeger, and S. R. Nagel, Phys. Rev. E **57**, 3164 (1998).
[2] G. Løvoll, K. J. Måløy, and E. G. Flekkøy, Phys. Rev. E **60**, 5872 (1999).
[3] D. L. Blair, N. W. Mueggenburg, A. H. Marshall, H. M. Jaeger, and S. R. Nagel, Phys. Rev. E **63**, 041304 (2001).
[4] L. Staron, J.-P. Vilotte, and F. Radjai, Phys. Rev. Lett. **89**, 204302 (2002).
[5] J. Desrues, R. Chambon, M. Mokni, and F. Mazerolle, Geotechnique **46**, 529 (1996).
[6] C. H. Liu, Phys. Rev. B **50**, 782 (1994).
[7] D. Howell, R. P. Behringer, and C. Veje, Phys. Rev. Lett. **82**, 5241 (1999).
[8] M. Da Silva and J. Rajchenbach, Nature (London) **406**, 708 (1999).
[9] J. B. Knight, C. G. Fandrich, C. N. Lau, H. M. Jaeger, and S. R. Nagel, Phys. Rev. E **51**, 3957 (1995).
[10] P. Philippe and D. Bideau, Europhys. Lett. **60**, 677 (2002).
[11] C. Lesaffre, V. Mineau, D. Picart, and H. Van Damme, C. R. Acad. Sci. Paris, Ser. IV **1**, 647 (2000).
[12] L. Cipelletti and D. A. Weitz, Rev. Sci. Instrum. **70**, 3214 (1999).
[13] V. Viasnoff, F. Lequeux, and D. Pine, Rev. Sci. Instrum. **73**, 2336 (2002).
[14] N. Menon and D. J. Durian, Science **275**, 1920 (1997).
[15] K. Kim, J. J. Park, J. K. Moon, H. K. Kim, and H. K. Pak, J. Korean Phys. Soc. **40**, 983 (2002).
[16] $l^\star$ was found equal to 220 $\pm$ 20 μm, which allows in our geometry the use of a diffusive model for the light in the sample [17].
[17] G. Maret and P. E. Wolf, Z. Phys. B **65**, 409 (1987); D. J. Pine, D. A. Weitz, P. M. Chaikin, and E. Herbolzheimer, Phys. Rev. Lett. **60**, 1134 (1988).
[18] A. Knaebel, M. Bellour, J.-P. Munch, V. Viasnoff, F. Lequeux, and J. L. Harden, Europhys. Lett. **52**, 73 (2000).
[19] V. Viasnoff and F. Lequeux, Phys. Rev. Lett. **89**, 065701 (2002).
[20] L. Cipelletti, L. Ramos, S. Manley, E. Pitard, D. A. Weitz, E. E. Pashkovski, and M. Johansson, Faraday Discuss. **123**, 237 (2003).
[21] F. Radjai, M. Jean, J.-J. Moreau, and S. Roux, Phys. Rev. Lett. **77**, 274 (1996).
[22] J.-P. Bouchaud, J. Phys. I (France) **2**, 1705 (1992).
[23] D. J. Durian, D. A. Weitz, and D. Pine, Science **252**, 686 (1991).

THEME 3 : PROCESSUS DISSIPATIFS LOCAUX DANS LES MOUSSES AQUEUSES

Résumé : Nous avons mesuré les forces d'adhésion dynamiques qui s'exercent entre deux bulles en contact oscillant par une analyse fine des profils de bulles. Ces résultats ont pu être compris dans le cadre d'un modèle dynamique d'échange des molécules tensio-actives entre les films de savon. Ces mesures de forces à l'échelle des bulles individuelles ont permis d'interpréter quantitativement des mesures rhéologiques obtenues sur des mousses tridimensionnelles de même composition chimique.

Les mousses aqueuses, comme d'autres matériaux macroscopiquement divisés tels que les émulsions, les colloïdes denses ou les milieux granulaires confinés, ont un comportement rhéologique qui se caractérise par une réponse élastique à faible déformation, et plastique au-delà d'une déformation seuil. A faible fréquence de sollicitation, la dissipation d'énergie est principalement contrôlée par les réarrangements locaux de la structure (processus T1, voirFigure 3) induits par le forçage lui-même ou par le phénomène de mûrissement d'Ostwald. A haute fréquence cependant, les mesures rhéologiques linéaires montrent une croissance rapide du module de perte G'' (qui caractérise la dissipation visqueuse) en puissance ½ de la fréquence qui révèle l'existence d'autres processus dissipatifs dont l'origine microscopique reste débattue.

Nous avons cherché à comprendre ce régime rhéologique sous sollicitation rapide en étudiant les forces d'adhésion dynamiques s'exerçant entre deux bulles de savon. Nous avons mis en place un dispositif expérimental original qui permet la mise en contact de deux bulles hémisphérique, puis la modulation de la distance qui sépare leur support, tout en mesurant avec une grande précision les profils des films (Figure 6A). L'évolution des différentes quantités géométriques est extraite de ces profils, notamment l'angle de contact θ que forment les bulles au niveau du film central, afin d'en déduire les forces d'adhésion s'exerçant à chaque instant. Ce dispositif expérimental est doublé d'une simulation numérique fondée sur un calcul de minimisation de surface adapté du programme *Surface Evolver* développé par Kenneth Brakke (Figure 6B).

En régime statique, nous avons mesuré l'écart de l'angle θ à la valeur 120° prévue dans une situation de mousse infiniment sèche. Cet écart résulte d'un effet de tension de ligne négative induit par la présence d'un bord de Plateau de volume fini à l'intersection des films de savon. Cet écart peut être quantitativement prédit en fonction du volume de liquide et du rayon du film séparant les deux bulles. En régime dynamique – *i.e.* lorsque la distance entre les supports des bulles est modulée sinusoïdalement – un écart à l'angle statique apparaît qui traduit l'existence de processus visco-élastique au sein des films de savon ou dans le bord de Plateau. En variant la fréquence de modulation de cette distance, nous avons déterminé le spectre de la réponse linéaire du système. Ce résultat a pu être interprété microscopiquement dans le cadre d'un modèle prenant en compte les échanges se produisant au sein et entre les monocouches tensio-actives couvrant les différents films[1].

A partir de ces mesures géométriques locales (*i.e.* à l'échelle de deux bulles), il est possible de prédire la réponse mécanique d'un réseau régulier de bulles soumis à une déformation oscillante. Cette prédiction s'est révélée compatible avec des mesures rhéologiques réalisées, en collaboration avec Sylvie Cohen-Addad et Reinhardt Hohler de l'Université Paris-Est Marne-la-Vallée, sur des mousses macroscopiques de même composition chimique[2]. Ce résultat semble indiquer que le comportement rhéologique des mousses aqueuses à haute fréquence est contrôlé principalement par les processus d'échanges de tensioactifs entre les monocouches couvrant les films liquides. Il permet de préciser la façon dont il est possible de moduler les propriétés de ces matériaux à partir de leur formulation physico-chimique.

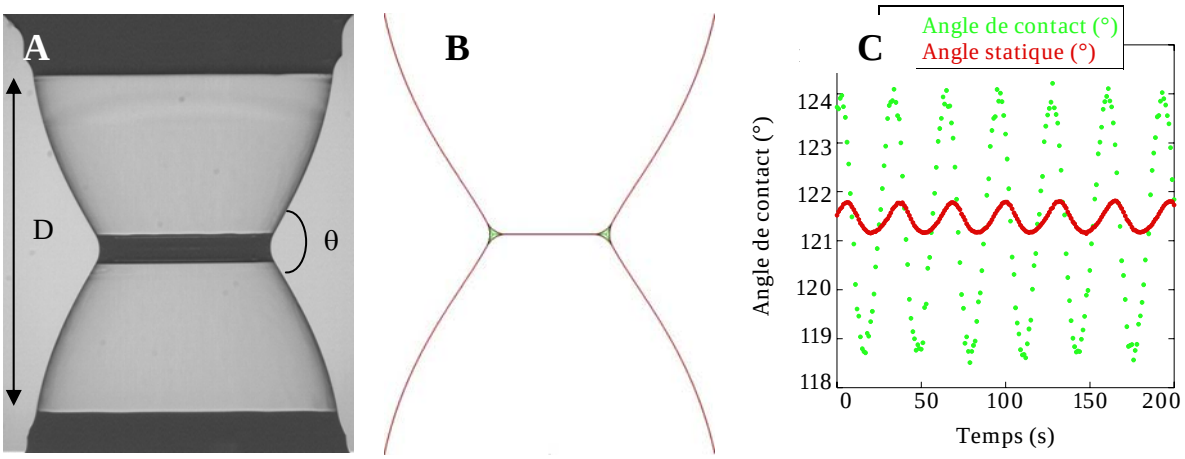

Figure 6 : (A) Image de deux bulles hémisphériques en contact. Le film central apparaît épais du fait de l'accumulation du liquide dans le bord de Plateau (la région d'intersection de trois films de savon). La distance entre les buses D peut être modulée ; à chaque instant, l'angle θ que forment les deux bulles est extrait par analyse d'image. (B) Profil prédit numériquement par minimisation de la surface totale (Surface Evolver). (C) Evolution de l'angle de contact θ en fonction du temps lors d'une expérience durant laquelle la distance D est modulée sinusoïdalement. La trace rouge correspond à l'angle prédit par minimisation des surfaces. L'écart entre la valeur mesurée (en vert) et l'angle statique prédit résulte des processus de dissipation viscoélastique dans les films.

Références :

1. Statics and dynamics of adhesion between two soap bubbles, S. Besson and G. Debrégeas, *Eur. Phys. J. E* 24, 109-117 (2007)
2. Dissipation in a Sheared Foam: From Bubble Adhesion to Foam Rheology, S. Besson, G. Debrégeas, S. Cohen-Addad and R. Höhler, *Phys. Rev. Lett.* 101, 214504(2008)

Eur. Phys. J. E **24**, 109–117 (2007)
DOI 10.1140/epje/i2007-10219-y

THE EUROPEAN PHYSICAL JOURNAL E

Statics and dynamics of adhesion between two soap bubbles

S. Besson[a] and G. Debrégeas

Laboratoire de Physique Statistique, CNRS UMR 8550, 24, rue Lhomond, 75231 Paris Cedex 05, France

Received 19 March 2007 and Received in final form 7 July 2007
Published online: 22 October 2007 – © EDP Sciences / Società Italiana di Fisica / Springer-Verlag 2007

Abstract. An original set-up is used to study the adhesive properties of two hemispherical soap bubbles put into contact. The contact angle at the line connecting the three films is extracted by image analysis of the bubbles profiles. After the initial contact, the angle rapidly reaches a static value slightly larger than the standard 120° angle expected from Plateau rule. This deviation is consistent with previous experimental and theoretical studies: it can be quantitatively predicted by taking into account the finite size of the Plateau border (the liquid volume trapped at the vertex) in the free energy minimization. The visco-elastic adhesion properties of the bubbles are further explored by measuring the deviation $\Delta\theta_d(t)$ of the contact angle from the static value as the distance between the two bubbles supports is sinusoidally modulated. It is found to linearly increase with $\Delta r_c/r_c$, where r_c is the radius of the central film and Δr_c the amplitude of modulation of this length induced by the displacement of the supports. The in-phase and out-of-phase components of $\Delta\theta_d(t)$ with the imposed modulation frequency are systematically probed, which reveals a transition from a viscous to an elastic response of the system with a crossover pulsation of the order $1\,\mathrm{rad}\cdot\mathrm{s}^{-1}$. Independent interfacial rheological measurements, obtained from an oscillating bubble experiment, allow us to develop a model of dynamic adhesion which is confronted to our experimental results. The relevance of such adhesive dynamic properties to the rheology of foams is briefly discussed using a perturbative approach to the Princen 2D model of foams.

PACS. 47.55.D- Drops and bubbles – 47.55.dk Surfactant effects – 83.80.Iz Emulsions and foams

1 Introduction

Liquid foams are concentrated dispersions of gas bubbles in a liquid matrix. Their mechanical properties have been the focus of a number of studies in the recent past [1–3]. Liquid foams exhibit quasi-elastic behavior up to a finite yield stress or strain beyond which they flow like shear-thinning viscous fluids. Most of the elastic response originates from the variation of the total film area induced by an applied shear. The resulting shear modulus scales as $\mu = 2\gamma/R$, where 2γ is the surface tension of the soap film, and R the average radius of the bubbles. The dissipation is controlled, in major part, by irreversible rearrangements of the bubbles (T1 events).

Other mechanisms of energy storage and dissipation, however, contribute to the viscoelastic moduli of the foam. They have been thoroughly discussed theoretically [4, 5]. One is associated with the interfacial viscoelasticity of the soap films, which can be independently measured using a wide range of experimental techniques (oscillating barriers [6, 7], thin-film interfaces [8], oscillating bubble/drop [9–11]). They all consist in submitting a single mono- or bi-layer to an oscillating stretching while measuring the evolution of the surface tension. The second source of dissipation takes place in the Plateau borders, the region of the foam where the films meet and where most of the liquid content is trapped. As the foam is strained, the Plateau borders move relatively to the soap films to which they are connected, inducing dissipative viscous flows. This viscous drag force has been extensively studied but only in a situation where the Plateau border is in contact with a solid surface [12–15].

Relating these local measurements (interfacial rheology and Plateau border viscous drag force) to the global rheology of the foams is tricky. First, it is difficult to actually separate the different modes of dissipation. In a real foam, Ostwald ripening (the disproportionation of bubbles induced by gas diffusion through the films) induce T1 events even in the absence of an imposed strain. Second, due to the many modes of accessible deformation, the motion of the vertices in a foam under simple strain is not affine. Describing their trajectory becomes extremely difficult when the foam is polydisperse.

Beyond these issues, one can also question the relevance of measurements performed with an isolated film to describe the behavior of a macroscopic foam. In all the techniques currently used to estimate the rheological properties of the films, the surfactant layers are confined

[a] e-mail: sebastien.besson@lps.ens.fr

by solid barriers. In contrast, films in a real foam are bounded by fluid Plateau borders which may allow the transfer of surfactants from one side to another. In the case of Plateau borders viscous drag, the situation is even worst: the resistance to motion is measured by dragging a Plateau border along a solid wall, which imposes a very different hydrodynamic boundary to the flow by comparison with a self-supported Plateau border.

One attempt to extract information about local dissipation within a macroscopic foam has been recently proposed by Durand and Stone [16]. They optically studied the dynamic of T1 events in a confined 2D foam (a monolayer of bubbles squeezed between two solid plates) and were able to relate the duration of the plastic process with intrinsic rheological properties of the soap films. This experiment enables the authors to study plastic processes *in situ*, although it is limited to a confined geometry. But the use of T1 events as the deformation mechanism does not allow one to modulate in a controlled way the dynamics of local deformation of the set of bubbles (although this might actually be feasible with minor modification of the authors' experimental procedure).

In this article, we propose a new approach to study local elastic and dissipative processes in a configuration more directly amenable to 3D foams. Two hemispherical bubbles are put into contact and their relative distance is modulated at various frequencies. In this configuration, the central film separating the two bubbles is bounded by a self-supported Plateau border whose radius oscillates with the distance between the two bubbles supports. We focus on angular measurements at the contact line which provide most of the relevant information concerning the elastic and dissipation processes.

The article is organized as follows. In Section 2, the experimental set-up, the optical measurements and image analysis procedure are detailed. The static results of contact angle measurements are presented in Section 3, together with data obtained from a numerical simulation. Section 4 focuses on the dynamic properties of adhesion and also presents the results of standard rheological interfacial measurements performed on single films using the same soap solution. These results are discussed in Section 5: a microscopic model, which describes the transport of surfactant molecules between the interfaces and the bulk as well as between adjacent interfaces, is developed. Its prediction in terms of angular moduli is confronted to the experimental measurements. In Section 6, the consequence of this angular response for the rheology of foams is discussed within the scope of the Princen 2D hexagonal model [17]. Conclusion and perspectives are drawn in Section 7.

2 Experiments

A hemispherical bubble is formed by blowing air at the cone-shaped end of a stainless-steel tube, of external radius $R = 7\,\mathrm{mm}$, filled with a soap solution (Fig. 1). The liquid in the tube is connected through a porous disk (Duran, diameter: 2.8 mm, height: 5 mm) to a reservoir. Once

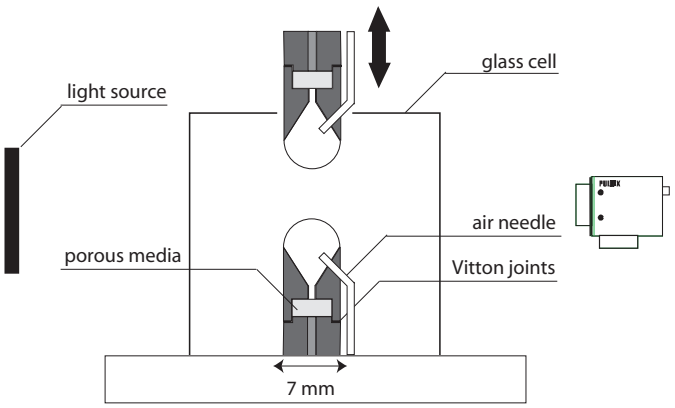

Fig. 1. Schematic of the experimental double-bubble device.

the bubble is formed, the reservoir is lowered a few centimeters to impose a small negative pressure difference between the liquid and gas phases. The disk porosity is fine enough (pore size: 10–16 μm) to prevent the bubble from being sucked down. The entire device is enclosed in a glass cell ($40 \times 40 \times 40\,\mathrm{cm}$) to limit evaporation and increase the bubbles lifetime. In all the experiments, the soap solution is made of tetramethyltetradecylammonium bromide (TTAB purchased from Sigma-Aldrich) 3 g/L in a water/glycerol mixture (volume ratio of 75/25).

This device is used in two types of experiments. In single-bubble experiments, a section of the air tube is squeezed between two plates whose separation can be sinusoidally modulated using a DC motor (Newport, LTA-HS). A pressure sensor (Validyne, DP103) allows us to simultaneously monitor the pressure drop between the inside and outside of the bubble. In the double-bubble setup, a similar device is placed on top of the first one (Fig. 1) and their axes are carefully aligned. The top device is mounted on a vertical displacement stage attached to the DC motor.

The set-up is illuminated by a diffusive light source (Schott, Backlight). The shadow image of the bubbles is captured on a CCD camera equipped with a telecentric objective (Navitar, 6×) to allow accurate angular and length measurements. Depending on the studied frequency, two cameras are used: a Pulnix TM-1320 CL and a Mikrotron MC1310 with frame rates up to 15 frames/s and 240 frames/s, respectively. Image capture is synchronized with the motor motion and pressure recording. The bubbles profiles are extracted by image analysis with a sub-pixel resolution using the software IDL (see Fig. 2(c)). The symmetry axis is determined and defines the cylindrical coordinates (r, z). For both bubbles, the profiles $r(z)$ are fitted to the Young-Laplace equation which relates the local curvature $\frac{1}{R'} + \frac{1}{R''}$ to the pressure drop ΔP across the film:

$$\Delta P = 2\gamma\left(\frac{1}{R'} + \frac{1}{R''}\right). \tag{1}$$

The profile equation $r(z)$ thus obeys the differential equation

$$\frac{r(z)}{\sqrt{1 + r'(z)^2}} = \frac{\Delta P}{4\gamma} r(z)^2 + \lambda\,, \tag{2}$$

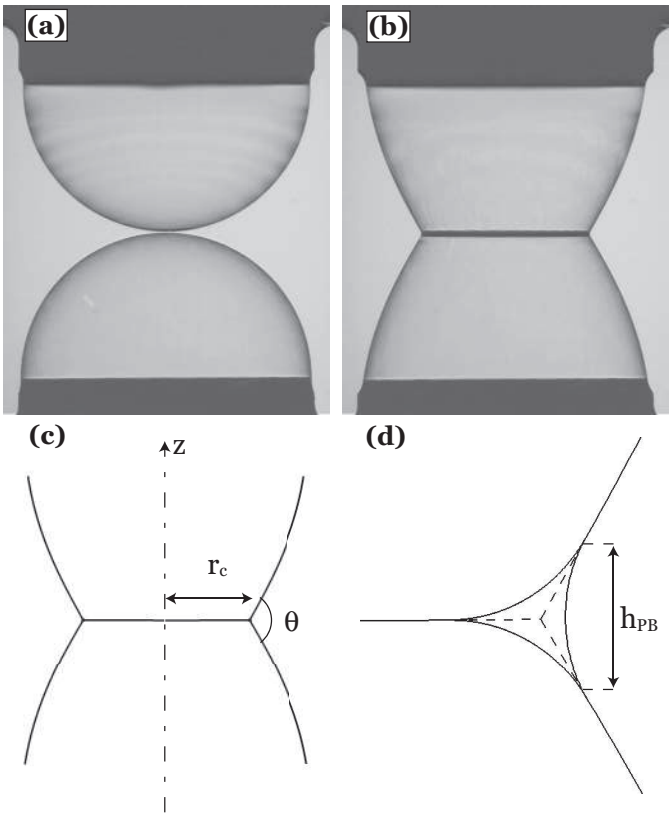

Fig. 2. Images of a double-bubble static adhesion experiment (a) before contact and (b) just after contact. Results of the image analysis: (c) external profiles fitted by the Young-Laplace equation from which the central film radius r_c and contact angle θ are extracted, (d) reconstructed Plateau border. The height h_{PB} is defined as the distance between the top and bottom intersection points of the Plateau border interfaces.

where 2γ is the surface tension of the soap film; the parameter λ results from the integration of equation (1) and is set by the boundary conditions. For each bubble, the set of parameters $(\frac{\Delta P}{4\gamma}, \lambda)$ is extracted from the best fit of the region of the profiles outside the Plateau border. The prolongations of the reconstructed profiles intersect in the Plateau border and define a contact radius r_c and a contact angle θ as shown in Fig. 2(c). Similarly, the three interfaces which delimit the Plateau border obey the same equation (2) with the term $\frac{\Delta P}{4\gamma}$ replaced by $\frac{\Delta P}{2\gamma}$ since these are single air/water interfaces. Here ΔP corresponds to the pressure difference between the liquid in the Plateau border and the gas phase (bubble or atmosphere). By fitting the external profile, we extract the set of parameters $(\frac{\Delta P}{2\gamma}, \lambda_l)$ and reconstruct the Plateau border (see Fig. 2(d)).

3 Dynamics of first contact and static equilibrium angle

Two bubbles are brought into contact at vanishing low speed. Time 0 is defined by the recording time of the image of the first contact. The time evolution of the central film radius r_c and contact angle θ at short times are shown in Figure 3. It exhibits a transient of a few seconds during which both parameters significantly vary. The first ~ 0.1 s corresponds to the rapid formation of the central film: only the end of this phase can be captured even with the fast camera. During the next few seconds, the radius and contact angle keep increasing. This second stage is associated with the capillary drainage of the freshly formed film toward the Plateau border which allows pressure equilibration within the liquid phase. This process can be monitored by measuring the evolution of the Plateau border height h_{PB} (see Fig. 2(d) for its definition) which appears to evolve with the same characteristic time as the contact radius (Fig. 3). For $t \gtrsim 10$ s, the system is equilibrated but a slow decay of r_c is still observable due to gas diffusion

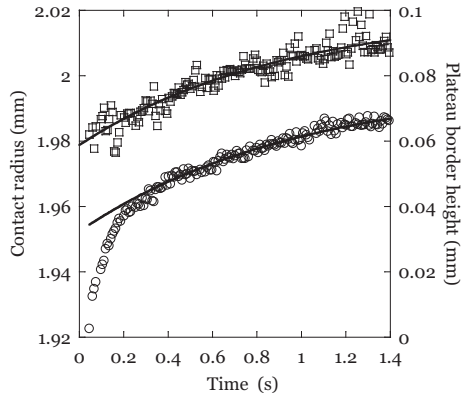

Fig. 3. Short-times evolution of the contact radius (circles) and the Plateau border height (squares) as a function of time for two contacting bubbles. During the first 0.2 s, the fast rise of the contact radius corresponds to the initial growth of the central film. After 0.2 s, the evolution of the contact radius is to be compared to the one of the Plateau border height. Both series of measurements are adjusted by rising exponential fits of the type $x_0 + \Delta x(1 - e^{\frac{-t}{\tau}})$ (solid lines) and highlight a characteristic time τ of the order of 1 s.

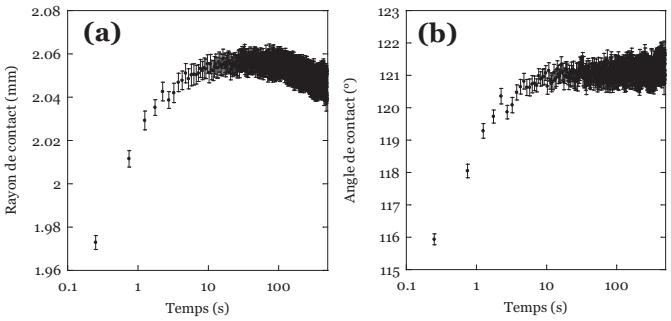

Fig. 4. Long-times evolution of (a) the contact angle and (b) the contact radius as a function of the time during a contacting-bubbles experiment. After an initial growth, both series reach constant values, the contact angle value being slightly higher than the predicted 120° from the Plateau rule. The decay of the contact radius after 60 s is attributed to the gas diffusion outside the bubble. The experiment ends up when one of the two bubbles break.

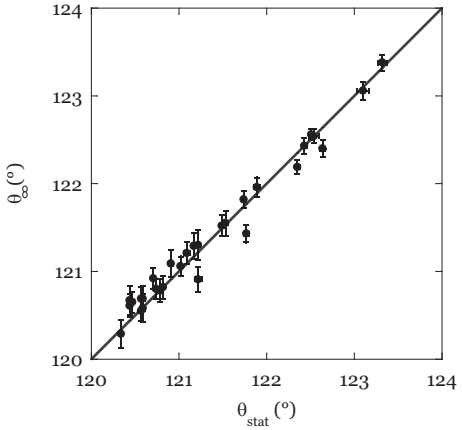

Fig. 5. Experimental static contact angle θ_∞ as a function of the angle predicted by Fortes law θ_{stat} (Eq. (3)) for various values of the radius r_c and the Plateau border volume. Each data point corresponds to the average of angular measurements performed after 10 s of contact.

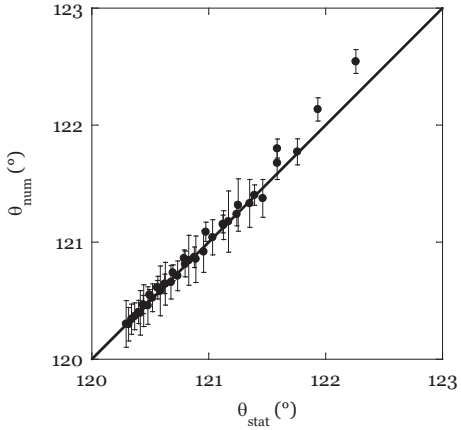

Fig. 6. Numerical contact angle θ_{num} obtained from surface evolver simulations as a function of the angle predicted by Fortes law θ_{stat} (Eq. (3)) for various values of the imposed Plateau border volume.

through the films (Fig. 4). This process does not affect the value of the contact angle θ which remains constant until the bubbles break up (after a few minutes).

We define θ_∞ as the value of the contact angle for time $t > 10$ s. For all experiments, θ_∞ is found to be larger than 120°, the value predicted by Plateau rule [18]. Such a deviation has been previously observed in various experiments [19–21]. In the last reference, similar measurements were performed on a single catenoid separated by a soap film. The contact angle between both catenoidal films was found to grow linearly with the ratio $\frac{r_{PB}}{r_c}$, where r_{PB} is the Plateau border curvature radius and r_c the central film radius.

This deviation can be qualitatively understood by first considering an infinitely dry foam. In this case, the force equilibrium at the contact line imposes the three films to meet at 120°. Decorating the line with a Plateau border reduces the total area of the films by a quantity $2S_{dry} - S_{PB}$ [22] which is a (negative) decreasing function of the Plateau border volume. The presence of a Plateau border is thus associated with a negative line tension. In the specific case of the double bubble, this effect has been described by Fortes and Teixeira [23]. They predict a contact angle in the presence of Plateau border given by

$$\theta_{stat} = 120 + \frac{180}{\pi}\frac{1}{4\pi r_c^2\sqrt{3}}(2S_{dry} - S_{PB}). \qquad (3)$$

In order to test this expression, several contacting-bubbles experiments are performed with different values of contact radius and Plateau border height. When the top bubble is initially formed, a liquid droplet is suspended at its apex. After contact, part of this liquid gathers in the Plateau border but a fraction of it flows down the lower bubble. If one separates the two bubbles then brings them into contact again, part of the liquid is further eliminated. The Plateau border size can thus be varied by applying successive contacts and separations of the bubbles. For each experiment, the final value of the contact angle as well as $S_{dry} - S_{PB}$ are measured. Figure 5 shows the measured angle θ_{stat} as a function of the prediction of equation (3).

It should be noticed that this model ignores disjoining-pressure effects such as those reported in references [24, 25]. Although gravity drainage tends to decrease the films thickness, this process is largely slowered in our experiment by the presence of glycerol in the solution. The thickness of the films have not been measured, but in all experiments, the films diffuse light which indicates that their thickess is larger than $\sim 1\,\mu$m. In this range, disjoining pressure is negligible. Consistently, we do not observed any evolution of the contact angle with time beyond ~ 10 s after initial contact.

This result was independently confirmed by simulations of the double-bubble experiment carried out using surface evolver [26]. This software allows one to calculate minimal surface configurations under a given set of conditions. Two contacting bubbles of fixed volume are generated with different volumes of the Plateau border. After several minimization cycles, the equilibrated configuration is treated the same way as for the experiments. Figure 6 shows the numerical contact angle *versus* the predicted contact angle value for various Plateau border volumes.

The agreement of the experimental and numerical results with Fortes and Teixeira's model validates the decoration law for the double bubble. It also demonstrates the accuracy of the angle measurement procedure. In the rest of the article, expression (3) will be used in order to calculate, at any moment, the equilibrium contact angle $\theta_{stat}(t)$. This reference angle will be subtracted from the measured angle in order to extract the dynamic deviation $\Delta\theta_d = \theta(t) - \theta_{stat}(t)$.

4 Dynamics of adhesion

In order to probe the dynamic response of the contact angle, a sinusoidal displacement of the upper tube is applied

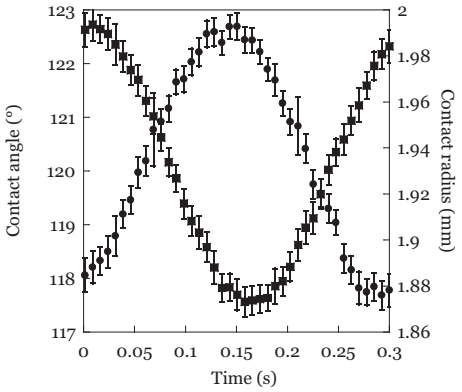

Fig. 7. Evolution of the contact radius (squares) and the contact angle (circles) as a function of the time over an oscillating period for an oscillating amplitude of 0.2 mm at a pulsation of $20\,\mathrm{rad}\cdot\mathrm{s}^{-1}$. The error bars are calculated from the uncertainties on the fitting parameters (Eq. (2)). Typical standard deviations are equal to $7\,\mu$m for the contact radius and 0.2° for the contact angle.

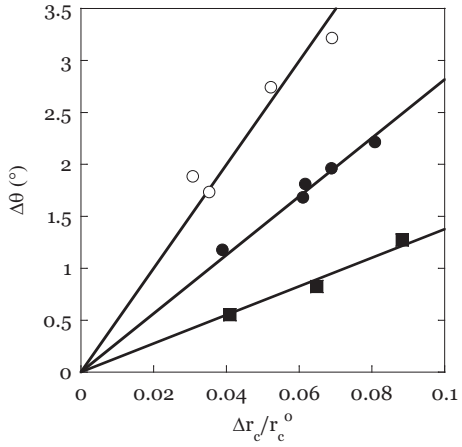

Fig. 8. Linearity of the amplitude of the dynamic angle deviation with the amplitude of the normalized contact radius variations at different frequencies. Squares: $0.2\,\mathrm{rad}\cdot\mathrm{s}^{-1}$. Circles: $1\,\mathrm{rad}\cdot\mathrm{s}^{-1}$. Diamonds: $5\,\mathrm{rad}\cdot\mathrm{s}^{-1}$.

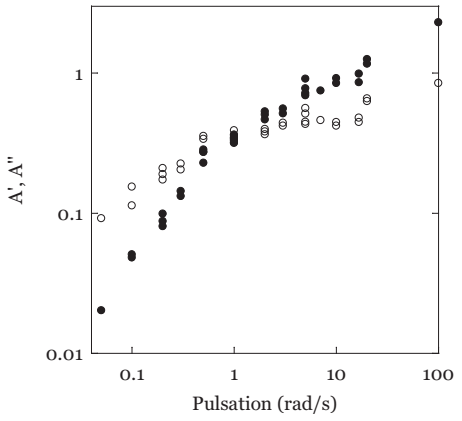

Fig. 9. Evolution of the angular elastic and viscous moduli, estimated from equations (6) and (7), with the frequency of the oscillation. Closed circles: elastic modulus. Open circles: loss modulus.

at controlled pulsations in the range 0.01–$20\,\mathrm{rad}\cdot\mathrm{s}^{-1}$. The double-bubble system is prepared as previously described. All experiments are performed with a contact radius $r_c \approx 2\,\mathrm{mm}$ and a Plateau border height $h_{PB} \approx 0.2\,\mathrm{mm} \ll r_c$. Figure 7 shows the typical time evolution of $r_c(t)$ and $\theta(t)$. The corrected contact angle, $\theta_{stat}(t)$, calculated from equation (3), varies between 120.50° and 120.56°. Therefore, the main contribution to the observed oscillation of $\theta(t)$ is due to dynamic effects. The evolution of these two parameters is decomposed as

$$r_c(t) = r_{c0} + \Delta r_c(\omega)\cos(\omega t), \tag{4}$$

$$\Delta\theta_d(t) = \Delta\theta(\omega)\cos(\omega t + \phi(\omega)). \tag{5}$$

It should be noted that r_{c0} is not strictly constant: it slightly decreases as a consequence of the gas diffusion (Fig. 4(b)). To precisely measure $r_c(\omega)$, $\Delta\theta(\omega)$ and $\phi(\omega)$, $r_c(t)$ and $\Delta\theta_d(t)$ are therefore filtered to extract the Fourier component associated with the imposed frequency. Figure 8 shows the dependence of $\Delta\theta$ with $\Delta r_c/r_{c0}$ for three different oscillation frequencies. It shows that the contact angle response is linear with the imposed solicitation. This allows one to define two moduli associated with the in-phase and out-of-phase responses of the contact angle to the modulation of the contact radius:

$$A'(\omega) = -\frac{\Delta\theta(\omega)}{\Delta r_c(\omega)} r_{c0}\cos(\phi(\omega)), \tag{6}$$

$$A''(\omega) = -\frac{\Delta\theta(\omega)}{\Delta r_c(\omega)} r_{c0}\sin(\phi(\omega)). \tag{7}$$

Figure 9 shows the evolution of A' and A'' as the pulsation ω is varied over 3 decades. It reveals a transition from a viscous regime at low frequency to an elastic regime at high frequency, with a crossover around $1\,\mathrm{rad}\cdot\mathrm{s}^{-1}$.

The existence of an in-phase component of the dynamic angle signal cannot be accounted for by dissipation in the Plateau border alone. In contrast, it can be understood by considering the viscoelastic behavior of the soap films [16, 27]. As the distance between the bubbles are modulated, the films area varies which in turn induces a variation of their surface tension. In Gibbs approach, the surface tension $\gamma(t)$ associated with a sinusoidal modulation of the film surface area $S(t) = S^0 + \Delta S\cos(\omega t)$ is written, in the limit $\Delta S/S^0 \approx 0$:

$$\gamma(t) = \gamma_0 + E'(\omega)\frac{\Delta S}{S_0}\cos(\omega t) + E''(\omega)\frac{\Delta S}{S_0}\sin(\omega t), \tag{8}$$

where $E^*(\omega) = E'(\omega) + iE''(\omega)$ is the dilational complex modulus [28]. This parameter can be independently evaluated by sinusoidally modulating the volume of a single bubble while recording its radius R and the difference between the inside and the outside pressure ΔP, from which its surface tension is determined using the Young-Laplace relation $2\gamma = \Delta P/2R$. The frequency diagram of both moduli is plotted in Figure 10.

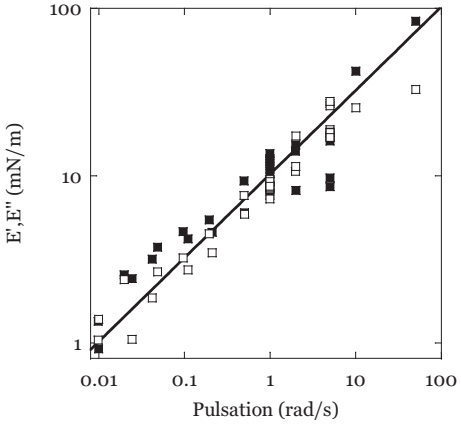

Fig. 10. Evolution of the dilational elastic and viscous moduli with the frequency of the oscillation for an oscillating-bubble experiment. Closed squares: elastic modulus. Open squares: viscous modulus. The dispersion is mainly due to uncertainties on the measurement of the internal pressure. Experimental data are fitted by the expressions of the Lucassen model above the critical micellar concentration (solid line).

Both elastic and viscous moduli exhibit a similar increase with the pulsation in $\sqrt{\omega}$ (as shown by the solid line in Fig. 10). Such a behavior of the dilational moduli has been predicted by Lucassen, in the limit of low frequency, for solutions below [6] and above [29] the critical micellar concentration. In these models, the surfactants adsorption at the interface is limited by diffusion in the bulk. This process defines a characteristic time set by the physico-chemical properties of the bulk solution.

5 Interpretation

In this section, we attempt to relate the double-bubble angular measurements to the film rheological moduli obtained from the single-oscillating-bubble experiment. In order to do so, we separately describe the evolution of each monolayer characterized at each time by their area and surface tension denoted S_i and γ_i, respectively (see Fig. 11)[1].

As the distance between the bubbles supporting cones is modulated, each monolayer experiences cycles of compression and stretching which in turn modulate its surface tension γ_i. We define the instantaneous deviation $\Delta\gamma_i$ to the equilibrium surface tension γ_0 such as $\gamma_i = \gamma_0 + \Delta\gamma_i$. In the limit of $\Delta\gamma_i \ll \gamma_0$, mechanical equilibrium at the intersecting line between the three interfaces imposes

$$\Delta\theta = \frac{1}{\gamma_0\sqrt{3}}(\Delta\gamma_1 + \Delta\gamma_2 - 2\Delta\gamma_3). \tag{9}$$

[1] The system is assumed to be symmetric with respect to the central film, which is the case in all experiments, so that the upper and lower monolayers have identical characteristics.

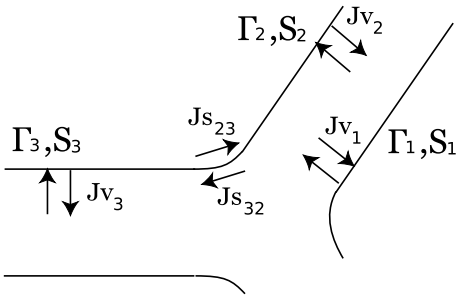

Fig. 11. In the case of a double bubble, one needs to consider 3 surfaces characterized by (S_i, γ_i). Each monolayer exchanges with the bulk solution with a flux Jv_i and with adjacent surface with a Marangoni flux Js_{ij}.

We now write the conservation of mass of surfactants for each monolayer in the form of

$$S\frac{\mathrm{d}\Gamma}{\mathrm{d}t} + \Gamma\frac{\mathrm{d}S}{\mathrm{d}t} = J_v + J_s\,, \tag{10}$$

where Γ is the surface concentration of the surfactant. The first flux J_v characterizes the exchange between the liquid phase and the interface while J_s corresponds to the exchange of surfactants between adjacent monolayers (Marangoni flow).

For a single oscillating bubble, J_v is the only relevent flux. The quantities γ_i and S_i are coupled through equation (8), and from equation (10), the volumic flow Jv can be expressed as a function of the dilational elastic module E^* through

$$Jv = S\frac{\mathrm{d}\Gamma}{\mathrm{d}t}\left(1 - \frac{E_0}{E^*}\right), \tag{11}$$

where

$$E_0 = -\mathrm{d}\gamma/\mathrm{d}\ln(\Gamma). \tag{12}$$

In the case of the double bubble, the transfer of surfactants between the monolayers 2 and 3 has to be taken into account through the flux J_s. One should in principle consider the concentration Γ_i as a continuously varying quantity. Here, we make the simplifying assumption that one can still consider that each monolayer can be characterized by a single surface tension and that the surface flux Js can be written as:

$$Js_{23} = -J_{32} = D_S\frac{\Gamma_2 - \Gamma_3}{L}2\pi r_c \tag{13}$$

where D_s is the surface diffusion coefficient of the surfactant and L a characteristic length of the order of the bubbles radius. From these two expressions, the mass conservation equation (10) for the three interfaces now reads

$$E_0 S_1\frac{\mathrm{d}\Gamma_1}{\mathrm{d}t} = -\Gamma_1 E^*\frac{\mathrm{d}S_1}{\mathrm{d}t}\,, \tag{14}$$

$$E_0 S_2\frac{\mathrm{d}\Gamma_2}{\mathrm{d}t} = -\Gamma_2 E^*\frac{\mathrm{d}S_2}{\mathrm{d}t} + E^* D_S\frac{\Gamma_3 - \Gamma_2}{L}2\pi r_c\,, \tag{15}$$

$$E_0 S_3\frac{\mathrm{d}\Gamma_3}{\mathrm{d}t} = -\Gamma_3 E^*\frac{\mathrm{d}S_3}{\mathrm{d}t} + E^* D_S\frac{\Gamma_2 - \Gamma_3}{L}2\pi r_c\,. \tag{16}$$

Using expression (12), this system of coupled equations (14, 15) and (16) can be solved to obtain an expression of the surface tension variations $\Delta\gamma_i$ as a function of the surface area variations $\Delta S_i/S_i$:

$$\Delta\gamma_1 = E^* \frac{\Delta S_1}{S_{10}}\,, \tag{17}$$

$$\Delta\gamma_2 = E^* \frac{iE_0\omega\tau}{E^* + iE_0\omega\tau} \frac{\Delta S_2}{S_{20}}\,, \tag{18}$$

$$\Delta\gamma_3 = E^* \frac{iE_0\omega\tau}{E^* + iE_0\omega\tau} \frac{\Delta S_3}{S_{30}}\,, \tag{19}$$

where τ is a characteristic time of surface tension equilibration between adjacent monolayers defined as

$$\tau^{-1} = 2\pi \frac{r_{c0}}{L} D_S \frac{S_{20} + S_{30}}{S_{20} S_{30}}\,. \tag{20}$$

Experimental measurements of the different surface areas as well the surface evolver simulations show that $S_1(t) + S_2(t)$ is a constant, equal to $2\pi R^2$ for initially hemispherical bubbles. The expression of the areas S_i and their variations ΔS_i are thus simply related, to first order, to the contact radius r_c and its variation Δr_c through the following relationships:

$$S_1 = S_2 = 2\pi R^2 - \pi r_c^2\,, \tag{21}$$

$$\Delta S_1 = \Delta S_2 = -2\pi \Delta r_c r_{c0}\,, \tag{22}$$

$$S_3 = \pi r_c^2\,, \tag{23}$$

$$\Delta S_3 = 2\pi \Delta r_c r_{c0}\,. \tag{24}$$

From this, and the expression of $\Delta\theta$ given by equation (9), one can deduce the angular complex modulus A^*:

$$A^* = \frac{2E^*}{\gamma_0\sqrt{3}} \left(\frac{iE_0\omega\tau}{E^* + iE_0\omega\tau} \frac{4R^2}{2R^2 - r_{c0}^2} + \frac{E^*}{E^* + iE_0\omega\tau} \frac{r_{c0}^2}{2R^2 - r_{c0}^2} \right). \tag{25}$$

Two limiting situations can be identified:

– When $\omega\tau \ll 1$, interfacial diffusion processes are instantaneous so that surface tension are immediately equilibrated between interfaces 2 and 3. In this limit, the interfaces can freely slide one over the other. Since $S_2 + S_3$ is constant, the contact angle deviations are only due to the external surface compression cycles as shown in Figure 12(a). The expression of the complex angular modulus reduces to

$$A_1^* = \frac{2E^*}{\gamma_0\sqrt{3}} \frac{r_{c0}^2}{2\pi R^2 - \pi r_{c0}^2}\,. \tag{26}$$

– When $\tau \gg 1$, Marangoni flows are negligible and the three double interfaces oscillates independently as shown in Figure 12(b). In this case the expression of the complex angular modulus reads

$$A_2^* = \frac{2E^*}{\gamma_0\sqrt{3}} \frac{4R^2}{2\pi R^2 - \pi r_{c0}^2}\,. \tag{27}$$

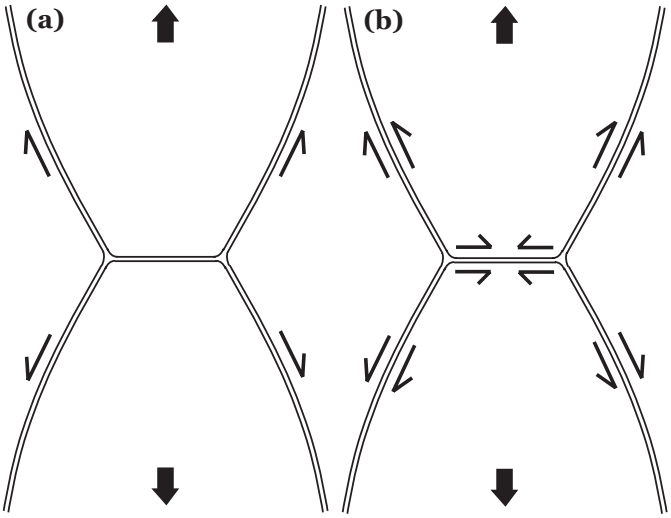

Fig. 12. Limiting models of compression/stretching of the monolayers for a double bubble submitted to an oscillating solicitation. (a) When $\omega\tau \ll 1$, surface diffusion processes are fast. Since the internal surface is constant, its surface tension of the internal film does not vary and the only contribution to the contact angle comes from the external monolayer. (b) When $\omega\tau \gg 1$, surface diffusion processes are slow. The surface tension is the same on either side of each film wich responds independently from each other.

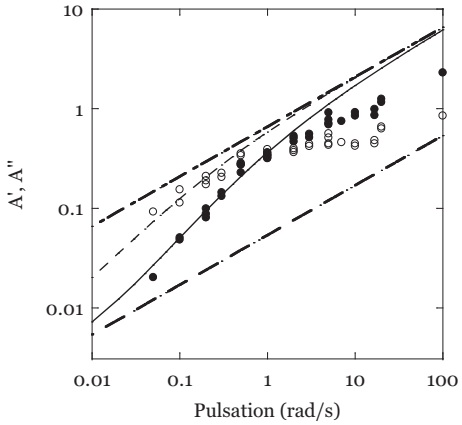

Fig. 13. Comparison of the experimental angular moduli A' (closed circles) and A'' (open circles) with the results of the double-bubble model adjusted with $\tau = 3 \cdot 10^{-4}$ s. The dashed lines represent the results corresponding to the sliding monolayers model, A_1' and A_2'' (dashed lines), and the independent films model, A_2' and A_2'' (dash-dotted lines).

Figure 13 shows the frequency diagram of A' and A'' and the two limiting predictions of A^* given by equations (26) and (27) using the Lucassen adjustement of E^*. Consistently, the experimental moduli lay within the limiting models over the whole range of frequency. The best fit of the data using equation (25) is also plotted which corresponds to a characteristic transition time $\tau = 3 \cdot 10^{-4}$ s. Although it compares correctly with the data at low frequency, significant deviation is observed at high frequency.

6 Application to a 2D model foam

In this part, the consequence of such dynamic effects on the bulk rheology of foams is discussed. We attempt to estimate how the angular measurements provided by the double-bubble set-up can be relevant to predict the contribution of the films (and Plateau borders) to the foam rheological properties. Such effects have been evidenced in macroscopic foam measurements [27]. Several models have been proposed to couple surface rheology to bulk foam mechanical response [4,30,31]. Here, our approach will be limited to a perturbative version of the Princen model.

This model pictures the foam as a 2D regular hexagonal lattice (Fig. 14(a)). Taking into account Plateau rule and the surface conservation of each cell, Princen derives the modification of lengths and orientations of the different films associated with an imposed quasistatic shear strain ϵ (Fig. 14(b)), from which he derives various mechanical quantities.

The angle Ψ of the initially vertical films as well as the film length variation dr can be expressed as a function of ϵ (see Fig. 14(b)):

$$\Psi = \frac{1}{2}\epsilon, \tag{28}$$

$$\frac{\mathrm{d}r}{r} = \frac{\sqrt{3}}{2}\epsilon. \tag{29}$$

The shear stress on a horizontal line (indicated in Fig. 14(b)) can be evaluated by considering that each film crossing this line carries a contribution $F = 2\gamma\sin(\Psi)$. Since the width of a unit cell is $r\sqrt{3}$, the stress σ is written as

$$\sigma = F = \frac{2\gamma}{r\sqrt{3}}\sin(\Psi) \approx \frac{2\gamma}{r\sqrt{3}}\Psi. \tag{30}$$

This allows one to write the shear modulus as

$$G_0 = \frac{\sigma}{2\epsilon} = \frac{1}{\sqrt{3}}\frac{\gamma}{r}\,. \tag{31}$$

The system is now submitted to an oscillating strain $\epsilon(t) = \epsilon_0\cos(\omega t)$. At finite oscillating frequency, one expects the Plateau rule no longer to be obeyed, and a correction $\Delta\theta_d(t)$ has to be added to the angle Ψ (see Fig. 15). By analogy with the double-bubble measurements, we define A' and A'' such as

$$\Delta\theta_d(t) = A'(\omega)\frac{\mathrm{d}r}{r}\cos(\omega t) + A''(\omega)\frac{\mathrm{d}r}{r}\sin(\omega t) \tag{32}$$

In the limit where the structure is weakly modified with regards to its equilibrium configuration (*i.e.* $\Delta\theta_d \ll \Psi$), the expression of dr/r provided by Princen (Eq. (29)) remains valid to the first order. Substituting ψ by $\psi + \Delta\theta_d$ in equation (30) yields a corrected foam modulus whose complex form now writes

$$G^* = G_0[1 + \sqrt{3}(A' + iA'')]. \tag{33}$$

It should be noticed that this result is independent of the physical origin of the viscoelastic process which sets

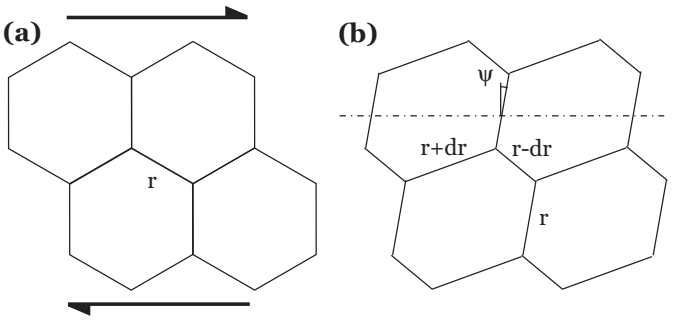

Fig. 14. The Princen model for the deformation of a 2D hexagonal foam. (a) Initial configuration. (b) After a small quasistatic deformation, the angles of the Plateau border remain equal to 120°. To the first order, the vertical films length remains unchanged but their orientation change by an angle Ψ. The other films length are modified by a quantity dr proportional to the applied strain.

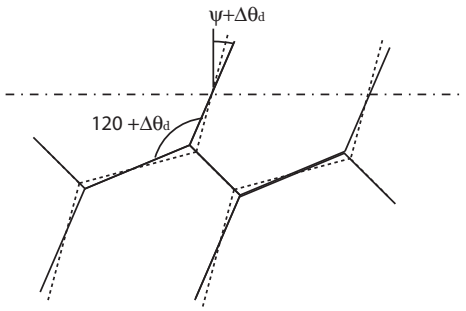

Fig. 15. Effect of the dynamic contact angle correction on the deformation of a 2D hexagonal structure. Contrary to the classical quasistatic deformation (dashed line), the angle of the central Plateau border is no longer 120°. This deviation induces an additional rotation of the vertical line of an angle equal to the dynamic correction $\Delta\theta_d$.

A' and A''. With the solution used in the present study, it appears that the viscoelastic behavior of the films is responsible for the observed deviation to Plateau rule. But one might expect for other systems that the dominating effect is the viscous dissipation localized in the Plateau border. Regardless of this underlying mechanism, the frequency diagram obtained by the double-bubble angular measurement directly provides the contribution of the film and Plateau border rheology to the foam modulus.

One limitation of this approach however needs to be underlined. The Princen model of foam elasticity is based on a perfectly regular network. In a real foam, r is largely distributed and one expects A' and A'' to depend on the relative lengths of the films connecting the given vertex. One is actually confronted with the same averaging problem when trying to evaluate the macroscopic modulus μ of a disordered film network. This structure parameter should control the prefactor of $A' + iA''$. But this limitation should still allow one to compare different systems (with different film rheological properties) provided that the foam structure is identical (same polydispersity).

7 Conclusion

A device has been developed to measure the contact angle between two soap bubbles in static and dynamic adhesion. This set-up allows us to confirm the existence of a negative line tension associated with the presence of a Plateau border at the intersection of three soap films: the static contact angle is systematically larger than 120° and the deviation amplitude can be quantitatively predicted given the central film radius and volume of the Plateau border. By varying the distance between bubbles, one can modulate the radius r_c of the central film. This induces a further deviation of the contact angle $\Delta\theta_d$ whose maximum value scales linearly with the amplitude of $\Delta r_c/r_c$. The amplitude and phase shift of $\Delta\theta_d$ with regards to $\Delta r_c/r_c$ has been systematically studied as a function of the modulation frequency.

The resulting phase diagram exhibits a transition from a viscous to an elastic regime with a crossover at a frequency of order $1\,\mathrm{rad}\cdot\mathrm{s}^{-1}$. This behavior of the double bubble cannot be deduced in a straightforward way from measurements of the film rheology obtained by single-oscillating-bubble measurements since exchanges can occur between adjacent surfaces. We constructed a model taking into account flows af surfactants from both the bulk phase and the adjacent surfaces for each monolayer. This leads to an expression of the angular module as a function of the dilational module and a characteristic time τ. Two limiting models correspond to extreme values of $\omega\tau$: the first one considers the three films in the double-bubble experiment as being independently stretched and overestimate the stored and dissipated energy in the oscillating experiment. The second one corresponds to the situation in which surfactant layers are free to slide over one another and underestimates the experimental measurements.

In order to test this hypothesis, we intend to modulate the rheological properties of the surfactant monolayer and the bulk solution. Surface shear viscosity can be increased by adding dodecanol in the solution. In contrast, the interstitial film can be rendered more viscous by increasing glycerol concentration or by adding soluble polymers such as PEO (polyethylene oxide).

We have illustrated the possibility to use these angular measurements as a way to predict the contribution of the films and vertices to macroscopic foam rheology. The proposed approach is based on a perturbative version of the Princen 2D regular foam model. It is therefore extremely naive and will need further work in order to be adapted to 3D foams and to take into account structural disorder. However, it suggests that this type of geometrical measurements might provide most of the relevant information. In particular, it integrates the different modes of energy dissipation, including the viscous drag associated with the Plateau borders motion. In order to test these ideas, such dynamical adhesion data need to be confronted to standard rheological measurements on 3D foams for various chemical solutions.

We woud like to thank K. Brakke for his help with surface evolver simulations as well as J.-F. Géminard, I. Cantat, S. Cohen-Addad and R. Höhler for fruitful discussions.

References

1. S.A. Khan, C.A. Schnepper, R.C. Armstrong, J. Rheol. **32**, 69 (1988).
2. D. Weaire, S. Hutzler, *The Physics of Foams* (Oxford University Press, New York, 1999).
3. R. Höhler, S. Cohen-Addad, J. Phys.: Condens. Matter **17**, R1041 (2005).
4. D. Buzza, C.Y. Lu, M. Cates, J. Phys. II **5**, 37 (1995).
5. L. Schwartz, H. Princen, J. Colloid Interface Sci. **118**, 201 (1987).
6. J. Lucassen, M. Van den Tempel, J. Colloid Interface Sci. **41**, 491 (1972).
7. J. Lucassen, M. Van den Tempel, Chem. Eng. Sci. **27**, 1283 (1972).
8. V. Bergeron, J. Phys.: Condens. Matter **11**, R215 (1999).
9. H. Fruhner, K.D. Wantke, Colloids Surf. A: Physicochem. Eng. Aspects **114**, 53 (1996).
10. H. Fruhner, K.D. Wantke, K. Lunkenheimer, Colloids Surf. A: Physicochem. Eng. Aspects **162**, 193 (1999).
11. K.D. Wantke, H. Fruhner, J. Colloid Interface Sci. **237**, 185 (2001).
12. P. Aussillous, D. Quéré, Europhys. Lett. **59**, 370 (2002).
13. I. Cantat, R. Delannay, Phys. Rev. E **67**, 031501 (2003).
14. N. Denkov, V. Subramanian, D. Gurovich, A. Lips, Colloids Surf. A: Physicochem. Eng. Aspects **263**, 129 (2005).
15. E. Terriac, J. Etrillard, I. Cantat, Europhys. Lett. **74**, 909 (2006).
16. M. Durand, H.A. Stone, Phys. Rev. Lett. **97**, 226101 (2006).
17. H.M. Princen, J. Colloid Interface Sci. **91**, 160 (1983).
18. J. Plateau, *Statique Expérimentale et Théorique des Liquides Soumis aux Seules Forces Moléculaires* (Clemm, Paris, 1873).
19. M. Fortes, M. Rosa, J. Colloid Interface Sci. **241**, 205 (2001).
20. J. Rodriguez, B. Saramago, M. Fortes, J. Colloid Interface Sci. **239**, 577 (2001).
21. J.C. Géminard, A. Zywocinski, F. Caillier, P. Oswald, Philos. Mag. Lett. **84**, 199 (2004).
22. M. Fortes, P. Teixeira, Philos. Mag. Lett. **85**, 21 (2005).
23. M. Fortes, P. Teixeira, Phys. Rev. E **71**, 051404 (2005).
24. A. Neimark, M. Vignes-Adler, Phys. Rev. E **51**, 788 (1995).
25. G. Han, A. Dussaud, B. Prunet-Foch, A. Neimark, M. Vignes-Adler, J. Non-Equilib. Thermodyn. **25**, 325 (2000).
26. K. Brakke, Exp. Math. **1**, 141 (1992).
27. S. Cohen-Addad, R. Höhler, Y. Khidas, Phys. Rev. Lett. **93**, 028302 (2004).
28. D. Langevin, Adv. Colloid Interface Sci. **88**, 209 (2000).
29. J. Lucassen, Faraday Discuss. Chem. Soc. **59**, 76 (1975).
30. D. Edwards, H. Brenner, D. Wasan, *Interfacial Transport Processes and Rheology* (Butterworth-Heinemann, 1991).
31. D. Stamenovic, J. Colloid Interface Sci. **145**, 255 (1991).

Résumé : Nous avons développé plusieurs expériences originales permettant de sonder les champs mécaniques à une interface frottante rugueuse. Nous avons montré qu'il était possible d'obtenir les champs de pression et de glissement interfaciaux à partir des images en lumière transmise de la zone de contact. Par ailleurs, nous avons intégré un micro-capteur de type MEMS (développé en collaboration avec le CEA-LETI à Grenoble) dans une membrane élastomère afin de mesurer directement le champ des contraintes immédiatement sous l'interface. Ces mesures ont permis d'identifier et d'interpréter des déviations aux modèles mécaniques classiques décrivant les champs de contraintes à une interface frottante.

Le frottement solide est un mécanisme qui met en jeu un large spectre d'échelles spatiales. Les contraintes macroscopiques sont contrôlées par la géométrie des objets en contact, tandis que les processus dissipatifs sont généralement confinés dans les toutes premières couches moléculaires en contact. Les échelles intermédiaires ne peuvent cependant être ignorées : en effet, la plupart des surfaces usuelles, même les plus finement usinées, présentent une rugosité aléatoire à l'échelle du micron. L'interface entre deux solides au contact n'est donc généralement pas homogène mais formée d'un grand nombre de micro-contacts isolés qui supportent l'ensemble de la charge appliquée entre les deux objets. Dans une approche mécanique de type milieu continu, une telle interface *multi-contacts* peut être décrite comme une fine couche d'un matériau composite intercalée entre les deux blocs solides. Cette couche possède des caractéristiques mécaniques contrôlées par les propriétés statistiques des micro-aspérités qui la composent, en particulier la distribution des hauteurs de leur sommet. Bien que d'épaisseur très faible (de l'ordre de la hauteur typique des aspérités, i.e. ~μm), son comportement mécanique est central pour la compréhension des contraintes s'établissant dans les deux objets en contact statique ou en frottement.

B) MESURE OPTIQUE DES CHAMPS DE CONTRAINTES ET DE DEPLACEMENT

Nous avons étudié les propriétés de ces couches en développant des mesures *in situ* fondées sur une observation optique de l'interface multi-contacts en lumière transmise. L'encart haut de la Figure 7 montre une image typique obtenue entre une lentille de verre sphérique et un bloc élastomère transparent dont la surface au contact est rugueuse. Les aspérités micrométriques diffusent la lumière et induisent sur toute l'image des modulations de l'intensité lumineuse transmise. Lorsque l'on déplace la sphère lisse à la surface du bloc rugueux, les micro-aspérités en contact sont d'abord entrainées par la sphère puis glissent à sa surface sans subir d'altération détectable. Nous les avons utilisées comme marqueurs de position pour mesurer, par vélocimétrie par corrélation d'images (CIV), le champ de déplacement dans le plan de l'interface[2]. Nous avons ainsi étudié la transition vers le glissement : dans la géométrie utilisée, celle-ci se produit par croissance d'une zone périphérique glissante qui coexiste avec une zone centrale circulaire collée (Figure 7), dont le rayon décroît et s'annule lorsqu'est atteinte la force seuil nécessaire au glissement macroscopique. Ces mesures de haute résolution spatiale, associées à l'utilisation d'un matériau relativement mou, ont également permis de caractériser la déformation élastique de la couche rugueuse avant la mise en glissement associée au fléchissement des aspérités individuelles. Nous avons ainsi pu évaluer un module de cisaillement effectif de cette couche, qui est environ 100 fois plus faible que celui du matériau massif.

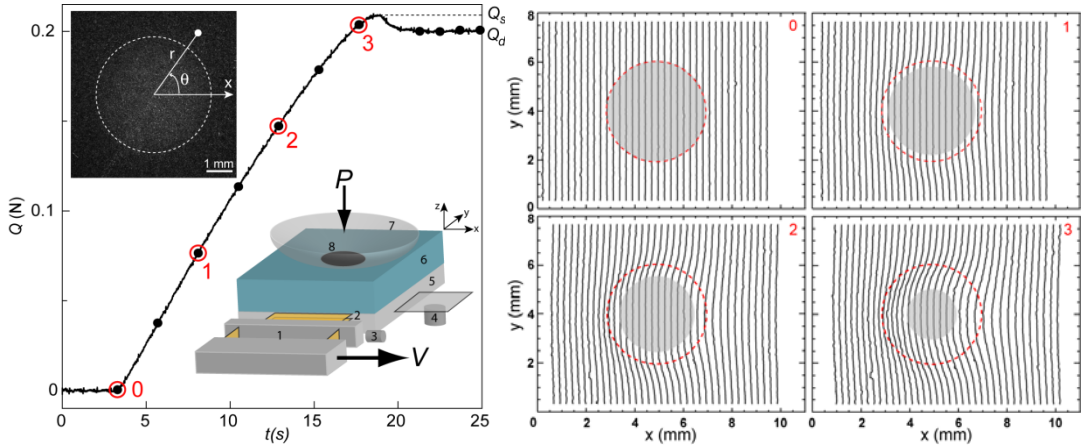

Figure 7: ***(Figure de gauche)*** *Encart bas : schéma du montage dédié à l'étude optique de l'interface entre un bloc élastomère de PDMS rugueux (6) et une lentille sphérique en verre (7). Le bloc est solidaire d'un support transparent (5) à travers lequel on éclaire le contact (8). Ce support est relié à une platine de translation par deux bilames (1 et 2) permettant de mesurer, à l'aide de capteurs de position (3 et 4), les charges normale* ***P*** *et tangentielle* ***Q*** *appliquées. Une platine, motorisée permet de déplacer à vitesse constante* ***V*** *le bloc. Courbe : Evolution typique de la charge tangentielle lors d'une expérience de mise en charge. Encart haut : Image de l'interface pour* ***P****=0.33 N. La ligne pointillée délimite la zone de contact.* ***(Figure de droite)*** *Champ des déplacements dans le plan de l'interface rugueuse, mesuré par corrélation d'images au cours d'une charge quasi-statique (****V****=4µm/s, charge* ***Q*** *~ 0.204 N correspondant aux 4 cercles rouges sur la courbe de charge). Les déplacements sont représentés par la déformation de lignes initialement rectilignes verticales. Ces mesures mettent en évidence au sein du contact (frontière en pointillés rouge) la coexistence d'une région centrale collée (déplacement nul, représentée par la zone grisée) et d'une région périphérique de micro-glissement. Les déplacements sont multipliés par 30 pour être visibles.*

B) MESURES LOCALES DE FORCES SOUS UN CONTACT SOLIDE

Dans un contact rugueux macroscopique, l'interface apparaît donc comme l'élément le plus déformable, à la fois en compression et en cisaillement. Par rapport à une interface lisse, la rugosité modifie significativement les conditions aux limites mécaniques qui contrôlent la distribution des contraintes dans le volume des solides en regard. Pour mesurer directement ces contraintes, nous avons noyé un micro-capteur de force dans le bloc élastique rugueux. Ce micro-capteur de type MEMS (Micro-Electro Mechanical System) nous a été fourni par le CEA-LETI (Grenoble); il est constitué d'une membrane de silicium circulaire suspendue sur son périmètre et surmontée en son centre d'une tige rigide cylindrique (Figure 8A). Lorsqu'une force est exercée sur la tige, les déformations induites dans la membrane sont mesurées à l'aide de jauges piezo-résistives. Il permet ainsi de mesurer les trois composantes de la force locale dans une région d'extension millimétrique. Nous avons utilisé ce dispositif pour étudier les champs de contraintes à la base d'un film élastomère rugueux en contact statique ou dynamique.

Sous force normale, nous avons observé des écarts significatifs aux profils prédits par la loi d'Amontons Coulomb et calculés numériquement par éléments finis[3]. Cette loi stipule qu'un glissement irréversible doit se produire dès lors que le rapport entre la contrainte tangentielle et normale excède un coefficient de frottement supposé uniforme. Ces déviations, observées pour des couches rugueuses de très faible épaisseur, est d'autant plus importante que la charge imposée est faible. Ce résultat a pu être interprété en prenant en compte la compliance finie de la couche rugueuse.

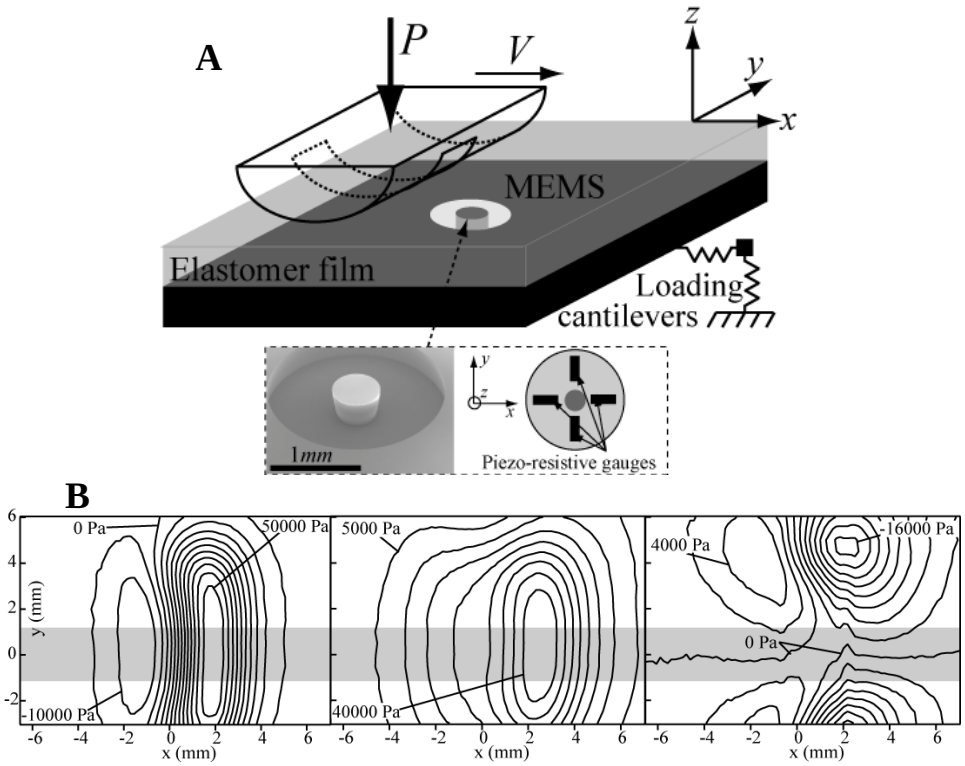

Figure 8 : (A) Schéma du montage permettant la mesure du champ des contraintes à la base d'un film élastomère rugueux d'épaisseur 2mm en régime de glissement stationnaire. Un indenteur cylindrique est déplacé à vitesse constante V et charge normale constante P à la surface du film. Un capteur de force est présent à la base de ce film (encart) : ce dernier consiste en une tige enfichée dans une membrane en silicium. Les contraintes subies par la membrane sont mesurées à l'aide de jauges piezo-résistives et permettent de mesurer les forces appliquées à la tige. (B) Champ des contraintes mesurées en régime de glissement stationnaire (de gauche à droite : contrainte normale, contrainte tangentielle dans la direction du glissement, contrainte tangentielle transverse).

Des mesures effectuées en régime de glissement stationnaire (Figure 8) ont permis de tester, pour la première fois de façon directe, certains modèles classiques décrivant les champs de contraintes et de glissement à une interface frottante[4]. Ces expériences ont été réalisées en géométrie cylindre/plan afin de permettre notamment une comparaison avec un modèle semi-analytique de frottement bidimensionnel développé par E. Katzav et M. Adda Bedia au laboratoire. Les écarts entre les profils de contraintes prédits par ce modèle et nos observations expérimentales sont limités mais significatifs. Là encore, ces écarts peuvent être attribués à la compliance de la couche rugueuse mais aussi à la dépendance en pression du coefficient de frottement dynamique, deux effets non pris en compte dans le modèle.

Références :

1. Optical measurement of the pressure at a multicontact interface, Julien Scheibert, Alexis Prevost, and Georges Debrégeas (en preparation)
2. Micro-slip field at a rough contact driven towards macroscopic sliding, Julien Scheibert, Georges Debregeas, Alexis Prevost (soumis)
3. Stress Field at a Sliding Frictional Contact: Experiments and Calculations, J. Scheibert, E. Katzav, M. Adda-Bedia, A. Prevost et G. Debrégeas, *J. Mech. Phys. Solids*, **57**, 1921-1933 (2009)
4. Experimental Evidence of Non-Amontons Behaviour at a Multi-contact Interface, J. Scheibert, A. Prevost, J. Frelat, P. Rey and G. Debrégeas, *Europhys. Lett.* 83, 34003 (2008)

A Letters Journal Exploring the Frontiers of Physics

August 2008

EPL, **83** (2008) 34003
doi: 10.1209/0295-5075/83/34003

www.epljournal.org

Experimental evidence of non-Amontons behaviour at a multi-contact interface

J. Scheibert[1(a)], A. Prevost[1], J. Frelat[2], P. Rey[3] and G. Debrégeas[1]

[1] *Laboratoire de Physique Statistique de l'ENS, UMR 8550, CNRS/ENS/Université Paris 6/Université Paris 7 24 rue Lhomond, F-75231 Paris, France, EU*
[2] *Laboratoire de Modélisation en Mécanique, UMR 7607, CNRS/Université Paris 6 4 place Jussieu, F-75252 Paris, France, EU*
[3] *CEA-LETI - 17 rue des Martyrs, F-38054 Grenoble Cedex 09, France, EU*

received 21 January 2008; accepted in final form 16 June 2008
published online 23 July 2008

PACS 46.55.+d – Tribology and mechanical contacts
PACS 81.40.Pq – Friction, lubrication, and wear
PACS 85.85.+j – Micro- and nano-electromechanical systems (MEMS/NEMS) and devices

Abstract – We report on normal stress field measurements at the multicontact interface between a rough elastomeric film and a smooth glass sphere under normal load, using an original MEMS-based stress-sensing device. These measurements are compared to Finite-Elements Method (FEM) calculations with boundary conditions obeying locally Amontons' rigid-plastic–like friction law with a uniform friction coefficient. In dry contact conditions, significant deviations are observed which decrease with increasing load. In lubricated conditions, the measured profile recovers almost perfectly the predicted profile. These results are interpreted as a consequence of the finite compliance of the multicontact interface, a mechanism which is not taken into account in Amontons' law.

Copyright © EPLA, 2008

Knowledge of the stress field at the contact region between two solids is of considerable interest to numerous domains such as mechanical engineering [1–6], solid friction [7–9] or seismology [10]. From a continuum mechanics point of view, the theoretical or numerical determination of this field requires a set of constitutive equations characterizing the mechanical response of the interface. These are usually inferred from macroscopic measurements: for instance, frictional contacts are often found to obey the empirical Amontons' friction law which states that irreversible sliding occurs when the ratio of tangential to normal forces reaches a static friction coefficient μ_{macro} without any prior deformation of the interface [11,12]. The classical approach for calculating frictional contact stress field therefore consists in considering a smooth interface exhibiting an analog rigid-plastic response: μ_{macro} now defines the threshold ratio between shear and normal stress components for local slip to occur [5,7–9].

Considering both a smooth interface and Amontons' law may seem paradoxical, since the latter is expected to be valid only for rough solids. Because of adhesion forces, contact between molecularly smooth surfaces generally do not obey Amontons' friction law [13,14]. Furthermore, random roughness provides a microscopic basis to Amontons' law [15–18]: it allows for the description of the interface as a collection of isolated load-bearing points forming a multicontact interface (MCI). For standard roughness characteristics, the real area of contact —and thus the tangential force required to trigger sliding— grows linearly with the applied load.

When associated with Amontons' law, the smooth-interface hypothesis must therefore be understood as the limiting case of a macroscopic surface bearing vanishingly small roughness. One may wonder to what extent this approximation is valid in real MCI's. Experimentally, this question has been addressed by focusing on the relationship between the macroscopic normal load and the indentation depth [17,19–21]. Here we go further and compare the stress field measured within an extended MCI with Finite-Elements Method (FEM) calculations assuming both smooth surfaces and the local (rigid-plastic) Amontons' law.

In order to perform such local measurements, we take advantage of the recent development of Micro Electro

(a) E-mail: julien.scheibert@lps.ens.fr

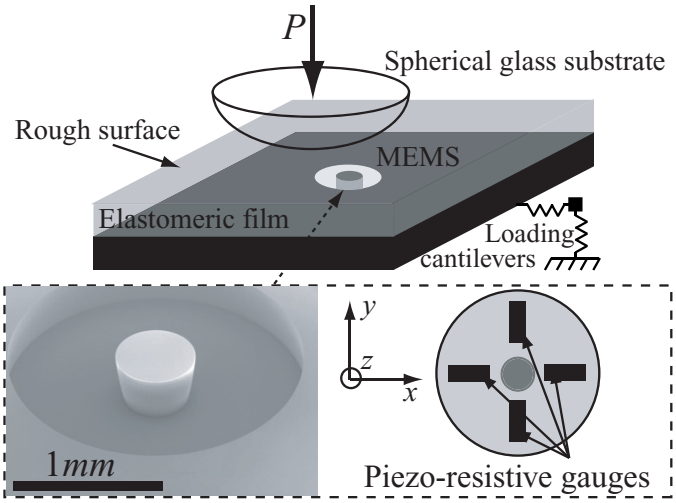

Fig. 1: Schematics of the stress sensor. A MEMS force sensor enables to measure the applied normal stress at the base of a rough, nominally flat PDMS film (thickness $h = 2\,\mathrm{mm}$, lateral dimensions $50 \times 50\,\mathrm{mm}$) pressed against a spherical glass substrate. The macroscopic normal and tangential loads are measured through the extension of two orthogonal loading cantilevers (normal stiffness $641 \pm 5\,\mathrm{Nm}^{-1}$, tangential stiffness $51100 \pm 700\,\mathrm{Nm}^{-1}$) by capacitive position sensors (respectively, MCC30 and MCC5, Fogale nanotech).

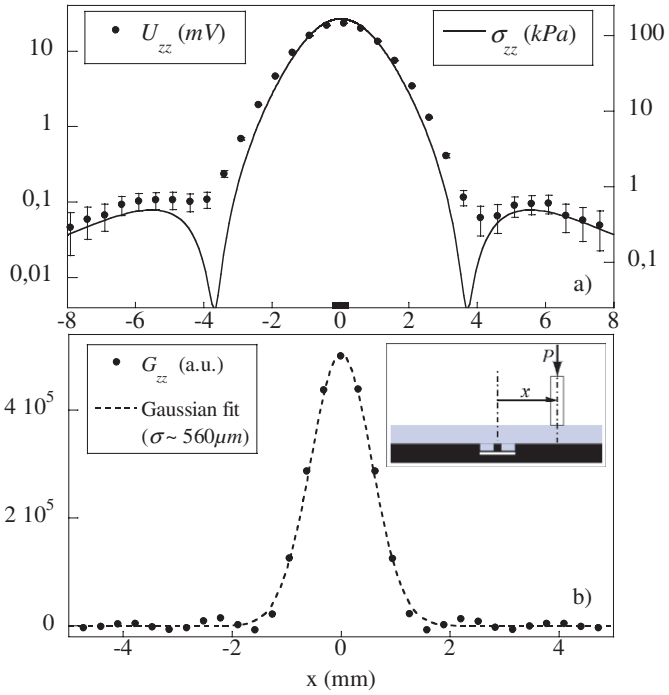

Fig. 2: a) Radial profiles associated to the indentation of the elastic film by a rigid thin rod, under normal load $P = 1\,\mathrm{N}$. The measured output voltage U_{zz} (•) is compared to FEM results (solid line) for the normal stress σ_{zz} at the base of the elastic film. The error bars represent the electronic noise. The black rectangular patch represents the rod diameter ($500\,\mu\mathrm{m}$). b) Normalized apparatus function of the MEMS for the normal stress, G_{zz} (•), as determined by numerical integration of eq. (1) and its Gaussian fit in dashed line.

Mechanical Systems (MEMS) [22,23]. Local normal stress measurements are obtained using a MEMS force sensor[1] embedded at the rigid base of a rough, nominally flat elastomeric film pressed against a rigid sphere under normal load (fig. 1). The MEMS sensitive part is a rigid cylinder (diameter $550\,\mu\mathrm{m}$, length $475\,\mu\mathrm{m}$) attached to a suspended circular Silicon membrane (radius 1 mm, thickness $100\,\mu\mathrm{m}$) whose deformations are measured with four couples of piezo-resistive gauges (see inset of fig. 1). The applied normal stress is therefore averaged over a surface of a few millimeters square.

The elastomeric material is a cross-linked polydimethylsiloxane (PDMS) (Sylgard 184, Dow Corning) of Young's modulus $2.2 \pm 0.1\,\mathrm{MPa}$, and of Poisson ratio 0.5 [25]. No measurable stress relaxation being observed after a sudden loading, the PDMS can be considered as purely elastic. The film is obtained by pouring the cross-linker/PDMS melt on the MEMS into a parallelepipedic mold covered with a PolyMethylMethAcrylate plate roughened by abrasion with an aqueous solution of Silicon Carbide powder (mean diameter of the grains $37\,\mu\mathrm{m}$). After curing and demoulding, the resulting rms surface roughness is measured with an interferential profilometer (M3D, Fogale Nanotech) to be $\rho = 1.82 \pm 0.10\,\mu\mathrm{m}$. This roughness is sufficient to avoid any measurable pull-off force against smooth glass substrates, as discussed in [26].

The stress sensing device is calibrated by indenting the film surface with a rigid rod of diameter $500\,\mu\mathrm{m}$, under a normal load P. With this type of indentor, the sensor output is found to be linear with the applied load. By successively varying the position of the rod along the x-direction, and assuming homogeneity of the surface properties of the film, one can construct point by point the normal output voltage radial profile U_{zz} (fig. 2a)). The latter is then compared to the results of Finite-Elements Method (FEM, Software Castem 2007) calculations for the stress σ_{zz} at the base of a smooth axi-symmetrical elastic film (of same elastic moduli and thickness) perfectly adhering to its rigid base and submitted to a prescribed normal displacement over a central circular area[2] of diameter $500\,\mu\mathrm{m}$. As expected for contact regions of dimensions smaller than the film thickness, the stress calculated at the base of the film is found to be insensitive to the frictional boundary conditions.

Ignoring the stress field modifications induced by the MEMS 3D structure, one can relate the measured output voltage U_{zz} to the stress field σ_{zz} by writing down that

$$U_{zz}(x, y) = A_{zz} G_{zz} \otimes \sigma_{zz}(x, y), \qquad (1)$$

[1] This MEMS also measures the tangential stress, but with an accuracy which is not sufficient for the present study [24].

[2] Such results could have been obtained semi-analytically for frictionless conditions by using the model developed in [27] but FEM calculations have been preferred here because they allow for variable boundary conditions.

where A_{zz} is a conversion constant (expressed in mV/Pa), G_{zz} is a normalized apparatus function and $\otimes$ is a convolution product. In Fourier space, eq. (1) becomes

$$A_{zz}G_{zz}(x,y) = \mathcal{F}^{-1}\left(\frac{\mathcal{F}\{U_{zz}\}(f_x,f_y)}{\mathcal{F}\{\sigma_{zz}\}(f_x,f_y)}\right)(x,y), \qquad (2)$$

where $\mathcal{F}$ is the bidimensional spatial Fourier transform, $\mathcal{F}^{-1}$ its inverse, and where f_x, f_y are, respectively, the spatial frequencies in the x, y directions. The $U_{zz}(x,y)$ and $\sigma_{zz}(x,y)$ fields are built from the profiles along the x-axis, assuming axisymmetry, and then transformed using the Fast Fourier Transform (FFT) algorithm. The fast decaying of $\mathcal{F}\{\sigma_{zz}\}$ with increasing spatial frequency introduces divergences of the ratio in eq. (2) To avoid it, a white noise of amplitude ten times weaker than the weakest relevant spectral component is added to both terms of the ratio before applying the FFT. The result is found to be insensitive to the particular amplitude of this white noise. A_{zz} is determined so that the integral of G_{zz} is 1.

Figure 2b) shows the resulting apparatus function. It has a bell shape with typical width of the order of 600 μm comparable to the MEMS lateral dimension. For the subsequent convolutions an approximated apparatus function, taken as a Gaussian of standard deviation 561 μm (fig. 2b)), has been used. This approximated apparatus function gives back the measured profile when convoluted by the calculated one, proving that neither the deconvolution method nor the approximation introduces significant loss of information. In particular, the point-like indentation involves a large enough spatial spectrum to allow for a faithfull determination of G_{zz} within all of its relevant spatial components.

Sphere-on-plane MCIs are formed against an optical plano-convex spherical glass lens (radius of curvature 128.8 mm). Both the glass and PDMS surfaces are passivated using a vapor-phase silanization procedure which lowers and homogenizes the surface energy. Each contact is obtained using the following loading sequence. The glass lens is pressed against the film up to the prescribed load P within 2% relative error. Due to this loading, the extremity of the normal cantilever is tangentially displaced and a significant tangential load Q is induced. Consequently, from this position, the contact is renewed by manual separation which results in a much smaller but finite Q. The glass lens is eventually translated a few micrometers tangentially down to $Q = 0$. Both the surface treatment and the loading sequence are found to yield an excellent reproducibility of the measurements. As for the rod indentation, the radial profiles are derived from a series of 33 contacts whose centers lie every 0.5 mm along the x-direction. These profiles divided by A_{zz} have the dimension of a stress and are labelled S_{zz}.

For a quantitative comparison, FEM calculations are carried out for a frictional sphere-on-plane contact with the same geometry. Both contacting surfaces are taken as smooth and the interface is assumed to obey locally

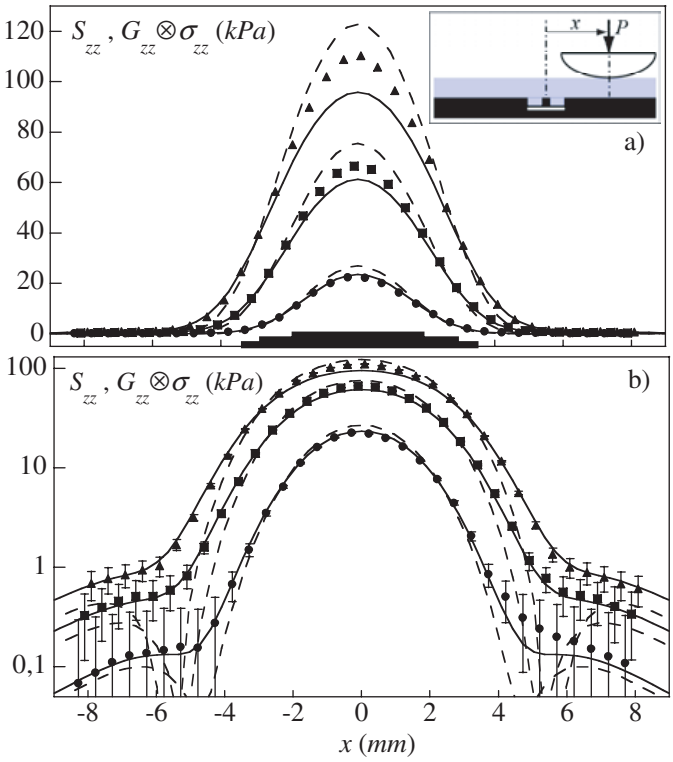

Fig. 3: Measured normal stress profiles (S_{zz}) under normal loading by a rigid sphere ($P = 0.34$ N (•), 1.37 N (■), 2.75 N (▲)). Comparison is made with $G_{zz} \otimes \sigma_{zz}$ for $\mu = 0$ (solid lines, indentation depths 18, 33 and 45 μm, respectively) and $\mu = \infty$ (dashed lines, indentation depths 16, 28 and 37 μm, respectively). a) Linear scale. b) Semi-logarithmic scale. The black rectangular patches on a) represent the contact diameters (2.00, 2.90 and 3.45 mm for $P = 0.34$, 1.37 and 2.75 N, respectively) obtained from the FEM calculations for $\mu = 0$.

Amontons' friction law with a friction coefficient μ. Both solids are discretized with a uniform mesh size of 50 μm and the normal displacement of the rigid elastic sphere is prescribed. The contact conditions are satisfied using a double Lagrange multiplier implying that both surfaces are slave and master. The normal load is reached step-by-step and at each step an iterative Newton-Raphson method is used to satisfy both the unilateral contact and the friction law.

Figure 3 compares the S_{zz} and $G_{zz} \otimes \sigma_{zz}$ profiles for two limiting boundary conditions, $\mu = 0$ and $\mu = \infty$, and for three values of P. Within the error bar the measured profiles are bracketed by the two limiting numerical profiles over the whole spatial range and over 3 orders of magnitude, as clearly displayed on fig. 3b). In the contact outer region, S_{zz} is systematically very close to the frictionless profile whereas at the center it increasingly departs from it with the load, as discussed further. Similar measurements are performed, for two limiting loads ($P =$ 0.69 N and $P = 2.75$ N), under lubricated conditions. A glycerol droplet is inserted at the interface prior to loading. The profiles display both a larger spatial extent and a

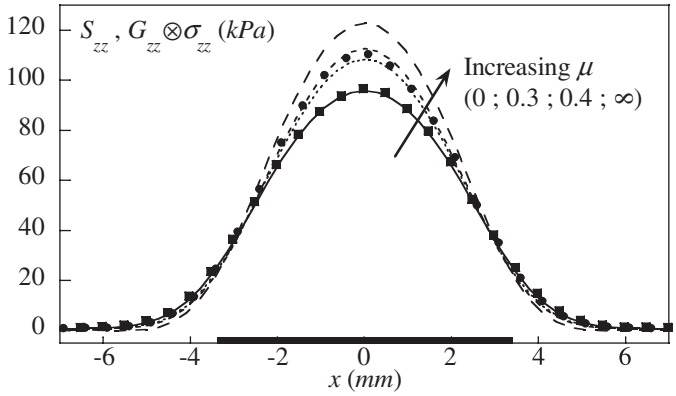

Fig. 4: Measured normal stress profile (S_{zz}) under normal loading ($P = 2.75\,\mathrm{N}$) by a rigid sphere for both dry (•) and glycerol-lubricated (■) contacts. Shown in solid and dashed lines are the $G_{zz} \otimes \sigma_{zz}$ profiles for 4 values of μ (0, 0.3, 0.4, ∞). The black rectangular patch represents the contact diameter (3.45 mm) obtained from the FEM calculation for $\mu = 0$ (indentation depth 45 μm).

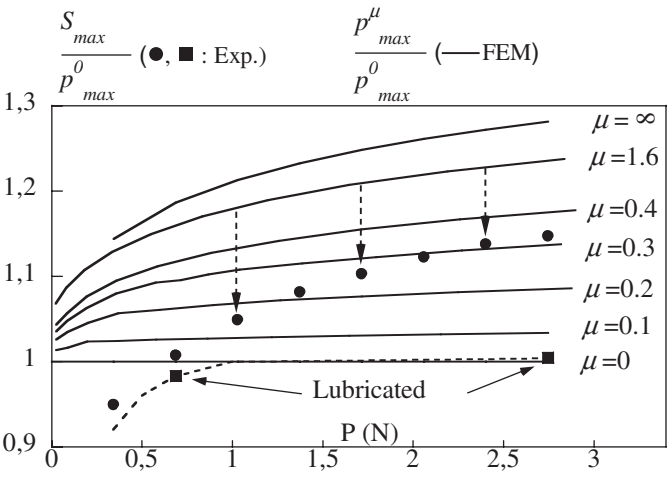

Fig. 5: Load dependence of S_{max}, the maximum normal stress measured for dry (•) and lubricated (■, guideline in dashed line) conditions, and p^μ_{max}, the maximum calculated normal stress for various values of μ. Both quantities have been normalized by p^0_{max}, the value of p^μ_{max} for $\mu = 0$. The vertical arrows represent the apparent drop of the friction coefficient from $\mu_{macro} \sim 1.6$ down to μ_e for dry conditions.

lower maximum amplitude than the ones obtained with dry conditions. They are correctly captured by the FEM calculation using a null friction coefficient (as shown for $P = 2.75\,\mathrm{N}$ in fig. 4).

Except for the smallest load, any pressure profile under dry conditions can be correctly approached using an effective friction coefficient μ_e which can be determined by trial and error with a resolution of order 0.1 (as illustrated in fig. 4). The load dependence of μ_e is exhibited by plotting the maximum pressure S_{max} normalized by the maximum pressure p^0_{max} calculated for a frictionless contact, for different loads. On the same graph, we plot the equivalent expression p^μ_{max}/p^0_{max} obtained by FEM calculation for different friction coefficients μ in the range $[0, \infty]$. This representation allows one to directly *read* the value of the effective friction coefficient μ_e for any load. μ_e is found to increase with P but remains well below the macroscopic friction coefficient $\mu_{macro} \approx 1.6$ over the range of loads explored[3].

The significant discrepancy between the effective and the macroscopic friction coefficient suggests that the rigid-plastic response of the interface underlying Amontons' law needs to be refined. One may in particular question the rigid hypothesis since MCIs are known to possess finite compliances both in normal and in-plane directions. The effect of the normal compressibility of a rough interface [16,17,21,29] on a sphere-on-plane contact has first been described by Greenwood and Tripp [30]. They predict an increase of the apparent contact radius with respect to a smooth interface, as well as a decrease in the maximum normal stress. These deviations are expected to vanish when the ratio of the *rms* surface roughness ρ to the indentation depth becomes small. The effect of the MCI tangential compliance has been recently probed experimentally [31,32]: a global reversible deformation of the interface between two contacting solids is measured before irreversible slippage occurs; regardless of the normal load, the maximum shear deformation of the interface before slippage is of the order of its *rms* roughness ρ.

In the present set of experiments, these two effects can be uncoupled since the tangential stress at the interface vanishes under lubricated conditions. The fact that the lubricated profiles (■ in fig. 5) are compatible with those calculated for a frictionless contact suggests that the MCI normal compressibility effect is negligible in most of the load range explored (typically for $P \gtrsim 1\,\mathrm{N}$). Still, it is probably responsible for the fact that S_{max}/p^0_{max} falls below 1 for the smallest loads when the indentation depth becomes comparable to the thickness ρ of the rough layer.

The tangential compliance of the interface is thus expected to be primarily responsible for the observed drop from μ_{macro} to μ_e for dry contacts. This effect can be qualitatively understood by first considering the case of an interface with infinite friction. The normal loading of a sphere-on-plane contact yields a divergence of the shear stress at the edge of the contact region [5,6]. In a system with finite friction, this stress is relaxed by the development of a slip annulus at the periphery of the contact region which coexists with a central (circular) stick region, as discussed by Spence [5] and observed in our FEM calculations. The radius of the stick region is a growing function of the friction coefficient. As compared to a rigid interface, the existence of a finite tangential compliance allows for

[3]The macroscopic friction coefficient has been measured for a driving velocity $v = 100\,\mu$m/s of the rigid base of the sensor: it shows a (small) decrease from 1.8 to 1.5 as the load is increased from 0.34 N to 2.75 N, a behavior usually attributed to the finite adhesion energy of the interface [28].

a subsequent strain relaxation at the elastomeric surface which is qualitatively equivalent to reducing the value of the apparent friction coefficient. This effect should vanish as the ratio of the tangential displacement induced by the sphere-on-plane loading becomes larger than the maximum elastic displacement ρ allowed by the MCI deformation. The effective friction coefficient is thus expected to asymptotically reach μ_{macro} as the load P is increased in qualitative agreement with our observations (fig. 5). It is noticeable however that the reduction of the apparent friction coefficient remains significant even for loads associated with a normal displacement of the rigid substrate more than 20 times larger than the interface thickness ρ.

The results reported in this letter provide evidence for the inadequacy of local Amontons' friction law to correctly capture sphere-on-plane MCI pressure profiles. They provide the first quantitative experimental measurements of such stress fields over a large range of loads for both lubricated and frictional contacts. It appears that each profile can be correctly described within the scope of Amontons' rigid-plastic law, but with a load-dependent effective friction coefficient. This coefficient grows with the total applied load but remains much smaller than the macroscopic friction coefficient even when the standard smooth hypothesis criterion (*rms* surface roughness much smaller than the indentation depth) is reached. By comparing lubricated and dry frictional contacts, we can separate the effects of normal and tangential compliance of the MCI and conclude that the latter is primarily responsible for the observed deviation to the local Amontons' law.

More generally, this study provides experimental support to previous works aiming at taking into account the rheological behaviour of the micro-contacts population in the mechanical studies of multicontact interfaces under tangential load [33–35]. From the present results we suggest that it should also be done for contacts under purely normal load. A first step could be the use of an elasto-plastic–like friction law instead of the classical rigid-plastic–like Amontons's one. These results were obtained with an original MEMS-based stress sensor, which has proven to be well-suited for the study of stress fields in centimeter-sized contacts and could be used to test directly any other mechanical model of the frictional interface. Many other aspects of contact mechanics are likely to be probed with the same method, such as the dynamical frictional regimes or the history-dependence of a contact submitted to an oscillatory tangential load below the sliding threshold. Other domains such as rheology or adhesion, where accurate spatially resolved stress measurements at interfaces are needed, could also benefit from the approach described here.

* * *

The authors thank A. Ponton and B. Ladoux for their help in the measurement of the PDMS Young's modulus and A. Chateauminois and C. Frétigny for fruitful discussions.

REFERENCES

[1] Hertz H., *Miscellaneous Papers* (Macmillan) 1896.
[2] Johnson K. L., *Br. J. Appl. Phys.*, **9** (1958) 199.
[3] Meijers P., *Appl. Sci. Res.*, **18** (1968) 353.
[4] Hardy C., Baronet C. N. and Tordion G. V., *Int. J. Numer. Methods Eng.*, **3** (1971) 451.
[5] Spence D. A., *J. Elasticity*, **5** (1975) 297.
[6] Johnson K. L., *Contact Mechanics* (Cambridge University Press) 1985.
[7] Cattaneo C., *Rend. Accad. Naz. Lincei*, **27** (1938) 214.
[8] Mindlin R. D., *Trans. ASME E, J. Appl. Mech.*, **16** (1949) 259.
[9] Hamilton G. M., *Proc. Inst. Mech. Eng. C - J. Mech. Eng. Sci.*, **197** (1983) 53.
[10] Scholtz C., *The Mechanics of Earthquakes and Faulting* (Cambridge University Press) 1990.
[11] Baumberger T. and Caroli C., *Adv. Phys.*, **55** (2006) 279, and references therein.
[12] Drees D. and Achanta S., *Proceedings of the ASME/STLE International Joint Tribology Conference, PTS A and B,* 2008, pp. 777–779.
[13] Vorvolakos K. and Chaudhury M., *Langmuir*, **19** (2003) 6778.
[14] Bureau L., Baumberger T. and Caroli C., *Eur. Phys. J. E*, **19** (2006) 163.
[15] Bowden F. and Tabor D., *The Friction and Lubrication of Solids* (Oxford University Press) 1950.
[16] Greenwood J. A. and Williamson J. B. P., *Proc. R. Soc. London, Ser. A*, **295** (1966) 300.
[17] Brown S. and Scholz C., *J. Geophys. Res.*, **90** (1985) 5531.
[18] Persson B. N. J., *J. Chem. Phys.*, **115** (2001) 3840.
[19] Nuri K. A., *Wear*, **30** (1974) 321.
[20] Kagami J., Yamada K. and Hatazawa T., *Wear*, **87** (1983) 93.
[21] Benz M., Rosenberg K., Kramer E. and Israelachvili J., *J. Phys. Chem. B*, **110** (2006) 11884.
[22] Kane B. J., Cutkosky M. R. and Kovacs G. T., *Sens. Actuators A: Phys.*, **54** (1996) 511.
[23] Leineweber M., Pelz G., Schmidt M., Kappert H. and Zimmer G., *Sens. Actuators A: Phys.*, **84** (2000) 236.
[24] Scheibert J., *Mécanique du contact aux échelles mésoscopiques* (Edilivre Collection Universitaire) 2008.
[25] Mark J. E. (Editor), *Polymer Data handbook* (Oxford University Press) 1999.
[26] Fuller K. N. G. and Tabor D., *Proc. R. Soc. London, Ser. A*, **345** (1975) 327.
[27] Fretigny C. and Chateauminois A., *J. Phys. D: Appl. Phys.*, **40** (2007) 5418.
[28] Carbone G. and Mangialardi L., *J. Mech. Phys. Solids*, **52** (2004) 1267.
[29] Persson B. N. J., *Phys. Rev. Lett.*, **99** (2007) 125502.
[30] Greenwood J. A. and Tripp J. H., *Trans. ASME E, J. Appl. Mech.*, **34** (1967) 153.
[31] Berthoud P. and Baumberger T., *Proc. R. Soc. London, Ser. A*, **454** (1998) 1615.

[32] Bureau L., Caroli C. and Baumberger T., *Proc. R. Soc. London, Ser. A*, **459** (2003) 2787.
[33] Tworzydlo W. W., Cecot W., Oden J. T. and Yew C. H., *Wear.*, **220** (1998) 113, and references therein.
[34] Sellgren U. and Olofsson U., *Comput. Methods Appl. Mech. Eng.*, **170** (1999) 65.
[35] Cochard A., Bureau L. and Baumberger T., *Trans. ASME E, J. Appl.Mech.*, **70** (2003) 220.

Micro-slip field at a rough contact driven towards macroscopic sliding (PREPRINT)

J. Scheibert, G. Debrégeas, A. Prevost*
Laboratoire de Physique Statistique de l'ENS, UMR 8550,
CNRS-ENS-Universités Paris 6 and 7, 24 rue Lhomond F-75231 Paris, France
(Dated: December 28, 2009)

The incipient sliding of a multicontact interface between a smooth glass sphere and a rough elastomer block is studied using an image correlation velocimetry technique. The displacement field of the elastomer's surface is measured both inside and outside the apparent contact region with a submicrometer displacement resolution. For a given shear load, a coexistence between an inner stick region surrounded by an outer slip annulus is observed. The stick region extension decreases with increasing load and eventually vanishes at the sliding threshold. These measurements allow for the first quantitative test of Cattaneo and Mindlin (CM) classical model of the incipient sliding of a smooth interface. Small deviations are observed and interpreted as a result of the finite compliance of the rough interface, a behavior which contrasts with Amontons' law of friction assumed to be valid locally in CM's model. We illustrate how these measurements actually provide a method for probing the rheology of the rough interface, which we find to be of the elasto-plastic type.

PACS numbers: 46.55.+d, 61.41.+e, 62.20.Qp, 68.35.Ct
Keywords: Contact mechanics, friction law, incipient sliding, micro-slip, image correlation velocimetry technique, multicontact, interfacial rheology

Amontons' law of friction states that the shear force required to trigger relative sliding between two solids in contact is proportional to the applied load normal to the interface. However, it is known that even for minute shear forces, well before macroscopic sliding settles in, micro-slip occurs within the contact. Slip bearing regions are thus expected to coexist with adhesive ones and to progressively invade the contact as the shear force approaches the sliding threshold. Providing a proper local description of this incipient sliding regime remains challenging despite its importance to the fields of tribology [1], earthquakes nucleation [2] or mechanical engineering [3, 4]. In the case of spherical contacts between elastic bodies (Hertz contact), an analytical solution to this problem is given by Cattaneo and Mindlin's (CM) procedure which has now become a classical model for shear loaded frictional contacts below the sliding threshold. It predicts that the stick region is a central disk whose radius continuously decreases from the apparent contact zone radius down to zero upon increasing shear loading [5, 6]. Experimental confirmation of CM's predictions has been obtained only indirectly by measuring macroscopic force-displacement curves or by observing the fretting zone resulting from the interfacial micro-slip [7].

In CM's approach, the interface is assumed to be smooth, incompressible and to obey locally Amontons' rigid-plastic like friction law. This is at odds with most realistic situations where surfaces are rough down to the micrometer scale, resulting in a multicontact interface with a much richer mechanical response [8–12]. One may wonder how these characteristics modify CM's predictions. In this Letter, we address this question by probing the local displacement field at a contact between a rigid sphere and a rough elastomer block for which displacements can be measured with a submicrometer resolution using an image correlation velocimetry technique. This method directly makes use of the micro-junctions and micro-asperities present at the interface as markers.

The sphere is an optically smooth glass lens (radius of curvature $R = 128.8$ mm) and the elastomer block (50×50 mm, thickness $h = 15$ mm) is made of a crosslinked PolyDimethylSiloxane (PDMS Sylgard 184, Dow Corning, Young's modulus $E = 2.2 \pm 0.1$ MPa, Poisson ratio ν=0.5). Its surface has been rendered rough by moulding the cross-linker/PDMS melt against a Plexiglas surface mechanically abraded with an aqueous solution of SiC powder. Its topography was characterized with optical profilometry (M3D, Fogale Nanotech). Its power spectral density is a power law down to the micrometer scale and up to about 40 μm. Its characteristic thickness σ, taken as the standard deviation of the height distribution, was found to be $1.28 \pm 0.05\,\mu$m. Both glass and PDMS surfaces were cleaned with ethanol and dried with filtered air prior to any experiment.

A typical experiment consists in pulling the elastomer block in contact with the sphere under a prescribed normal load P at constant velocity V with a precision motorized actuator (LTA-HL, Newport), while recording simultaneously P, the shear load Q and images of the interface (Fig. 1). In all experiments, $V = 4\,\mu$m/s, a velocity small enough for visco-elastic interfacial dissipation to be negligible [13]. Both P and Q are measured at a sampling rate of 1 kHz by probing with position sensors the deflections of two cantilevers (Fig. 1, lower inset). The normal loading of the contact produces a significant shear force due to the coupling between normal and lateral motion of each cantilever. To circumvent this problem the contact is manually renewed until Q is less than 1% of P. During this separation procedure, no measurable pull-off force is observed, indicating that adhesion forces are neg-

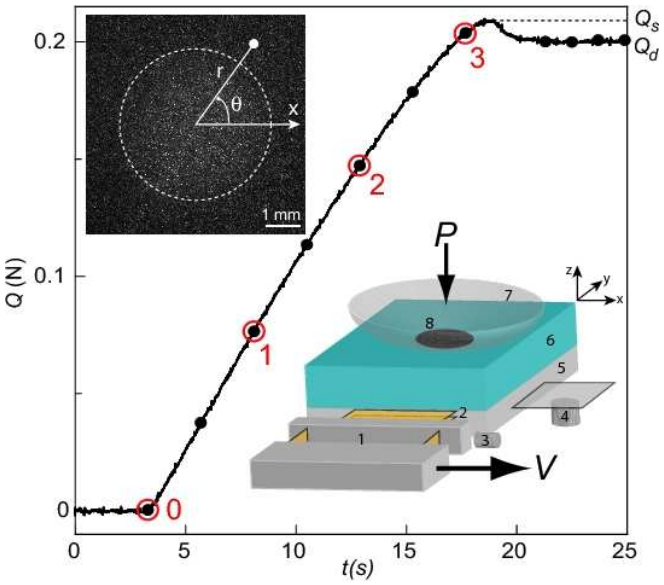

FIG. 1: (Color online) Sketch of the experimental setup (lower inset), time evolution of the shear force Q during the loading experiment with $P = 0.33$ N and $V = 4\,\mu$m/s, and image of the contact (upper inset) with its apparent contact border (white dashed line) and coordinates system. On the sketch, (1) is the shear cantilever (stiffness 9579 ± 25 N.m^{-1}) and (2) the normal one (stiffness 689 ± 5 N.m^{-1}), (3) and (4) are two capacitive position sensors (MCC10 and MCC20, Fogale Nanotech), (5) is a glass plate to which the PDMS block (6) is attached, (7) is the glass lens and (8) the resulting circular contact. On the Q curve, circled points and black disks indicate Q values at which the displacements are displayed in the next figures.

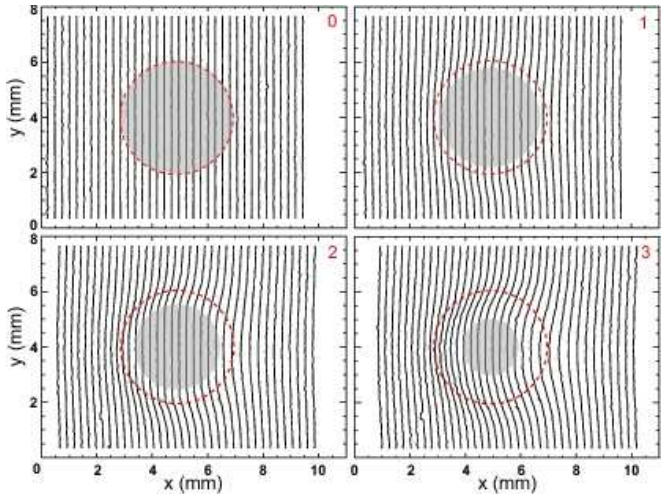

FIG. 2: (Color online) Snapshots of the displacement field $u_x(x, y)$ at the positions labeled 0, 1, 2 and 3 on the curve of Fig. 1. The reference, undeformed image is taken at position 0. $u(x, y)$ is represented by joining together with a solid line the extremities of the displacement vectors $\vec{u_x}$ of equal abscissa grid points. Since u_x lies in the range [0, 100 μm] an amplification factor of 30 has been used to ease vizualisation. The dashed circle is the border of the apparent contact region whose area is unaffected by the loading. The grey circular disk is a region of null displacement within the contact.

ligible [14, 15]. Q versus time curves, like the one shown in Fig. 1 for $P = 0.33$ N are reproducible for any P in the experimentally accessible range [0, 1 N], with the following typical behavior. While P varies by less than 1%, Q increases until it reaches a maximum value Q_s beyond which it slightly decreases before flattening at a constant value $Q_d = 0.96\,Q_s$ signaling a steady sliding regime with a dynamical coefficient of friction of about 0.6.

Imaging of the contact is done by illuminating the optically transparent PDMS block from below with a white LED and a ground glass diffuser, and using a stereomicroscope (Olympus SZ11). Images (Fig. 1, upper inset) are recorded by a CCD camera (Hamamatsu C8484-05G, 12 bits), whose 1344×1024 pixels sensor provides at the chosen magnification a field of view of 9.8×7.5 mm. Images' contrast results from the diffusive nature of the rough interface. In the contact region, additional bright spots correspond to the micro-junctions which favorably transmit light. Interfacial displacement fields are extracted from snapshots acquired at a 4 Hz frame rate using an image correlation velocimetry technique [16, 17].

It consists in finding, for a given subimage at position (x, y) in a reference image the displacement (u_x, u_y) which provides the maximum correlation with a subsequent deformed image. Since u_x is at least an order of magnitude larger than u_y, the correlation function is calculated by translating a square window of side length λ along the shear direction x only. With $\lambda = 20$ pixels, the u_x field is obtained with a spatial resolution of about 150 μm. The resolution on the displacements, found by correlating two different images of the interface prior to contact, and taken as the standard deviation of the displacements distribution, is about 275 nm, i.e. $1/30^{th}$ pixel. All displacements are defined respective to an image taken at $Q = 0$ N.

The displacement field at various applied forces along the loading curve of Fig. 1 was determined by correlating successive images with the $Q = 0$ reference image and is shown in Fig. 2 at four instants. For a given Q a central circular stick region coexists with a surrounding annulus in which slip has already occured. Its diameter decreases with Q and vanishes at Q_s. When $Q = Q_d$, u_x is the sum of two terms. The first one corresponds to the driving motion and is a uniform displacement of amplitude Vt. The second one is a residual displacement corresponding to the deformation of the elastomer block (Fig. 3, insets).

Such a scenario has been theoretically predicted by Cattaneo and Mindlin (CM) [5, 6] who have considered the combined normal and shear loading of a contact between spherical elastic bodies. Their calculations assume that (1) both surfaces are *smooth*, (2) the pressure distribution p within the contact is unchanged upon shearing

and given by Hertz contact theory, and (3) Amontons' law of friction is valid locally at any (r, θ) position (Fig. 1, upper inset), i.e. slip occurs wherever the shear stress q reaches μp, μ being the friction coefficient. For a contact of radius a between a rigid sphere of radius R and an elastic plane of reduced modulus $E^* = \frac{E}{1-\nu^2}$ under normal load P, $p(r, \theta)$ is given by $p(r) = p_0\sqrt{1 - r^2/a^2}$ with $p_0^3 = \frac{6PE^{*2}}{\pi^3 R^2}$. CM predicts the coexistence of an inner adhesive circular region of radius $c = a\left(1 - Q/(\mu P)\right)^{1/3}$ surrounded by an outer slip annulus. Using a superposition principle, CM's calculations provide complete analytic expressions for u_x within the contact, in both the stick and slip regions [3, 4]. Further derivations by Johnson [3] also give u_x outside the contact, thus providing the entire field at the interface. Comparison between CM's and measured u_x were done in two ways, by averaging $u_x(r, \theta)$ over θ (Fig. 3(a)), and by evaluating $u_x(a, \theta)$ with θ running from 0 to 2π (Fig. 3(b)).

In Fig. 3(a), displacement curves are shown for all values of Q corresponding to the dotted positions along the Q curve in Fig. 1. The inset shows $u_x(r) - u_x(0)$ in the steady sliding regime at the last four dotted points. Evaluation of $u_x(a, \theta)$ (Fig. 3(b)) is done similarly at the same dotted points in the transient loading regime and in steady sliding (inset). As shown, a good overall agreement between CM's predictions (red solid lines) and the measured u_x is found. Close look at their radial dependence even shows that the radius of the stick region is very close to CM's prediction for c. In addition, CM's expressions for $u_x(a, \theta)$ predict a $cos(2\theta)$ dependence, which is well reproduced over the whole θ range and for all Q.

Systematic deviations to CM's predictions are however clearly seen on the radial profiles displayed in Fig. 3(a). Outside the stick region ($r > c$), the experimental data points systematically lay below the predicted profiles. Furthermore, while CM's model predicts a kink in the radial displacement profiles at $r = a$, the measured curves remain smoother. This may be attributed to deviations to Hertz's pressure field around $r = a$, induced by the non-linear normal compressibility of the rough layer [9]. More surprisingly, in the stick region ($r < c$) a non-zero displacement in the submicrometric range is measured whose value increases with Q. This effect can be best caught by evaluating $u_x(r = 0)$ averaged over a disk of radius λ centered on the contact as a function of time. Results plotted in Fig. 4(a) and magnified on Fig. 4(b) show that in the loading phase $u_x(r = 0)$ increases continuously from 0 to about 1 μm.

This can be understood when considering that the image correlation velocimetry technique actually probes the mean displacement over the mean thickness σ of the rough layer. It indeed averages out intensity fluctuations due to both the micro-contacts and the non-contacting micro-asperities between micro-contacts. We can then

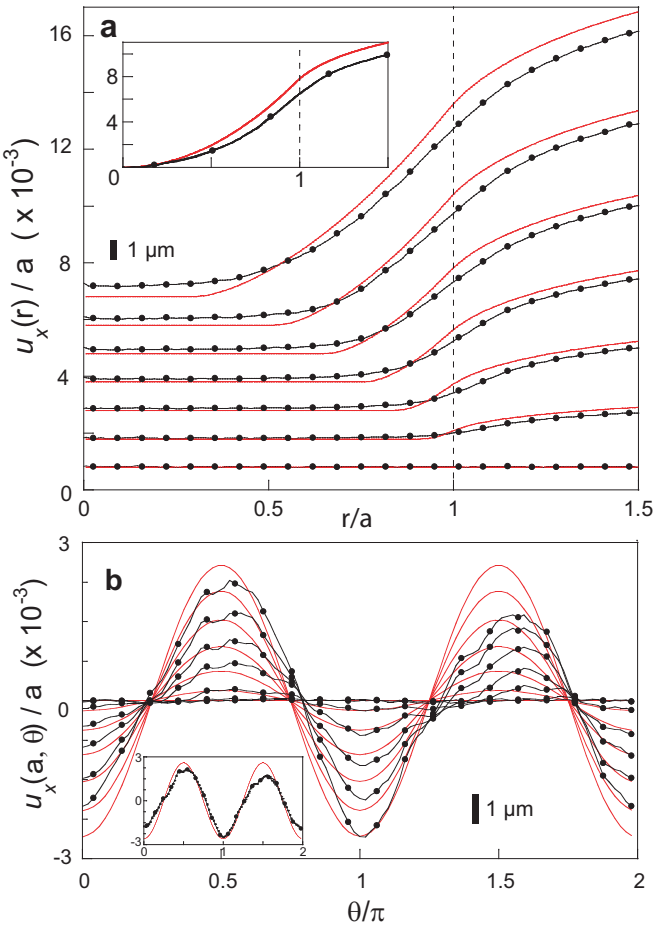

FIG. 3: (Color online) Comparison between the measured displacements (solid lines with filled disks) and CM's predictions (red solid lines). (a) $u_x(r)/a$ versus r/a. All curves are shifted arbitrarily along the y axis for vizualization and CM's curves have been smoothed out with a running window of size λ. From bottom to top, each set of curves corresponds to an increasing Q in the loading phase (black dots in Fig. 1). Inset shows 4 almost fully overlapped $u_x(r)/a$ curves in steady sliding measured at the last 4 dotted positions in Fig. 1. (b) $u_x(a, \theta)/a$ versus θ evaluated at the same Q in the transient regime, and in steady sliding (inset).

propose the following scenario. As long as $Q < Q_s$, summits of the asperities in contact remain stuck [22] while their underlying bulk base is displaced due to the applied shear. The rough layer is therefore deformed with a mean strain which can be estimated, at the center of the contact, as $\epsilon_0 = u_x(r = 0)/\sigma$ (Fig. 4(c)). The image correlation velocimetry technique developped here thus appears as a tool to probe locally the rheology of the rough layer, provided that the corresponding shear stress q_0 is known. Since our experiment does not allow any direct shear stress measurement, we have used CM's prediction for $q_0 = q(r = 0) = \mu p_0(1 - c/a)$ to obtain q_0 versus ϵ_0 (Fig. 4(d)). Clearly, the rough layer mechanical response deviates significantly from the Amontons'

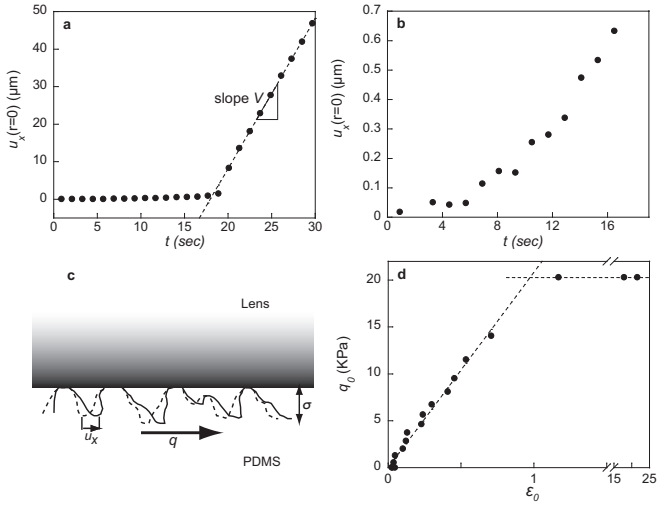

FIG. 4: (a) $u_x(r = 0)$ versus time. The dashed line is a linear fit, characterizing steady sliding at $V = 4\,\mu$m/s. (b) Magnified centered region of the previous plot. (c) Sketch detailling the mechanism resulting in a non-zero measured displacement in the stick region. (d) Calculated shear stress q_0 at $r = 0$ using CM's model versus the strain ϵ_0 defined as $u_x(r = 0)/\sigma$. Shown in dashed lines are the $q_0 = 20$ kPa horizontal line and a linear fit of the data points for $\epsilon_0 < 1$.

rigid-plastic like behavior assumed by CM. The friction law is rather elasto-plastic like with an effective shear modulus G_l given by $G_l = \partial q_0/2\partial\epsilon_0$ of about 10 kPa. This value is two orders of magnitude smaller than the bulk shear modulus $G = \frac{E}{2(1+\nu)} \approx 0.73$ MPa. It is fully consistent with previous measurements on multicontacts averaged over the whole apparent contact area [10]. It is expected to depend on the local pressure so that systematic measurements at successive different loads would be required to determine the complete mechanical response of the rough layer.

In this Letter we have implemented an image correlation velocimetry technique to measure with a submicrometer resolution the displacement field at a multicontact interface between a soft elastomer and a rigid body. This technique provides the first direct and non-invasive measurements of the interfacial slip field in both incipient sliding and steady sliding regimes at a sphere-on-plane contact. It can be directly applied to dynamical regimes, therefore complementing real contact area measurements on rough contacts such as those recently implemented in Plexiglas to investigate the interfacial dynamics of a multicontact interface at the onset of sliding [18, 19]. In principle, it could also be extended to smooth contacts by patterning the elastomer with markers located below its surface [20]

The measured displacement fields are well captured by the classical model of Cattaneo and Mindlin thus providing its first direct experimental test. Significant deviations are however observed and shown to result from the too stringeant smoothness assumption, which is often made in continuum mechanics calculations. The interfacial rough layer indeed exhibits a finite shear compliance. The latter was directly probed, allowing to evidence an elasto-plastic like friction law different from Amontons' law which is commonly believed to apply for multicontacts. These results provide direct experimental support to the interpretation of a recently observed non-Amontons behavior in a similar setup [21].

The auhors wish to thank Antoine Chateauminois and Christian Frétigny for fruitfull discussions.

* alexis.prevost@lps.ens.fr

[1] T. Baumberger and C. Caroli, Adv. Phys. **55**, 279 (2006).
[2] Y. Ben-Zion, J. Mech. Phys. Solids **49**, 2209 (2001).
[3] K. L. Johnson, *Contact Mechanics* (C. U. P., 1985).
[4] D. Hills and D. Nowell, *Mechanics of Fretting Fatigue* (Kluwer Academic Publishers, 1994).
[5] C. Cattaneo, Rendiconti dell'Accademia nazionale dei Lincei **27**, 214 (1938).
[6] R. D. Mindlin, Trans. ASME, Series E, J. Appl. Mech. **16**, 259 (1949).
[7] K. L. Johnson, Proc. R. Soc. London, Ser. A **230**, 531 (1955).
[8] J. A. Greenwood and J. B. P. Williamson, Proc. R. Soc. London, Ser. A **295**, 300 (1966).
[9] J. A. Greenwood and J. H. Tripp, Trans. ASME, Series E, J. Appl. Mech. **34**, 153 (1967).
[10] P. Berthoud and T. Baumberger, Proc. R. Soc. London, Ser. A **454**, 1615 (1998).
[11] B. Persson, Phys. Rev. Lett. **99**, 125502 (2007).
[12] M. Müser, Phys. Rev. Lett. **100**, 055504 (2008).
[13] O. Ronsin and K. L. Coeyrehourcq, Proc. R. Soc. London, Ser. A **457**, 1277 (2001).
[14] K. R. Shull, Mat. Sci. Eng. R. **36**, 1 (2002).
[15] K. N. G. Fuller and D. Tabor, Proc. R. Soc. London, Ser. A **345**, 327 (1975).
[16] F. Hild and S. Roux, Strain **42**, 69 (2006).
[17] J. Scheibert, *Mécanique du contact aux échelles mésoscopiques* (Edilivre, Collection Universitaire, 2008).
[18] S. M. Rubinstein, G. Cohen, and J. Fineberg, Nature **430**, 1005 (2004).
[19] S. Rubinstein, G. Cohen, and J. Fineberg, Phys. Rev. Lett. **96**, 256103 (2006).
[20] A. Chateauminois and C. Frétigny, Private communication (2008).
[21] J. Scheibert, A. Prevost, J. Frelat, P. Rey, and G. Debrégeas, Europhys. Lett. **83**, 34003 (2008).
[22] Direct confirmation that the micro-contacts remain stuck was obtained by zooming on individual asperities.

THEME 5 : APPROCHE BIOMIMETIQUE DE LA PERCEPTION TACTILE

Résumé : Le senseur tribologique MEMS décrit précédemment a été mis à profit dans le cadre d'une étude des caractéristiques physiques de la perception tactile digitale humaine. Ce senseur (micro-capteur et membrane élastique) présente des dimensions proches de celles du système tactile digital humain (mécanorécepteur cutané et peau). Nous avons pu ainsi évaluer directement les caractéristiques de vibrations sous-cutanées induites par le frottement du doigt sur une surface texturée par une approche de type bio-mimétique. Ce travail a permis en particulier de mettre en évidence un rôle possible des empreintes digitales pour la transduction de l'information tactile : nous avons montré que la présence de cette texturation particulière de la surface de la peau conduit à une sélection et une amplification d'un mode de vibration particulier. Ce mécanisme pourrait avoir des conséquences importantes pour le codage des informations de textures notamment.

La main est un instrument extraordinaire qui nous permet d'interagir avec notre environnement avec une précision bien supérieure à celle des meilleurs robots. Cette capacité résulte de la coordination entre le système moteur, qui contrôle l'activité des muscles, et le système tactile qui informe en permanence le système nerveux des contraintes s'exerçant à la surface de la peau. La sensibilité tactile cutanée des mains nous permet également d'extraire une grande quantité d'information sur les objets que nous manipulons, telle que leur courbure ou leur poids, les propriétés de rugosité ou d'adhésion de leur surface, ou encore la dureté du matériau qui les constitue.

Comme dans tout système sensoriel, la perception tactile implique une étape de transduction de l'information par un organe périphérique qui assure l'interface entre le monde extérieur et le système nerveux. L'information finale, traitée par le système nerveux central, dépend de façon cruciale des propriétés biomécaniques de cet organe qui contrôlent la façon dont l'information physique est filtrée, mise en forme puis traduite en activité nerveuse. Dans le cas du toucher humain, c'est la peau qui constitue cette interface : l'information tactile est entièrement contenue dans la séquence de déformation de la peau induite par le contact entre le doigt et l'objet. Ces déformations cutanées sont converties en signaux nerveux par des terminaisons nerveuses mécano-sensibles situées à une profondeur de l'ordre du millimètre sous la surface de la peau.

Afin d'obtenir une description complète de la perception tactile, il est donc nécessaire de comprendre comment les différentes caractéristiques physiques d'un substrat (forme, rugosité, adhésion, dureté, etc.) se traduisent mécaniquement au niveau sous-cutané dans des conditions naturelles d'exploration. Nous avons pour cela développé une approche bio-mimétique de la perception tactile en mettant au point un capteur tactile artificiel reproduisant le fonctionnement d'un mécanorécepteur lors d'une exploration dynamique[1]. Le micro-capteur de force MEMS (décrit au chapitre précédent) tient lieu de terminaison mécano-sensible artificielle. Il est recouvert d'une « peau » élastique formant une calotte sphérique de grand rayon de courbure et d'épaisseur millimétrique (Figure 9). Grâce à ce dispositif, nous nous sommes intéressés notamment au rôle des empreintes digitales dans le processus de transduction de l'information tactile associée à la perception des textures fines. A cet effet, deux types de « peau » ont été fabriquées, l'une lisse et l'autre présentant des structures en surface analogues aux empreintes digitales sous la forme de créneaux réguliers de période L=220 µm.

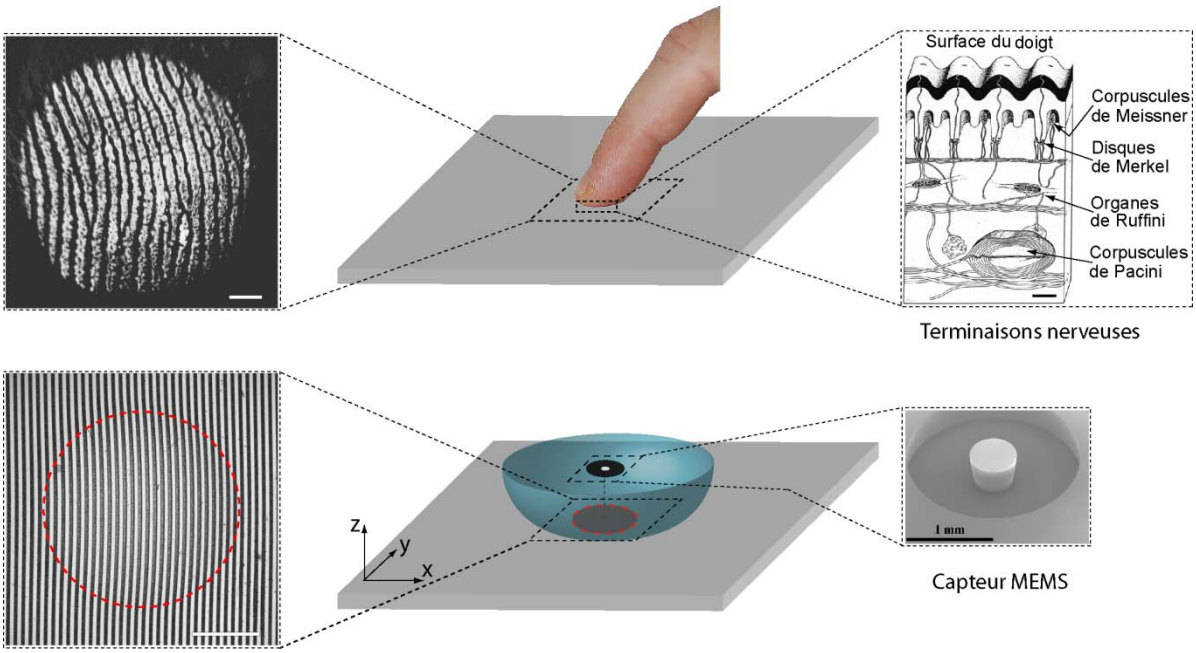

Figure 9 : Principe de l'approche biomimétique. Panel du haut : l'extrémité du doigt humain est couverte d'empreintes digitales (photo de gauche) et contient un grand nombre de terminaisons nerveuses mécano-réceptrices distribuées sous la surface de la peau jusqu'à des profondeurs de l'ordre de 2 mm (schéma de droite, d'après Darian-Smith, Handbook of Physiology,1984). Panel du bas : pour modéliser le fonctionnement d'un type de ces terminaisons nerveuses (Corpuscule de Pacini), un micro-capteur de force (CEA-LETI, Grenoble, partie sensible visible sur la photo de droite), a été recouvert d'une calotte sphérique élastique de PDMS d'épaisseur maximale 2 mm. La surface de celle-ci est soit lisse soit couverte de sillons parallèles analogues aux empreintes digitales (photo de gauche). Pour les deux photos de gaucge, la barre blanche mesure 2 mm. Ce senseur biomimétique est mis en contact puis frotté contre des lames de verres présentant une rugosité contrôlée de période de l'ordre de quelques dizaines de microns.

Ce capteur est frotté à charge et vitesse constantes sur des substrats plans à grande échelle mais dont la surface présente une rugosité contrôlée sous la forme de créneaux obtenus par photolithographie. Les arêtes de ces créneaux sont positionnées aléatoirement (et séparées en moyenne de 75 μm) afin de produire un bruit blanc topographique, c'est-à-dire une rugosité pour laquelle chaque longueur d'onde spatiale est présente avec une égale intensité. La Figure 10 montre les variations de pression mesurées à l'aide du capteur MEMS en fonction de la distance parcourue par le substrat, pour les deux types de peau. Dans le cas d'une peau lisse, le signal de pression présente des modulations sur des échelles de déplacement du substrat de l'ordre du millimètre. La présence d'empreintes digitales produit un signal dont l'enveloppe est similaire mais qui présente par ailleurs de larges oscillations à la longueur d'onde L des empreintes. Les empreintes digitales permettent donc une amplification spécifique, de type passe-bande, de l'information tactile associée aux textures de période spatiale similaire à celle des empreintes elles-mêmes.

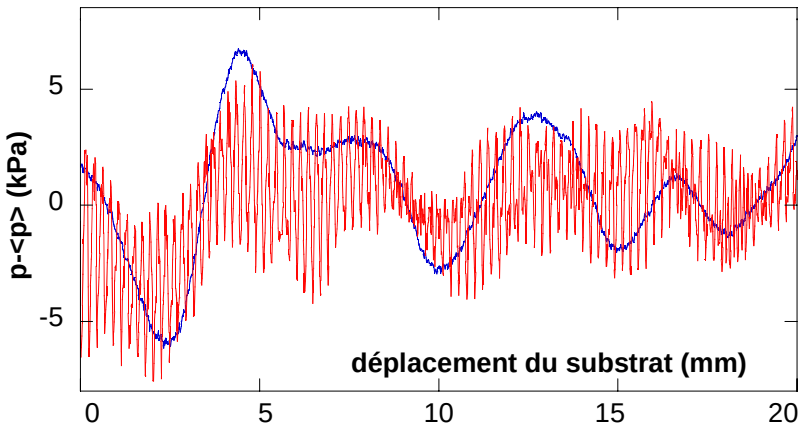

Figure 10 : Evolution de la pression (contrainte normale) mesurée à l'aide du micro-capteur de force MEMS en fonction du déplacement du substrat, dans le cas d'une peau lisse (bleu) et couverte de lignes parallèles (rouge). La présence de structures simulant les empreintes digitales fait apparaître une modulation de large amplitude du signal à la période spatiale des empreintes elles-mêmes (0.22mm).

Nous avons pu interpréter ce résultat dans le cadre d'un modèle linéaire. Nous avons établi que la transduction linéaire de l'information tactile (le processus de conversion de l'information topographique du substrat en signal temporel de pression) est entièrement contrôlée par une fonction de réponse qui s'exprime simplement en fonction des caractéristiques intrinsèques du capteur - ses dimensions, la profondeur à laquelle il se trouve dans la peau - et des paramètres d'exploration : le champ de contrainte moyen s'exerçant entre le "doigt" et le substrat, le coefficient de frottement, la vitesse d'exploration tactile, etc. Cette approche linéaire permet d'interpréter de façon directe les modifications de la transduction mécanique tactile induites par la présence d'empreintes digitales, et notamment le phénomène d'amplification spectrale observée.

L'utilisation de substrats présentant une rugosité aléatoire – un bruit de texture « blanc » - a permis de confirmer expérimentalement les formes prédites de la fonction de réponse linéaire pour les deux types de peau par une méthode dite de corrélation inverse. Cette méthode d'analyse de systèmes dynamiques est fondée sur un développement mathématique (Wiener/Volterra) dont le résultat pratique est que la réponse linéaire de tout système peut être obtenue en corrélant le signal d'entrée au signal de sortie dès lors que le premier présente les caractéristiques d'un bruit blanc gaussien.

Le système bio-mimétique utilisé pour cette étude constitue une version minimale de l'organe tactile. Cependant, les ingrédients physiques qui conduisent aux caractéristiques essentielles de la fonction de réponse stimulus/signal du système sont suffisamment simples pour qu'il soit raisonnable d'en analyser les conséquences fonctionnelles dans le cas d'un véritable doigt humain. Nous avons établi sa pertinence en mettant en évidence une modulation de la force de frottement induite par les empreintes dans un contact entre un vrai doigt et un substrat texturé[2]. En prenant en compte les conditions physiologiques réelles (la période spatiale des empreintes, la vitesse typique d'exploration tactile), la fréquence sélectionnée par les empreintes digitales se trouve dans la gamme 200-300Hz qui correspond au régime optimal de réponse de l'un des mécanorécepteurs digitaux appelé corpuscule de Pacini. Les empreintes digitales permettent donc un conditionnement du signal mécanique optimum pour le codage neuronal par le canal Pacinien qui est impliqué dans la perception des informations de textures fines (sub-millimétrique). Ce processus d'amplification des modulations de contraintes sous-cutané pourrait également permettre une détection plus efficace du glissement entre le doigt et le substrat, information essentielle aux tâches de manipulation.

Outre ces enjeux biologiques, ce résultat pourrait avoir des conséquences dans le domaine de l'haptique, c'est-à-dire pour l'introduction de capacité tactile dans des systèmes robotiques. Les systèmes actuels sont le plus souvent fondés sur une détection statique de la topographie des substrats au moyen de palpeur formés d'une matrice de capteurs dont la densité (au mieux de l'ordre de quelques centaines de microns) fixe la limite de résolution spatiale. Le résultat de notre étude suggère

que cette limite pourrait être franchie par une exploration tactile active et en structurant à petite échelle la surface de la membrane élastique couvrant les capteurs.

Références :

1. The role of fingerprints in the coding of tactile information probed with a biomimetic sensor, J. Scheibert, S. Leurent, A. Prevost et G. Debrégeas, Science 323 1503-1506 (2009)
2. Effect of fingerprints orientation on skin vibrations during tactile exploration of textured surfaces, Alexis Prevost, Julien Scheibert and Georges Debrégeas, *Communicative and Integrative Biology 2*(5) (2009)

the interaction was greatly enhanced in the presence of SYD-1 (Fig. 4, C, D, and G), suggesting that SYD-1 facilitates binding between ELKS-1 and SYD-2. Consistent with this result, SYD-1 directly interacted with ELKS-1 (Fig. 4, E and G), and this interaction was weakened in the presence of RSY-1ΔSR (Fig. 4, F and G). Thus, one way in which RSY-1 regulates SYD-2 function is indirectly by weakening the interaction of SYD-1 with ELKS-1 and thus potentially blocking the ability of SYD-1 to facilitate SYD-2 function (Fig. 4K).

Given that the ELKS-1/SYD-2 binding is very weak in the absence of SYD-1 in our assay, we could not test whether interaction of RSY-1 with SYD-2 inhibited ELKS-1/SYD-2 binding. However, the ELKS-1/SYD-2 interaction does increase when SYD-2 contains a gain-of-function mutation, $Arg^{184} \rightarrow Cys^{184}$ (R184C) (*14*), which was verified in our cell-based assay (Fig. 4, H and J). We then tested the effect of RSY-1 on this interaction and found that the interaction between ELKS-1 and SYD-2R184C was weakened in the presence of RSY-1ΔSR (Fig. 4, I and J), suggesting that, besides acting via SYD-1, RSY-1 can also directly antagonize the ability of SYD-2 to recruit ELKS-1 (Fig. 4K).

It is increasingly clear that positive and negative regulators control synapse development at multiple levels. For example, the transcription factor MEF2 globally regulates the number of excitatory synapses (*7*). Three ubiquitin ligase complexes also regulate presynaptic development (*5*, *8*, *29*). Here, RSY-1 was shown to act as a negative regulator of synaptogenesis by counteracting SYD-1 function to inhibit SYD-2–dependent presynaptic assembly in the HSNL neuron. RSY-1 controls the amount of synaptic material recruited to presynaptic sites. RSY-1 also plays a role in establishing a balance between synapse formation and synapse elimination. RSY-1 achieves these functions by interacting with integral components of the synapse assembly machinery and by regulating a dense network of protein-protein interactions between various active-zone molecules (Fig. 4K).

References and Notes

1. M. Zhen, Y. Jin, *Nature* **401**, 371 (1999).
2. M. Zhen, Y. Jin, *Curr. Opin. Neurobiol.* **14**, 280 (2004).
3. C. L. Waites, A. M. Craig, C. C. Garner, *Annu. Rev. Neurosci.* **28**, 251 (2005).
4. Q. Chang, R. J. Balice-Gordon, *Neuron* **26**, 287 (2000).
5. P. van Roessel, D. A. Elliott, I. M. Robinson, A. Prokop, A. H. Brand, *Cell* **119**, 707 (2004).
6. K. Nakata *et al.*, *Cell* **120**, 407 (2005).
7. S. W. Flavell *et al.*, *Science* **311**, 1008 (2006).
8. M. Ding, D. Chao, G. Wang, K. Shen, *Science* **317**, 947 (2007); published online 11 July 2007 (10.1126/science.1145727).
9. M. P. Klassen, K. Shen, *Cell* **130**, 704 (2007).
10. V. Y. Poon, M. P. Klassen, K. Shen, *Nature* **455**, 669 (2008).
11. C. Desai, H. R. Horvitz, *Genetics* **121**, 703 (1989).
12. K. Shen, C. I. Bargmann, *Cell* **112**, 619 (2003).
13. M. R. Patel *et al.*, *Nat. Neurosci.* **9**, 1488 (2006).
14. Y. Dai *et al.*, *Nat. Neurosci.* **9**, 1479 (2006).
15. Materials and methods are available as supporting material on *Science* Online.
16. G. Zimowska *et al.*, *Invest. Ophthalmol. Vis. Sci.* **44**, 4715 (2003).
17. P. Ouyang, *Biochem. Biophys. Res. Commun.* **263**, 192 (1999).
18. J. H. Joo *et al.*, *Mol. Vis.* **11**, 133 (2005).
19. R. Alpatov *et al.*, *Mol. Cell. Biol.* **24**, 10223 (2004).
20. P. Wang, P. J. Lou, S. Leu, P. Ouyang, *Biochem. Biophys. Res. Commun.* **294**, 448 (2002).
21. R. Baumeister, Y. Liu, G. Ruvkun, *Genes Dev.* **10**, 1395 (1996).
22. D. H. Hall, E. M. Hedgecock, *Cell* **65**, 837 (1991).
23. D. A. Wagh *et al.*, *Neuron* **49**, 833 (2006).
24. R. J. Kittel *et al.*, *Science* **312**, 1051 (2006); published online 13 April 2006 (10.1126/science.1126308).
25. S. L. Deken *et al.*, *J. Neurosci.* **25**, 5975 (2005).
26. D. Blanchard, H. Hutter, J. Fleenor, A. Fire, *Mol. Cell. Proteomics* **5**, 2175 (2006).
27. M. D. Muzumdar, B. Tasic, K. Miyamichi, L. Li, L. Luo, *Genesis* **45**, 593 (2007).
28. J. Ko, M. Na, S. Kim, J. R. Lee, E. Kim, *J. Biol. Chem.* **278**, 42377 (2003).
29. T. A. Fulga, D. Van Vactor, *Neuron* **57**, 339 (2008).

30. We would like to thank the *Caenorhabditis* Genetics Center and the Japanese NBPR for strains; Y. Kohara (National Institute of Genetics, Japan) for Y53H1A.1 cDNAs; J. Audhya (University of California, San Diego) for *C. elegans* optimized mCherry cDNA; L. Luo (Stanford University) for vertebrate mCherry cDNA; T. Meyer (Stanford University) for eYFP-C3 plasmid; M. Park (Stanford University) for mCerulean-C1 plasmid; C. Gao for technical assistance; and members of the Shen lab, C. Bargmann, T. Clandinin, and L. Luo for critical comments on the manuscript. We would also like to thank B. Grill (Stanford University) for providing protocol and guidance for coimmunoprecipitation experiments. This work was funded by grants awarded to K.S. [from NIH (1R01NS048392), the Human Frontier Science Foundation, the Howard Hughes Medical Institute, and the W. M. Keck Foundation] and by a National Research Service Award predoctoral fellowship awarded to M.R.P. by NIH.

Supporting Online Material

www.sciencemag.org/cgi/content/full/323/5920/1500/DC1
Materials and Methods
Figs. S1 to S11
References

26 November 2008; accepted 7 January 2009
10.1126/science.1169025

The Role of Fingerprints in the Coding of Tactile Information Probed with a Biomimetic Sensor

J. Scheibert,* S. Leurent, A. Prevost,† G. Debrégeas‡

In humans, the tactile perception of fine textures (spatial scale <200 micrometers) is mediated by skin vibrations generated as the finger scans the surface. To establish the relationship between texture characteristics and subcutaneous vibrations, a biomimetic tactile sensor has been designed whose dimensions match those of the fingertip. When the sensor surface is patterned with parallel ridges mimicking the fingerprints, the spectrum of vibrations elicited by randomly textured substrates is dominated by one frequency set by the ratio of the scanning speed to the interridge distance. For human touch, this frequency falls within the optimal range of sensitivity of Pacinian afferents, which mediate the coding of fine textures. Thus, fingerprints may perform spectral selection and amplification of tactile information that facilitate its processing by specific mechanoreceptors.

The hand is an important means for human interaction with the physical environment (*1*). Many of the tasks that the hand can undertake—such as precision grasping and manipulation of objects, detection of individual defects on smooth surfaces, and discrimination of textures—depend on the exquisite tactile sensitivity of the fingertips. Tactile information is conveyed by populations of mechanosensitive afferent fibers innervating the distal fingerpads (*2*, *3*). In recent years, a breakthrough in our understanding of the coding of roughness perception has been made with the experimental confirmation of Katz's historical proposition of the existence of two independent coding channels that are specific for the perception of coarse and fine textures (*4*–*6*). The perception of coarse textures (with features of lateral dimensions larger than about 200 μm) relies on spatial variations of the finger/substrate contact stress field and is mediated by the slowly adapting mechanoreceptors (*7*). The perception of finer textures (<200 μm) requires the finger to be scanned across the surface because it is based on the cutaneous vibrations thus elicited. These vibrations are intensively encoded, principally by Pacinian fibers (*8*), which are characterized by a band-pass behavior with a best frequency (i.e., the stimulus frequency where maximum sensitivity occurs) on the order of 250 Hz (*9*). The most elaborated description of the latter coding scheme was given by Bensmaïa and Hollins, who directly measured the skin vibrations of fingers scanning finely tex-

Laboratoire de Physique Statistique de l'Ecole Normale Supérieure, CNRS UMR 8550, Associé aux Universités Paris 6 et Paris 7, 24 rue Lhomond, 75231 Paris Cedex 05, France.

*Present address: Physics of Geological Processes, University of Oslo, Post Office Box 1048 Blindern, N-0316 Oslo, Norway.
†Present address: Laboratoire de Physique Théorique, 24 rue Lhomond, 75231 Paris Cedex 05, France.
‡To whom correspondence should be addressed. E-mail: georges.debregeas@lps.ens.fr.

Downloaded from www.sciencemag.org on March 13, 2009

tured substrates. They were able to correlate the perceived roughness of the surface with the power of the texture-induced vibrations weighted by the Pacinian spectral sensitivity (*10*, *11*).

Among the four types of mechanoreceptors that convey tactile information, Pacinian corpuscles (PCs) have the most extended receptive field and therefore the lowest spatial resolution. This may seem paradoxical given their involvement in the tactile perception of fine features (*12*, *13*). In standard psychophysical tests, the substrates used as stimuli are made of regularly spaced dots or bars (*1*). The resulting skin vibrations are confined to a single frequency whose value can be actively tuned by the subject through the scanning velocity so that it falls within the PC optimal range of sensitivity. Such regular stimuli substrates thus favor tactile identification or classification tasks. In contrast, for natural surfaces where features are randomly distributed and exhibit a wide spectrum of size, the elicited skin vibrations are expected to be spread over a large range of frequencies, among which only a limited fraction contributes to the PC activity.

To address this question on how low-resolution receptors encode fine textural information, the present study investigates the mechanical filtering properties of the skin. It aims at characterizing how textural information at any spatial scale (less than the finger/substrate contact diameter) is converted into subcutaneous vibrations in the vicinity of the mechanoreceptors during a dynamic tactile exploration. Because there is currently no way to measure experimentally the subcutaneous stress using a human subject, our approach is based on the use of a biomimetic tactile sensor whose functioning principle and main geometrical characteristics are matched to those of the human fingertip. This allows us to test, in particular, the role of epidermal ridges (fingerprints) in this transduction process. Two distinct functional roles have been so far attributed to these characteristic structures of the digital skin. Fingerprints are believed to reinforce friction and adhesion of the fingerpads, thus improving the ability to securely grasp objects or supports (*1*, *14*). They may also be implicated in tactile perception, each of them acting as a magnifying lever, thus increasing the subsurface strain with respect to the surface deformation (*15*, *16*). Here, we show that fingerprints may have a strong impact on the spectral filtering properties of the skin in dynamic tactile exploration.

The tactile sensor aims at mimicking the operation of the PC in dynamic tactile exploration (*17*, *18*). As far as possible, the various geometrical and mechanical characteristics of the sensor are scaled to its biological counterpart (see fig. S1 for a comparison of key parameters). The sensing element consists of a microelectromechanical system (MEMS) device that provides force measurements in a region of millimeter extension. This microforce sensor is attached to a rigid base and covered with an elastic spherical cap mimicking the fingertip skin (Fig. 1A). This cap, made of cross-linked poly(dimethylsiloxane) (PDMS), has a maximum thickness h = 2 mm. Its surface is either "smooth" or "fingerprinted," that is, patterned with a regular square wave grating of period λ = 220 μm and depth 28 μm. The tactile sensor is mounted on a double cantilever system, allowing one to record the normal and tangential loads using capacitive position sensors. In a typical experiment, the sensor is scanned at constant velocity across a rigid, nominally flat substrate under a constant normal load P = 1.71 N, yielding a contact zone of centimeter extension. This value for the load, together with the periodicity of the fingerprint-like structure, is chosen so that the number of ridges within the contact in the artificial system is close to that observed with an actual fingerpad under standard exploratory load (as illustrated in Fig. 1, B and C).

The stimuli consist of white-noise one-dimensional (1D) textured substrates (Fig. 1A,

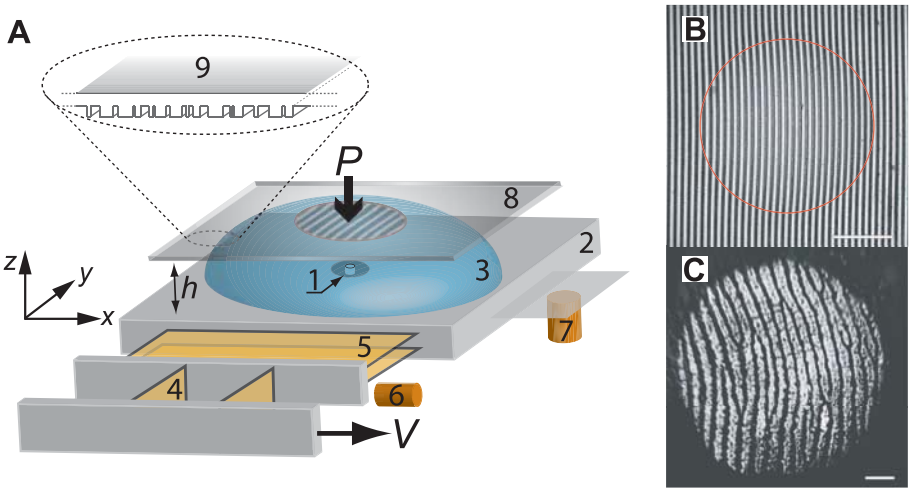

Fig. 1. (**A**) Sketch of the experimental setup. A MEMS microforce sensor (1) is mounted on a rigid base (2). It is covered with a spherical elastomer cap (3) of maximum thickness h = 2 mm and whose surface is smooth or patterned with parallel ridges. The resulting tactile sensor is mounted on a double-cantilever system (4, 5) allowing one to measure the total normal and tangential loads exerted on the sensor using capacitive position sensors (6, 7). In a typical experiment, the tactile sensor is scanned at constant speed v (using a linear motor) and under constant normal load P, across glass slides (8) whose surface is patterned with a 1D random square-wave grating (9). (**B**) Snapshot of the contact between the fingerprinted cap and a smooth glass slide in steady sliding. Wells between the elastomer's ridges appear bright, and the red circle, also shown on (A), defines the border of the contact. Actual contact only occurs on the ridges' summits. Ridges are slightly deformed at the periphery of the contact zone because of interfacial friction. (**C**) For comparison, this snapshot displays the contact between a human fingertip and a smooth glass surface with $P \approx 0.5$ N (a typical value in tactile exploration). Scale bars, 2 mm.

Fig. 2. (**A**) Typical pressure variation $p - \langle p \rangle$ measured with the smooth (blue) and fingerprinted (red) biomimetic fingers as a function of the substrate displacement u. The stimulus substrate used to produce these signals is a patterned glass slide exhibiting 1D random roughness. (**B**) Normalized power spectra of both signals obtained by Fourier transform averaged over four data sets, equivalent to a substrate of total length 180 mm. Shown in dashed lines is the theoretical power spectrum of the random pattern used as stimuli.

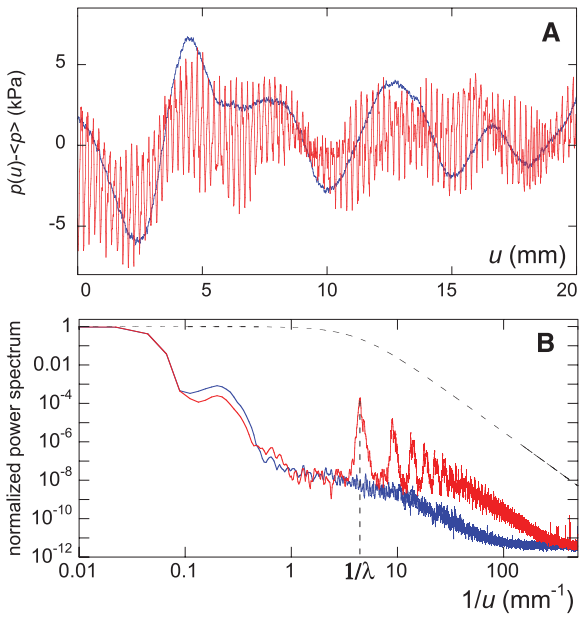

Downloaded from www.sciencemag.org on March 13, 2009

upper inset). They are obtained by patterning glass slides with a 28-μm-deep square wave grating whose edges are positioned at random positions with a mean grating width of 75 μm (*17*). The fingerprint-like ridges (when present) and substrate gratings are parallel to each other and oriented perpendicularly to the sliding direction. For moderate scanning velocities (v < 0.4 mm/s) and a given normal load, the pressure signal $p(t)$ is found to be a sole function of the substrate position at time t, regardless of the scanning velocity v (figs. S2 and S3). All experiments are performed at constant v = 0.2 mm/s, well within this velocity-independent regime of friction. To facilitate the analysis, data are systematically plotted as a function of the sensor/substrate relative displacement $u = vt$, as a strict equivalence exists between time and substrate displacement in steady sliding.

Figure 2A shows the typical pressure variations $p(u) - \langle p \rangle$ (where $\langle p \rangle$ is the average pressure) measured with the microforce device as the sensor is scanned across a textured surface. The smooth sensor exhibits pressure modulations with a characteristic wavelength in the millimeter range. The fingerprinted system reveals similar long-wavelength modulations to which are superimposed rapid oscillations whose period corresponds to a displacement of the substrate over the interridge distance λ = 220 μm. A characterization of both sensors' filtering properties is given in Fig. 2B, which displays the power spectra of both signals together with that of the input stimulus, that is, the substrate topography (dashed line). The smooth sensor acts as a low-pass filter as it rapidly attenuates all pressure modulations induced by texture components of wavelength smaller than ≈1 mm. In contrast, the fingerprinted sensor exhibits band-pass filtering characteristics around the spatial frequency 1/λ (with further harmonics at integer multiples of 1/λ). The presence of fingerprint-like ridges results in an amplification by a factor of 100 of the pressure modulations induced by a texture of wavelength λ (*19*).

These filtering characteristics can be interpreted to first order using a linear mechanical description of tactile sensing (*20*). Consider a small linear force sensor embedded at depth h in an elastic skin and located at ($x = 0$, $y = 0$). Its response to localized unit forces applied at various positions (x,y) on the skin surface defines its receptive field $F(x,y)$. The sensor signal p induced by any stress field $\sigma^s(x,y)$ applied at the skin surface then reads $p = \iint F(x, y)\sigma^s(x, y)\,dx\,dy$. We denote $\bar{\sigma}(x, y)$ the (time invariant) contact stress field resulting from the continuous rubbing of a smooth substrate under a given load. If the substrate exhibits a fine texture, the stress field σ^s becomes dependent on the substrate position u. As u varies, σ^s is modulated around the reference field $\bar{\sigma}(x, y)$. The use of substrates exhibiting a two-level topography and a large enough contrast prevents any contact above the wells (as optically evidenced in fig. S4). The contact pressure is thus zero over half of the apparent contact region, whereas it is expected to be about twice the time-averaged stress field $\bar{\sigma}(x, y)$ at the location of the substrate summits. As a first approximation, one may thus write the superficial stress field as a function of u in the form

$$\sigma^s(x, y) = \bar{\sigma}(x, y).(1 + T(u - x)) \qquad (1)$$

where $T(x)$ is the normalized two-level function ($T = \pm 1$), representing the topography of the surface. An exact calculation of the contact stress at a given location should take into account the local topography of the substrate and not just the average fraction of summits. The induced corrections should be important at short length-scales but become small when considering stress modulations over distances larger than the mean grating period.

With this expression, the pressure signal is then given by

$$p(u) = \langle p \rangle + \iint (F.\bar{\sigma})(x, y).T(u - x)dxdy \qquad (2)$$

The transduction of tactile information is controlled by the product of the receptive field F and the reference stress field $\bar{\sigma}$. The function F characterizes the intrinsic properties of the receptor. It is expected to have a typical lateral extension of order h and to be fairly independent of the skin topography (such as fingerprints), provided that the height of the surface features is less than h (*21*). The reference field $\bar{\sigma}$ depends on the exploratory conditions such as the normal load P, the friction coefficient, or the position of the contact zone with respect to the sensor location. Unlike F, the stress field $\bar{\sigma}$ is highly sensitive to the skin surface topography. In particular, the presence of fingerprints a few tens of micrometers deep leads to a complete extinction of $\bar{\sigma}$ along regularly spaced lines (as illustrated in fig. S6), resulting in the observed spectral amplification of the signal at the frequency 1/λ.

Equation 2 can be rewritten as $p(u) = \langle p \rangle + \int g_1(x)T(u - x)dx$ where $g_1(x) = \int (F.\bar{\sigma})(x, y)dy$ now defines the linear response function of the sensor with respect to 1D two-level stimuli substrates. The use of white-noise stimuli enables us to implement a Wiener-Volterra reverse-correlation method and extract $g_1(x)$directly from the measurements, $g_1(x) = \langle p(u)T(u - x)\rangle$ (*22*, *23*). The result of this computation for both smooth and fingerprinted sensors is plotted on Fig. 3. In qualitative agreement with the linear model, both response functions exhibit an

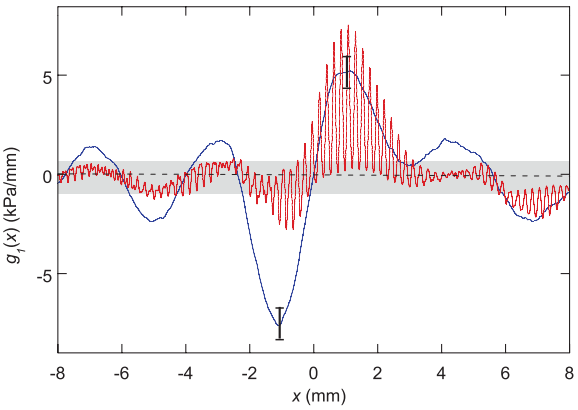

Fig. 3. Linearized stimulus-signal response functions $g_1(x)$ computed by cross-correlating the pressure signals and the stimulus topography $T(x)$, for both smooth (blue) and fingerprinted (red) systems. These data were obtained by averaging over three data sets, each one corresponding to a substrate length of 45 mm. The expected statistical deviation due to the finite length of the substrates was estimated numerically to be ±0.75 kPa/mm. This value is shown with the error bars and the shaded rectangle.

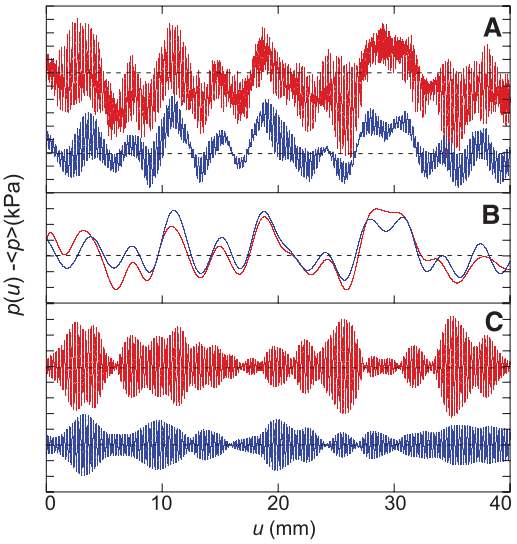

Fig. 4. (**A**) In red, pressure signal $p - \langle p \rangle$ measured with the fingerprinted sensor on a rough substrate. In blue, predicted signal obtained by convoluting the substrate topography function $T(x)$ with the linear response function $g_1(x)$. The latter was obtained independently by reverse correlation using two distinct 45-mm-long substrates. The dotted line indicates the $y = 0$ axis, and each interval along the y axis corresponds to a pressure variation of 1 kPa. For easier comparison, the same signals are plotted after applying (**B**) a low-pass filter with a cutoff frequency of 1/(2λ) and (**C**) a band-pass filter centered around the peak frequency 1/λ.

Downloaded from www.sciencemag.org on March 13, 2009

envelope of lateral extension of order h, and the response function of the fingerprinted sensor is further modulated with a spatial period λ. These functions can be tested by confronting actual measurements of $p(u) - \langle p \rangle$ with the predicted signal $\int g_1(x)T(u - x)dx$ as shown in Fig. 4A for the fingerprinted system. To facilitate the comparison, Fig. 4, B and C, displays the low- and high-frequency components, respectively. The linear response function allows one to reproduce the low-frequency signal. Although it correctly predicts the maxima and minima of the high-frequency component, it fails to capture its amplitude, which indicates that nonlinear effects might not be negligible for small length-scales. These effects could be taken into account by correlating p with the successive powers of T in order to include additional terms of the Wiener-Volterra series to describe the response function. However, this computation would require using a much larger set of stimuli to provide sufficient statistics.

Although the biomimetic tactile sensor used in this study offers a crude version of the finger physiology (*24*, *25*), the mechanism of spectral selection it helped unravel depends on a very limited set of ingredients and should therefore be relevant to human digital touch. Namely, it requires that the surface of the tactile sensor displays a regularly ridged topography whose spatial period and amplitude are much smaller than the receptive field diameter and the mechanoreceptor's depth. In these conditions, such ridges have little influence on the skin deformations induced by a coarse texture (of spatial scale larger than the interridge distance λ). However, by shaping the interfacial contact stress field, such epidermal ridges give rise to an amplification of the subsurface stress modulations induced by a texture of characteristic wavelength equal to λ. In the time domain, this spatial period corresponds to a frequency $f_0 = v/\lambda$ where v is the finger/substrate relative velocity. In natural exploratory conditions, v is observed to be on the order of 10 to 15 cm/s (*1*). With a typical interridge distance $\lambda \approx 500$ μm, this yields a frequency $f_0 \approx 200$ to 300 Hz on the order of the best frequency of the Pacinian fibers that mediate the coding of fine textures. Fingerprints thus allow for a conditioning of the texture-induced mechanical signal that facilitates its processing by specific mechanoreceptors. It should be noted that this process is strongly dependent on the orientation of the ridges with respect to the scanning direction (fig. S7). In humans, fingerprints are organized in elliptical twirls so that each region of the fingertip (and thus each PC) can be ascribed with an optimal scanning orientation. Further studies are needed to elucidate how this may reflect on the exploratory procedures (such as fingertip trajectory and contacting zone) used by humans during texture evaluation tasks.

Remarkably, the response function of the fingerprinted system displayed in Fig. 3 is analogous to a Gabor filter because it provides both spatial and spectral resolution. Such filters are classically used in image analysis and have been identified in visual systems at the neural level (*26*). They are known to provide orientation discrimination, contrast enhancement, and motion detection. One may therefore expect, beyond the spectral filtering process discussed here, other interesting functional consequences of fingerprints, presumably relevant to the design of realistic haptic interfaces for humanoid robots (*27*, *28*).

References and Notes

1. L. A. Jones, S. J. Lederman, *Human Hand Function* (Oxford Univ. Press, 2006).
2. I. Darian-Smith, in *Handbook of Physiology: The Nervous System: Sensory Processes* (American Physiological Society, Bethesda, MD, 1984), vol. 3, chap. 17.
3. K. O. Johnson, J. R. Phillips, *J. Neurophysiol.* **46**, 1177 (1981).
4. D. Katz, *The World of Touch*, I. E. Krueger, Transl. and Ed. (Hillsdale, NJ, Erlbaum, 1989; original work published 1925).
5. M. Hollins, S. J. Bensmaïa, S. Washburn, *Somatosens. Mot. Res.* **18**, 253 (2001).
6. M. Hollins, S. J. Bensmaia, *Can. J. Exp. Psychol.* **61**, 184 (2007).
7. S. J. Lederman, M. M. Taylor, *Percept. Psychophys.* **12**, 401 (1972).
8. M. A. Srinivasan, J. M. Whitehouse, R. H. Lamotte, *J. Neurophysiol.* **63**, 1323 (1990).
9. J. C. Makous, R. M. Friedman, C. J. Vierck, *J. Neurosci.* **15**, 2808 (1995).
10. S. J. Bensmaia, M. Hollins, *Somatosens. Mot. Res.* **20**, 33 (2003).
11. S. J. Bensmaia, M. Hollins, *Percept. Psychophys.* **67**, 842 (2005).
12. R. S. Johansson, *J. Physiol.* **281**, 101 (1978).
13. M. Hollins, S. R. Risner, *Percept. Psychophys.* **62**, 695 (2000).
14. M. Cartmill, *Am. J. Phys. Anthropol.* **50**, 497 (1979).
15. N. Cauna, *Anat. Rec.* **119**, 449 (1954).
16. R. S. Fearing, J. M. Hollerbach, *Int. J. Robot. Res.* **4**, 40 (1985).
17. Materials and methods are available as supporting material on *Science* Online.
18. J. Scheibert, A. Prevost, J. Frelat, P. Rey, G. Debrégeas, *Europhys. Lett.* **83**, 34003 (2008).
19. A comparable spectral amplification is observed with finely abraded glass substrates (see fig. S5).
20. R. D. Howe, M. R. Cutkosky, *IEEE Trans. Robot. Autom.* **9**, 140 (1993).
21. K. L. Johnson, *Contact Mechanics* (Cambridge Univ. Press, Cambridge, 1985).
22. N. Wiener, *Nonlinear Problems in Random Theory* (MIT Press, Cambridge, MA, 1958).
23. F. Rieke, D. Warland, R. de Ruyter van Steveninck, W. Bialek, *Spikes: Exploring The Neural Code* (MIT Press, Cambridge, MA, 1999).
24. K. Dandekar, B. I. Raju, M. A. Srinivasan, *J. Biomed. Eng.* **125**, 682 (2003).
25. Q. Wang, V. Hayward, *J. Biomech.* **40**, 851 (2007).
26. J. P. Jones, L. A. Palmer, *J. Neurophysiol.* **58**, 1233 (1987).
27. R. Crowder, *Science* **312**, 1478 (2006).
28. V. Maheshwari, R. F. Saraf, *Science* **312**, 1501 (2006).

29. This project was supported primarily by CNRS basic funding and in part by the EU-NEST (New and Emerging Science and Technology) program, MONAT (Measurement of Naturalness) project (contract 21, number 29000). We are grateful to D. Chatenay and L. Bourdieu for fruitful discussions and careful reading of the manuscript.

Supporting Online Material

www.sciencemag.org/cgi/content/full/1166467/DC1
Materials and Methods
Figs. S1 to S7
References

26 September 2008; accepted 16 January 2009
Published online 29 January 2009;
10.1126/science.1166467
Include this information when citing this paper.

Downloaded from www.sciencemag.org on March 13, 2009

Je souhaite, dans les années à venir, prolonger les activités décrites dans les deux derniers chapitres. Il s'agira en particulier (*1*) de poursuivre, grâce aux nouveaux dispositifs multi-MEMS notamment, l'étude de la perception tactile digitale en explorant d'autres composantes de cette perception (surfaces réelles, perception du glissement, etc.) (*2*) de développer une approche statistique du comportement des interfaces frottantes multi-contact s'appuyant sur l'utilisation de surfaces micro-structurées par photolithographie, dans le cadre d'une collaboration avec l'équipe de Antoine Chateauminois et Christian Fretigny au PPMD à l'ESPCI.

Par ailleurs, je suis engagé depuis cette année dans une collaboration avec une équipe de neuroscience du CNRS (Daniel Shulz, UNIC, Gif sur Yvette) visant à comparer les stratégies de codage de l'information tactile chez l'humain et le rat. Nous souhaitons appliquer certaines des approches méthodologiques (expérimentale et théorique) développées dans le projet bio-mimétique à l'étude de la perception tactile vibrissale chez le rongeur.

Enfin, je travaille actuellement au développement de surfaces texturées actives utilisant certaines techniques issues du domaine de la micro-fluidique. Ces surfaces pourraient servir d'interfaces haptiques, i.e. capables de produire une sensation tactile.

A) TRANSDUCTION DE L'INFORMATION TACTILE CHEZ L'HUMAIN ET LE RONGEUR.

Depuis quelques mois, nous disposons de barrettes multi-capteurs 10x1 et 30x1 utilisant la même technologie MEMS que celle décrite précédemment (Figure 11). Le pas de ces réseaux est de 1mm (ce qui a impliqué une réduction d'un facteur trois des dimensions des capteurs) et la sensibilité en pression est augmentée d'un facteur 5 environ. Le capteur linéaire a été intégré dans une membrane élastomère et sa réponse à une indentation ponctuelle a été calibrée. Ce nouveau senseur biomimétique ouvre de nouvelles possibilités d'analyse des champs des contraintes sous-cutanées, et notamment l'examen de leurs corrélations spatiales et temporelles dont il est connu qu'elles contribuent au codage de l'information tactile de forme notamment (1).

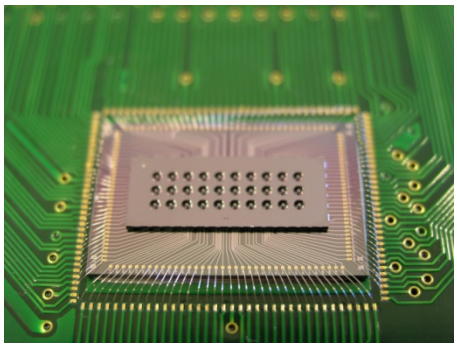

Figure 11 : barrette 3x10 MEMS montée sur support électronique. La structure sensible est inchangée par rapport au capteur de la ***Erreur ! Source du renvoi introuvable.****, si ce n'est une réduction en taille. Le pas du réseau est de 1mm.*

Nous envisageons de développer d'autres dispositifs bio-mimétiques, tirant parti des techniques optiques développées dans le projet frottement, pour extraire les champs de contraintes à l'interface peau-substrat. Il s'agira d'une membrane élastique texturée d'épaisseur millimétrique et gonflée à l'air. La déformation de la membrane, induite par le frottement, sera mesurée optiquement en

visualisant la face interne de la membrane (celle qui n'est pas en contact avec le substrat). Nous souhaitons également intégrer à une profondeur contrôlée dans l'élastomère des marqueurs colorés (rhodamine) pouvant servir de traceur (2).

A terme, l'objectif de ce projet est de proposer une description quantitative la plus complète possible du phénomène de transduction de l'information tactile digitale, prenant en compte les propriétés du capteur (caractéristiques mécaniques, géométriques, topographie de la surface) et les conditions d'exploration. Nous souhaitons en particulier tester plus avant le modèle de transduction de l'information de rugosité que nous avons récemment proposé, ce qui ne pouvait être fait avec un capteur unique. Nous adopterons pour cela la méthodologie déjà implémentée dans la configuration mono-capteur (rugosité aléatoire et corrélation inverse). Nous souhaitons également étudier le codage d'autres informations : courbure, détection d'un défaut unique, identification de la transition vers le glissement - essentiel pour les tâches de préhension (3) -, mesure des propriétés macroscopiques (coefficient de frottement, dureté, etc.)

Dans une optique plus applicative, nous souhaitons tester les possibilités de discrimination et de classification de textures « naturelles » offertes par le capteur biomimétique. Nous souhaitons en particulier évaluer dans quelle limite la texturation fine de la surface de la « peau » peut permettre de faciliter ce type de tâche. Cet aspect du projet se poursuit dans le cadre de la collaboration engagée depuis plusieurs années avec le LETI, qui vient de dupliquer le senseur bio-mimétique au sein de son département système, et devrait donner lieu cette année au recrutement d'un post-doc en co-tutelle. Pour cette étude, nous souhaitons utiliser des substrats modèles fournis par plusieurs laboratoires industriels avec lesquels des contacts sont déjà établis. Ceux-ci s'intéressent aux propriétés tactiles de familles de matériaux (émulsions, papier, tissus, etc.) qu'ils souhaiteraient pouvoir caractériser sans recours à des évaluations psychophysiques impliquant des panels d'experts.

Nous sommes conscients que la pertinence de l'approche biomimétique suivie, du point de vue strictement biologique, dépendra de la possibilité de confronter les résultats obtenus à des données neurophysiologiques, c'est-à-dire à des mesures de l'activité nerveuse du système mécano-sensoriel en réponse à des stimuli similaires. Chez l'homme (ou le primate), de telles données sont difficiles à obtenir[1]. Du fait de cette limitation propre au modèle humain, nous nous sommes engagés depuis cette année, dans une collaboration avec l'équipe dirigée par Daniel Shulz à l'Unité de Neurosciences Intégratives et Computationnelles (UNIC, CNRS, Gif sur Yvette). Ce dernier s'intéresse à la perception tactile vibrissale chez le rat, et développe notamment des mesures physiologiques dans le cortex somato-sensoriel.

Chez le rat, l'information tactile est contenue principalement dans la séquence de déformation de ses longues vibrisses faciales (ses moustaches) lorsque ces dernières parcourent la surface d'un substrat (4). Ces déformations mécaniques sont traduites en signaux nerveux par des mécanorécepteurs situés à la base du follicule pileux (5). Cette collaboration vise à caractériser la transduction mécanique de l'information tactile chez le rat par une approche relativement similaire à celle que nous avons développée pour le système tactile humain (Figure 12). L'utilisation d'une même méthodologie pour ces deux systèmes – digital et vibrissal – pourrait permettre d'identifier des stratégies communes d'amplification et de codage. Expérimentalement, il s'agira de mesurer optiquement, chez le rat anesthésié, les déformations de vibrisses dont l'extrémité est frottée contre des substrats de texture contrôlée. Ces expériences seront réalisées à Gif sur Yvette, mais la préparation des substrats, une partie de l'analyse et la modélisation biomécanique seront réalisées au laboratoire. Nous chercherons à établir le lien entre les propriétés topographique de la surface explorée et la séquence de déformation de la vibrisse, en particulier au niveau du follicule pileux. Cette étape de transduction mécanique de l'information tactile est essentielle pour comprendre le codage opérée par le système somato-sensoriel. Celui-ci pourra être testé ensuite par l'équipe de Gif en mesurant l'activité neuronales dans les aires corticales recevant l'information des vibrisses lorsque la séquence

[1] Nous avons néanmoins pris de premiers contacts en ce sens avec l'équipe de Jean-Pierre Roll, du laboratoire de Neurobiologie Humaine à Marseille, qui travaille sur le système somato-sensoriel humain.

de déflection, induites par une texture, sera « rejouée » au niveau de la base des vibrisses à l'aide d'actuateurs piezoélectriques (6).

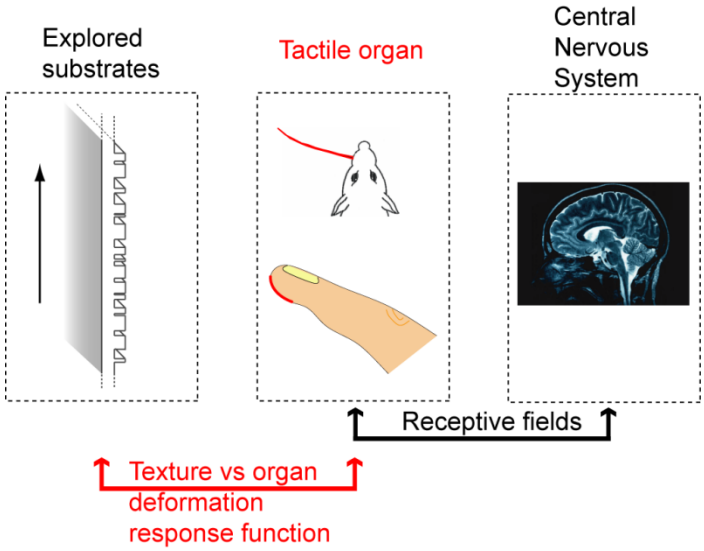

Figure 12 : Caractérisation de la transduction tactile chez l'humain et le rat. La détermination des champs récepteurs des neurones mécanorécepteurs consiste à identifier la réponse du neurone à la stimulation de l'organe tactile (vibrisse ou peau). Cette réponse dépend des propriétés intrinsèques du système somato-sensoriel. Le projet décrit vise au contraire à caractériser le lien entre les propriétés physiques du susbtrat exploré (ici une surface rugueuse) et la déformation de l'organe tactile. Cette réponse dépend des propriétés biomécaniques de l'organe mais aussi de facteurs contextuels tels que les conditions exploratoires.

C) FROTTEMENT SOLIDE ENTRE SURFACES MICRO-STRUCTUREES

Le comportement tribologique de deux objets en frottement dépend, dans une large mesure, des caractéristiques topographiques de leur surface. Les modèles traditionnels décrivant le champ des contraintes à une interface frottante se limitent souvent à une description statistique des hauteurs d'aspérités sans prendre en compte ni le couplage mécanique entre aspérités voisines (qui dépend de leur répartition spatiale), ni le couplage entre différentes échelles de rugosité (7; 8). D'un point de vue expérimental, l'utilisation de surfaces rugueuses « naturelles », obtenues par exemple par polissage mécanique, ne permet pas de moduler de manière contrôlée les propriétés topographiques superficielles, et ne peut donc permettre d'évaluer quantitativement ces effets. Nous souhaitons étendre l'étude des interfaces de frottement multi-contacts (thème 4 de ce document) à des surfaces micro-structurées par photolithographie, technique qui offre la possibilité d'un contrôle précis des propriétés topographiques de la surface ; cette même technique permet aussi, par greffage spécifique de molécules hydrophobes, de moduler spatialement les propriétés d'adhésion et de frottement.

L'approche expérimentale sera fondée, comme précédemment, sur une observation directe de l'interface frottante pour des contacts étendus. Nous chercherons à caractériser le comportement individuel et collectif des micro-contacts (corrélation spatiale et temporelle des événements de glissements notamment) en fonction de leurs caractéristiques géométriques et de leur distribution statistique. Nous évaluerons les conséquences de cette dynamique locale vis-à-vis de la réponse mécanique globale de l'interface. Des expériences préliminaires utilisant des surfaces constituées de plots cylindriques de quelques dizaines de micron de diamètre et répartis aléatoirement, ont montré une grande richesse de comportement (Figure 13). La dynamique de l'interface peut faire apparaître des événements de glissement cohérent de l'ensemble des plots, mais il existe également des régimes pour lesquels cette dynamique est stochastique, les événements de glissement impliquant des régions limitées de l'interface. Ce mécanisme microscopiquement incohérent se traduit par un signal de force global présentant un large spectre de fluctuations.

Au travers de ces expériences, nous souhaitons tester la possibilité d'une description nouvelle des interfaces frottantes inspirées de celle utilisée dans les systèmes désordonnés hors d'équilibre, en modélisant celles-ci comme un ensemble statistique d'oscillateurs multi-stables couplés mécaniquement via le matériau massif (9). Au-delà de la compréhension des processus mécaniques à l'œuvre dans le frottement aux interfaces rugueuses, cette étude peut permettre de guider la fabrication de surfaces présentant des propriétés tribologiques contrôlées (10; 11) (cf partie C).

Ce projet bénéficiera d'une collaboration mise en place récemment avec Antoine Chateauminois et Christian Fretigny (PPMD, ESPCI) qui travaillent sur des questions relativement proches. Cette équipe développe notamment des algorithmes d'inversion permettant d'extraire les contraintes dans des couches élastiques minces à partir des champs de déplacements mesurés en surface (2).

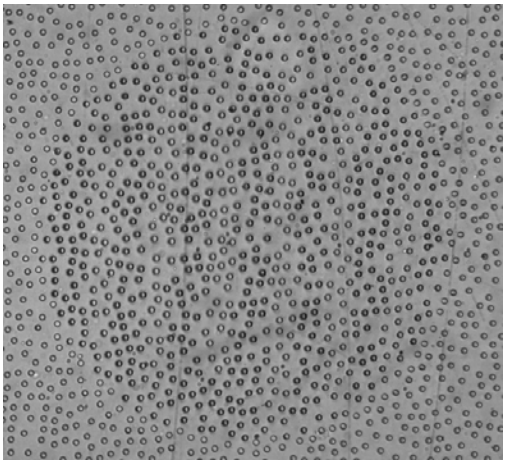

Figure 13 : Image en lumière transmise d'un contact frottant entre un bloc élastomère présentant des plots de 50µm de diamètre aléatoirement répartis en surface et une lentille sphérique. Sous l'effet du cisaillement, les plots fléchissent légèrement ce qui se traduit par l'apparition d'une bordure noire plus épaisse. L'apparence variée des plots au sein de la zone de contacts traduit l'hétérogénéité de cette flexion.

C) SURFACES ACTIVES ET INTERFACES HAPTIQUES

L'une des perspective des senseurs tactiles bio-mimétiques est leur intégration dans des systèmes robotiques déportés. Il s'agit de robots esclaves, contrôlés à distance et transmettant en temps réel des informations sensorielles donnant l'illusion à l'utilisateur d'intervenir directement sur l'environnement. De tels systèmes peuvent être utiles pour l'intervention dans des milieux hostiles (nucléaire, sous-marin, spatial, etc.), à des échelles inaccessibles (micro-chirurgie) ou dans des environnements virtuels (réalité virtuelle). Ces systèmes nécessitent l'intégration d'interfaces haptiques capables de produire une sensation tactile contrôlée et réaliste (12). Dans ce domaine, le rendu des textures des objets manipulés reste la composante la moins développée. Les dispositifs existants consistent en des matrices d'actuateurs (typiquement de l'ordre de quelques dizaines) pouvant être adressés individuellement. Les actuateurs font appel à diverses technologies (MEMS, électro-magnétique, piezo, etc). Aucun d'entre eux ne permet à ce jour d'atteindre simultanément les vitesses d'actuation, les amplitudes de déformation et la densité spatiale nécessaires au rendu de tout type de texture. En outre, l'encombrement et le poids de nombre de ces dispositifs handicapent leur implémentation dans des systèmes robotiques.

Dans cette optique, nous envisageons de développer des interfaces micro-structurées actives en adaptant certaines techniques issues de la micro-fluidique (13). Il s'agit de membrane PDMS réticulées au sein de laquelle sont intégrés des micro-réservoirs (de diamètre de l'ordre de quelque dizaines à quelques centaines de microns) connectés par un réseau de canaux micro-fluidiques. Ces

réservoirs peuvent être activés pneumatiquement au moyen de mini-valves électro-magnétiques, produisant ainsi une protrusion à la surface du PDMS. Un tel dispositif aurait plusieurs avantages : d'une part, les vitesses d'actuation, pour de telles dimensions, sont supérieures à la centaine de Hertz et les déformations produites sont importantes. Par ailleurs, la membrane est compliante et peut donc s'adapter sur le doigt ou la main. Cette souplesse de la membrane laisse envisager la possibilité de superposer plusieurs de ces dispositifs, afin d'obtenir une actuation simultanée à plusieurs échelles spatiales, ce qu'aucun dispositif actuel n'est en mesure de produire.

Outre l'aspect haptique, nous souhaitons évaluer comment cette interface active pourrait permettre un contrôle dynamique des propriétés de frottement (et notamment du coefficient de frottement) par une modulation contrôlée des propriétés mécaniques de l'interface et de la zone réelle de contact.

Bibliographie :

1. R.S. Johansson, I. Birznieks. *Nat Neurosci.* 2004, Vol. 7, 2, pp. 170-7.
2. A. Chateauminois, C. Fretigny. *Eur. Phys. J. E.* 2008, Vol. 27, pp. 221-227.
3. R.S. Johansson, J.R. Flanagan. *Nature Reviews Neuroscience.* 2009, Vol. 10, p. 345:359.
4. T. Prigg, D. Goldreich, G.E. Carvell and D.J. Simons. *Physiol. Behav.* 2002, Vol. 77, pp. 671-675.
5. B.L.J. Munger, F.L. Rice. *Comp Neurol.* 1986, Vol. 252, pp. 186-205.
6. V. Jacob, J. Le Cam, V. Ego-Stengel and D.E. Shulz. *Neuron.* 2008, Vol. 60, p. 1112:1125.
7. J.A. Tripp, J.H. Greenwood. *Trans. ASME Series E, Journal of Applied Mechanics .* 1967, Vol. 34, 153.
8. B.N.J.Persson. *J. Chem. Phys.* 2001, Vol. 115, 3840.
9. P.Nozières, C. Caroli. *Eur. Phys. J. B.* 1998, Vol. 4, 233.
10. M. Lamblet, E. Verneuil, P. Silberzan, T. Vilmin, L. Léger. *Langmuir.* 2007, Vol. 23, p. 6966.
11. C. Majidi, R. E. Groff, Y. Maeno, B. Schubert, S. Baek, B. Bush, R. Maboudian, N. Gravish, M. Wilkinson, K. Autumn and R. S. Fearing. *PRL.* 2006, Vol. 97, 076103.
12. G. Moy, U. Singh, E. Tan and R. S. Fearing. *Haptics-e, The Electronics J. of Haptics Research.* 2000, Vol. 1, 3, p. 20.
13. M.A. Unger, H.-P. Chou, T. Thorsen, A. Scherer and S. Quake. *Science.* 2000, Vol. 288, 7, pp. 113-116.

PUBLICATIONS, CONFERENCES ET SEMINAIRES

A) LISTE DES PUBLICATIONS

Articles publiés dans des revues à comité de lecture

1. Stress Field at a Sliding Frictional Contact: Experiments and Calculations, J. Scheibert, E. Katzav, M. Adda-Bedia, A. Prevost et G. Debrégeas, *J. Mech. Phys. Solids*, **57**, 1921-1933 (2009)
2. Effect of fingerprints orientation on skin vibrations during tactile exploration of textured surfaces, A. Prevost, J. Scheibert and G. Debrégeas, *Communicative and Integrative Biology* **2**(5) (2009)
3. The role of fingerprints in the coding of tactile information probed with a biomimetic sensor, J. Scheibert, S. Leurent, A. Prevost et G. Debrégeas, *Science* **323** 1503-1506 (2009)
4. Dissipation in a Sheared Foam: From Bubble Adhesion to Foam Rheology, S. Besson, G. Debrégeas, S. Cohen-Addad and R. Höhler, *Phys. Rev. Lett.* **101**, 214504 (2008)
5. Experimental Evidence of Non-Amontons Behaviour at a Multi-contact Interface, J. Scheibert, A. Prevost, J. Frelat, P. Rey and G. Debrégeas, *Europhys. Lett.* **83**, 34003 (2008)
6. Statics and dynamics of adhesion between two soap bubbles, S. Besson and G. Debrégeas, *Eur. Phys. J. E* **24**, 109-117 (2007)
7. Quasi-static rheology of foams. Part 1. Oscillating strain, A. Kabla and G. Debrégeas, *Journal of Fluid Mechanics*, **587**, pp 23-44 (2007)
8. Quasi-static rheology of foams. Part 2. Continuous shear flow, A. Kabla, J. Scheibert and G. Debrégeas, *Journal of Fluid Mechanics* **587**, pp 45-72 (2007)
9. X-ray observation of micro-failures in granular piles approaching an avalanche, A. Kabla, G. Debrégeas, J.-M. di Meglio and T. J. Senden, *Europhys. Lett.* **71** 932-937 (2005)
10. Contact Dynamics in a Gently Vibrated Granular Pile. A. Kabla and G. Debrégeas, *Phys. Rev. Lett.* **92**(3), 035501(2004)
11. Local Stress Relaxation and Shear Banding in a Dry Foam under Shear. A. Kabla and G. Debrégeas, *Phys. Rev. Lett.* **90**(25) 258303 (2003)
12. Partial rejuvenation of a colloidal glass. F. Ozon, T. Narita, A. Knaebel, G. Debrégeas, P. Hébraud and J.-P. Munch, *Phys. Rev. E* **68**, 032401 (2003)
13. Rheology of soft glassy materials. D. Bonn, P. Coussot, H. Huynh, F. Bertrand and G. Debrégeas, *Europhys. Lett.*, **59** (5), pp. 786-792 (2002)
14. Stick-slip instability for viscous fingering in a gel. N. Puff, G. Debrégeas, J.-M. di Meglio, D. Higgins, D. Bonn, C. Wagner, *Europhys. Lett.* **58**(4), p. 524 (2002)
15. Deformation and Flow of a Two-Dimensional Foam under Continuous Shear. G. Debrégeas, H. Tabuteau, and J.-M di Meglio, *Phys. Rev. Lett.* **87**(17) 178305 (2001)
16. A self-similar model for shear flows in dense granular materials. G. Debrégeas and C. Josserand, *Europhys. Lett.*, **52** (2), pp. 137-143 (2000)
17. Signatures of granular microstructure in dense shear flows. D. Mueth, G. Debregeas, G. Karczmar, P. Eng, S. Nagel & H. Jaeger, *Nature* **406**, 385-388 (2000)
18. The Life and Death of "Bare" Viscous Bubbles. G. Debrégeas, P.-G. de Gennes, F. Brochard-Wyart, *Science* **279**, 1704 (1998)
19. Dewetting of Supported Viscoelastic Polymer Films: Birth of Rims. F. Brochard-Wyart, G. Debrégeas, R. Fondecave, and P. Martin, *Macromolecules*, **30**(4) pp 1211-1213 (1997)
20. Nucleation radius and growth of a liquid meniscus. G. Debrégeas, F. Brochard-Wyart, *Journal of colloid and interface science* **190**(1) pp.134-141(1997)

21. Spreading of viscous droplets on a non viscous liquid F. Brochard-Wyart, G. Debrégeas, P.-G. de Gennes, *Colloid and polymer science* **274**(1) pp.70-72 (1996)
22. Experimental Study of the Spreading of a Viscous Droplet on a Nonviscous Liquid. L. Bacri, G. Debrégeas, and F. Brochard-Wyart, *Langmuir* **12**(26), pp 6708-6711 (1996)
23. Viscous Bursting of Suspended Films. G. Debrégeas, P. Martin and F. Brochard-Wyart, *Phys. Rev. Lett.* **75**(21) 3886 (1995)

Articles soumis ou en préparation :

24. Micro-slip field at a rough contact driven towards macroscopic sliding, Julien Scheibert, Georges Debrégeas, Alexis Prevost *(soumis)*
25. Optical measurement of the pressure at a multicontact interface, Julien Scheibert, Alexis Prevost, and Georges Debrégeas *(en préparation)*

Articles de synthèse :

26. L'éclatement de bulles visqueuses, G. Debrégeas et F. Brochard-Wyart, *Pour la Science*, mai 1995
27. Mécanique du contact rugueux et perception tactile, Julien Scheibert, Georges Debrégeas et Alexis Prevost, *Reflets de la physique* n°**16**, octobre 2009, pp. 17-19
28. Toucher digital humain : transduction mécanique de l'information tactile et rôle des empreintes digitales, Georges Debrégeas, Alexis Prevost, Julien Scheibert, A paraître dans le prochain numéro des *Images de la Physique*

Acte de Congrès :

29. A Novel Biomimetic Haptic Sensor to study the Physics of Touch, J. Scheibert, A. Prevost, G. Debrégeas, R. Rousier et P. Rey, *Actes Mécano−Transduction* (2004).

B) CONFERENCES ET SEMINAIRES

Participation à des conférences en tant qu'intervenant invité

1. *06/10* : Gordon Research Conference on Tribology, Waterville, Maine.
2. *09/09* : Workshop : "Flowing Complex Fluids: Rheological measurements and constitutive modeling", Institute for Mathematics and its Applications, University of Minnesota, USA.
3. *01/09* : Physics@FOM, Veldhoven, Hollande.
4. *05/08* : "DeGennesDays", IHP, Paris.
5. *10/07* : Franco-Israeli Trends, Biarritz, France.
6. *09/06* : Second European SCAT (Scientific Computing Advanced Training) Workshop, Jussieu, Paris.
7. *02/05* : Cours "milieux granulaires", conférence IHP, Paris.
8. *03/04* : American Physical Society March Meeting, Montreal, Canada.
9. *11/03* : Gordon Research International Meeting on Rheology, Lausanne, Suisse.
10. *04/03* : Euroconference on Complex Fluid Interfaces, San Feliu de Guixol, Espagne.
11. *02/03* : Ecole des Houches, « From Elasticity to Plastic Flow in Condensed Media » (cours 3h)
12. *07/02* : Gordon Research Conference on « Complex Fluids », Cambridge, UK.
13. *04/02* : Journée "mousses", Orsay.
14. *07/01* : 4th International Discussion Meeting on Relaxations in Complex Systems, Heraklion, Grèce.
15. *06/01* : Colloque des Houches, "New concepts in foams".
16. *11/00* : Nestlé International Meeting on Rhéology, Lausanne, Suisse.
17. *07/97* : Gordon Research Conference on Elastomers, Networks and Gels. New London, USA.

Autres conférences et seminaires

18. *12/09* : Tactile sensing workshop @ Humanoids '09, Jussieu, Paris
19. *11/09* : Séminaire IUSTI, Marseille.
20. *11/09* : Mechanics Colloquium in the Department of Engineering at Cambridge University, Cambridge, UK.
21. *04/09* : Séminaire général du département de Physique de l'ENS, Paris.
22. *04/09* : Séminaire neurosciences théoriques du département d'études cognitives de l'ENS, Paris
23. *02/09* : Séminaire da la Formation Interuniversitaire de Physique, ENS, Paris.
24. *06/08* : Journées du LPS, ENS, Paris.
25. *10/08* : Séminaire/cours à l'ENSAD, Paris (1h30).
26. *04/06* : Séminaire CRPP, Bordeaux.
27. *2003-2006* : Participation régulière au GDR « Mousses ».
28. *05/05* : Séminaire LPPMD, ESPCI, Paris.
29. *04/05* : Séminaire FAST, Orsay.
30. *11/04* : Séminaire GDPC, Montpellier.
31. *11/04* : Journées de l'ENS, IHP, Paris.
32. *2001-2003* : Participation régulière au GDR « Milieux divisés ».
33. *02/03* : Séminaire Centre de Recherche Rhodia, Aubervilliers.
34. *03/03* : Séminaire Centre de Recherche Nestlé, Lausanne.
35. *07/03* : Séminaire PMMH, ESPCI, Paris.
36. *03/02* : Séminaire Dept. Applied Mathematics, Australian National University, Canberra, Australie.
37. *06/02* : Séminaire LDFC, Strasbourg.
38. *11/02* : Séminaire CRPP, Bordeaux.
39. *11/02* : Séminaire LPT/LPTMS, Orsay.
40. *03/02* : Séminaire LPS, ENS, Paris.
41. *04/02* : Séminaire James Frank Institute, University of Chicago, USA.
42. *12/02* : Séminaire LETI, CEA Grenoble.
43. *12/01* : Séminaire Laboratoire de spectrometrie physique, Grenoble.
44. *11/01* : Séminaire ENS, Lyon.
45. *11/01* : Séminaire GMCM, Rennes.
46. *09/01* : Ecole d'été "milieux divisés", Porquerolles.
47. *06/01* : Séminaire MMB (commun au LMDH - LMCP - LI2C – LBHP), Jussieu, Paris.
48. *05/01* : Séminaire LMDH Jussieu, Paris.
49. *05/01* : Séminaire LPCM, ESPCI, Paris.
50. *03/01* : Séminaire IRPHE, Marseille.
51. *12/00* : Séminaire Département de Chimie, Université de Florence, Italie.
52. *08/00* : 7èmes Journées de la Matière Condensée (SFP). Poitiers, (Poster).
53. *06/00* : Eurofoam : 3rd Conference on Foams, Emulsions and Applications. Delft, Pay-bas, (Poster).
54. *10/00* : Séminaire LMM Jussieu, Paris
55. *12/98* : Séminaire Department of Applied Mathematics, MIT, Cambridge, USA.
56. *08/98* : 17th General Conference of the Condensed Matter Division (EPS) & 6èmes Journées de la Matière Condensée (SFP), Grenoble.
57. *03/98* : APS March Meeting, Los Angeles.
58. *05/97* : Séminaire James Frank Institute, Université de Chicago, USA.
59. *12/96* : Conference on Instabilities and Dewetting of Thin Films. Mulhouse.
60. *06/96* : SIS Symposium (Surfactants in Solutions), Jérusalem, Israël (poster).
61. *05/96* : Conférence Internationale sur les Mousses, Arcachon.
62. *06/95* : Rencontre de Carry-le-Rouêt.

ENCADREMENT ET ENSEIGNEMENT.

A) ENCADREMENT D'ETUDIANTS ET JEUNES CHERCHEURS

Thèses :

1. Alexandre Kabla (soutenance en 2003)
   Désordre et plasticité dans les milieux divisés : mousses et matériaux granulaires
   Actuellement professeur assistant au département de Mechanical Engineering de l'Université de Cambridge, UK.
2. Julien Scheibert (soutenance en 2007)
   Mécanique du contact aux échelles mésoscopiques (récompensé par le prix Edouard Branly).
   Actuellement en post doc à l'Université d'Oslo, Norvège.
3. Sébastien Besson (soutenance en 2007)
   Propriétés adhésives entre deux bulles de savon
   Actuellement en post-doc à l'Université d'Harvard, USA.

ATER/post-doc :

4. Nicolas Puff (de Septembre 2000 à Juin 2001)
5. Florian Ozon (de Septembre 2001 à Juin 2002)
6. Eric Janiaud (de Novembre 2003 à Juin 2004)
7. Raphaël Candelier (depuis Octobre 2009)

DEA/Master 2 :

8. Alexandre Kabla (de Février à Septembre 2000)
9. Hervé Tabuteau (Février à Juillet 2000)
10. Julien Scheibert (de Février à Juillet 2002)
11. Sébastien Besson (de Octobre à Juin 2003)
12. Sébastien Leurent (de Janvier à février 2008)
13. Flavien Kiefer (de Janvier à Février 2008)
14. Frederico Zalamea (de Janvier à Février 2010)

License/Maitrise (M1)/Ecole d'ingénieur :

15. Douglas Higgins (de Juillet à Août 1999)
16. Gregory Francius (de Avril à Juin 2002)
17. Sébastien Kremer (de Avril à Juin 2004)
18. Maxime Deforet (de Avril à Juin 2007)
19. Julien Dupas (de Avril à Juillet 2008)
20. Adrien Bouty (de Avril à Juillet 2009)

B) ENSEIGNEMENT

1995-1997 : Cours « formulation » à l'IUT de Cergy (18 heures/an).
2000-2001 : Préparation à l'agrégation, Université Louis Pasteur à Strasbourg (6 heures).

2001-2002 : « Physique des milieux granulaires », cours d'option au DEA « Matière Condensée » de l'université Louis Pasteur à Strasbourg (16 heures).

2004-2006 : « Physique des milieux granulaires », cours d'option dans le cadre du parcours recherche « Physique des Fluides Complexes et des Milieux Structurés », Master 2 de Physique à Paris 7, (21 heures/an).

2008-2010 : « Physique de la perception tactile », cours d'option au M1 de physique pour les biologistes de l'ENS Paris (6 heures/an).

AUTRES INFORMATIONS

A) RESPONSABILITES ADMINISTRATIVES :

J'ai co-organisé en Mai 2002 une école à Carry-le-Rouet sur la rhéologie des mousses.

J'ai organisé les séminaires à l'ICS (2 ans), au Collège de France (1 an) et au LPS (2 ans), et ai été membre du conseil de laboratoire dans ces trois laboratoires.

J'ai été membre de deux comités de sélection pour des recrutements d'enseignant chercheur à l'ESPCI et Paris 7.

B) INFORMATION SCIENTIFIQUE

Animation d'un stand « physique du tas de sable » à la Science en fête (éditions 2001 et 2002).

L'article [3] a donné lieu à plusieurs compte-rendu dans la presse scientifique et généraliste, dont notamment :

Revues scientifiques : Science news, Science Update (radio), Science signaling, Nature news, Nature Research highlights, Nature Methods, Analytical Chemistry, Atten. Percept & Psych.,

Journaux institutionnels : Journal du CNRS, Harvard Science review, Cern Courier, MIT technology.

Medias Nationaux : Libération, Le Monde, Le Figaro, Le Nouvel Obs, La Recherche, Science et Vie.

Medias internationaux : NRC Handelsblad (Hollande), Science News Magazine (USA), Scientific American, ABC (Canada), La Presse (Montréal), German Public Radio, CNN online, Forskning & Framsteg (Suède), Frankfurter Allgemeine (Allemagne).

C) SEJOURS A L'ETRANGER

1997-1998 : James Frank Institute, Université de Chicago, USA (18 mois) – Grainger post-doctoral fellowship.

2000 : Département de Chimie (équipe de Piero Baglioni), Université de Florence, Italie (6 semaines) – contrat Galileo « smart foams ».

2002 : Department of Applied Mathematics, Australian National University, Canberra, Australie (6 semaines) – équipe de Tim Senden.